ALMA MATER STUDIORUM
UNIVERSITÀ DI BOLOGNA

DOTTORATO DI RICERCA IN FISICA

Ciclo XXXVII

Settore Concorsuale: 02/A1 - Fisica Sperimentale delle Interazioni Fondamentali
Settore Scientifico disciplinare: FIS/01 - Fisica Sperimentale

Study of Neutrino Interactions on Hydrogen in the SAND Detector of DUNE

Presentata da:

Gianfranco Ingratta

Coordinatore Dottorato:

Prof Alessandro Gabrielli

Supervisore:

Laura Patrizii

Co-Supervisori:

Matteo Tenti

Nicoletta Mauri

Esame finale anno 2025

All the science I don't understand, it's just my work 5 days a week.

Abstract

The Deep Underground Neutrino Experiment (DUNE) is a next-generation long-baseline neutrino oscillation project. Its primary goals are to measure the possible δ_{CP} violation phase and determine the sign of Δm^2_{13}, which is crucial for understanding the neutrino mass hierarchy. DUNE will exploit a Far Detector consisting of four multi-kiloton Liquid Argon Time Projection Chambers (LArTPCs) and a Near Detector (ND) complex situated near the neutrino source at Fermilab.

One of the main limitations on the achievable precision on the measure of the neutrino flux, are the large uncertainties on neutrino cross-section on nuclei, which stems from the choice of a nuclear model and of final state interactions, that cannot be calculated in perturbative QCD.

The measurement of neutrino interactions on **free nucleon** would instead allows to minimize the uncertainties on the flux, because the neutrino cross-section on free nucleon is known with much lower uncertainty.

The SAND detector uses a low-density tracker in a magnetic field combined with a high-granularity calorimeter with high neutron detection efficiency and exceptional timing resolution to distinguish interactions on Hydrogen from those on nuclei.

This thesis explores a detailed approach to achieve precise (anti)neutrino on Hydrogen measurements by statistically subtracting interactions on thin graphite targets (pure C) from those on polypropylene (C3H6) targets (*solid Hydrogen* [1]). With the neutrino-Hydrogen cross-section known to percent-level precision, this study demonstrates that SAND can measure the flux with uncertainties at the few-percent level, with margins for future improvements.

Contents

Chapter 1

Neutrino Oscillations

Neutrinos are the most abundant of all Standard Model fermions in the Universe, and yet the most elusive. We did not even realize they existed till the '30. The idea came about in the study of β decays ${}^{A}_{Z}X \rightarrow {}^{A}_{Z-1}Xe^{+}$ with an observed continuum spectrum for the observed positron, where energy conservation would unavoidably imply a monochromatic spectrum. On 4 December 1930 Pauli proposed a "desperate way out" to save energy conservation postulating the existence of a new neutral particle originally called "neutron" and lately, in 1934, Fermi proposed its theory of beta decay [2] containing "speculations too remote from reality".

Neutrinos were finally directly observed by Cowan and Reines in 1956 in a nuclear reactor experiment, and found to be left-handed in 1958. Davis et al., following Pontecorvo's technique, first detected a neutrino anomaly in 1968 by measuring a solar ν_e rate lower than predicted by Bahcall et al. Despite extensive efforts, until recent years, the distinction between a solar neutrino problem and a neutrino solar problem remained unclear. In 2002, two signals emerged: SNO detected evidence of ν μ τ appearance, while KamLAND confirmed the solar anomaly by observing the disappearance of $\overline{\nu}$ from Japanese reactors. Additionally, in 1998, (Super)Kamiokande identified a second neutrino anomaly [3] by analyzing atmospheric neutrinos, validated by K2K around 2004 [4], marking the inaugural long base-line neutrino beam experiment.

1.1 Massless neutrinos in the SM

In all observed processes, baryon number B and lepton number L are conserved. A Key aspect of gauge theories, such as the Standard Model, is that B and L automatically emerge as approximately conserved charges, where pre-SM theories introduced a new conserved charge, called baryon number B, under which the proton is the lightest charged particle. The most general $SU(3)_c \times SU(2)_L \times U(1)_Y$ gauge-invariant renormalizable Lagrangian that can be written with the SM field (the Higgs doublet H and the observed fermions: the doublets $L = (\nu, l_L)$, $Q = (u_L, d_L)$ and the singlets l_R , u_R , d_R) beyond 'minimal' terms (kinetic and gauge interactions) can only contain the following Yukawa and Higgs-potential terms:

$$L_{SM} = L_{minimal} + (\lambda_l^{ij} l_R^i L^j H^* + \lambda_d^{ij} d_R^i Q^j H^* + \lambda_u^{ij} u_R^i Q^j H + h.c.) + m^2|H|^2 - \lambda/4|H|^4 \tag{1.1}$$

with i, j flavour indices. No term violates baryon number B and lepton flavour L_e, L_μ, L_τ that therefore emerge as accidental symmetries.

Within the Standard Model (SM), there's no requirement to manually enforce a stable proton or massless neutrinos. This approach yields more accurate predictions, as baryon flavor and CP violation occur in a precise manner outlined by the CKM matrix. This phenomenon results, among other things, in distinctive rates of transitions such as $K^0 \leftrightarrow \overline{K}^0$ and $B^0 \leftrightarrow \overline{B}^0$.

The Higgs vev breaks $SU(2)_L \times U(1)_Y \rightarrow U(1)_{em}$:

$$\langle H \rangle = (0, v) \qquad with \qquad v \approx 174 GeV \tag{1.2}$$

and gives Dirac masses to charged leptons and quarks mass terms $m_i = \lambda_i v$:

$$m_R l_R l_L + m_d d_R d_L + m_U u_R u_D \tag{1.3}$$

but neutrinos remain massless. A Dirac mass term both neutrino and antineutrinos would appear, but so far there is no experimental evidence of the existence of a right-handed neutrino. Within the SM, neutrinos are fully described by the kinetic term plus gauge interactions with the massive vector bosons $\overline{\nu} Z \nu$ and $\overline{\nu} W l_L$.

1.2 Massive neutrinos beyond the SM

The phenomenon of neutrino oscillations has given proof of non-zero neutrino mass, whose absolute value is still unknown. Different methods are used to estimate the absolute neutrino mass: cosmological studies, search for neutrinoless double β-decay and direct measurements based on the kinematics of single β-decay. For the latest, the most stringent results on the effective ν_e mass were obtained by the KATRIN experiment [5], which set an upper limit of 0.8 eV (90% CL).

Results obtained using cosmological data, such as the ones from the WMAP and Planck experiments, provide an upper limit on the sum of the three neutrino masses. Such results are model dependent and, in the ΛCDM Standard Cosmological Model, typical values are: $\Sigma_i m_i < (0.11 - 0.54) eV$ [6].

The Standard Model fails to explain the masses of neutrinos. Additionally, unlike other fermions, neutrinos lack electric or color charge. This suggests the potential for neutrinos to be self-conjugate particles. A fermion possessing this property is termed a Majorana fermion, whereas in the alternative scenario, it is referred to as a Dirac fermion.

The minimal SM extension that includes the neutrino masses would introduce a right-handed neutrino ν_R. However, these new particles are fundamentally different from those of the SM, as they do not participate in the weak interaction, but just the gravitational one. For this reason, they are called *sterile*.
A different approach is to make use of the charge-conjugation matrix C to rewrite the Dirac equation in terms of left-handed fields only, in which the fields can be written as:

$$\nu = \nu_L + \nu_R = \nu_L + \nu_L^C \tag{1.4}$$

From Eq.1.3 it follows that a Majorana particle is its own anti-particle:

$$\nu^C = (\nu_L + \nu_L^C) = \nu_L^C + \nu_C = \nu \tag{1.5}$$

For a Majorana particle, the mass term is written using only the left-handed component of the field:

$$-\frac{1}{2}m\overline{\nu}_L^C\nu_L \tag{1.6}$$

Up to date, there is no experimental evidence whether neutrinos are Dirac or Majorana particles that remains one of the open questions 1.4 in the neutrino physics. Eq. 1.6 is not invariant under $SU(2)\times U(1)$ transformation and, moreover, it violates the lepton number conservation by two units.

1.3 The oscillation phenomenon

The idea of neutrino-antineutrino oscillation was first discussed by Pontecorvo in 1957, following the analogy with koan-antikaon oscillations. A little later, the transformation of a neutrino of a certain flavor into a neutrino of a different flavor was hypothesized; it was then pointed out that this implies that neutrinos must have non-zero masses. Similar to the quark sector, there is a non-exact correspondence between the weak gauge eigenstates (that enters the weak interactions as beta decay) and the mass eigenstates (eigenvectors of the Hamiltonian). Indeed, in the quark sector the CC Lagrangian is written as:

$$\mathcal{L}_{CC}^{quarks} = \frac{g}{\sqrt{2}}\left[\begin{pmatrix}\bar{u}_L & \bar{c}_L & \bar{t}_L\end{pmatrix} V\gamma^\mu \begin{pmatrix}d_L\\ s_L\\ t_L\end{pmatrix} W_\mu^+ \quad + \quad h.c.\right] \tag{1.7}$$

where the subscript L refers to the left chiral component of the quark fields, γ^μ are the usual Dirac matrices and W_μ^+ is the charged vector boson field mediating the weak interactions. As far as V is concerned, this is the CKM matrix, which can be factorized as product of 2 unitary 3×3 matrices $V = V_u^\dagger V_d$. The latter allows moving from mass to weak (or flavor) eigenstates, the ones that join the weak interactions.

The mass differences between quarks are so large that there are no oscillations between quark: e.g. the down type quark q produced in decays of charmed hadrons, $c \to q l \overline{\nu}$, is $|q\rangle = \cos\theta_C\,|d\rangle + \sin\theta_C\,|s\rangle$, giving rise to a π with probability $\cos^2\theta_C$ and to K with probability $\sin^2\theta_C$, not to $\pi \leftrightarrow K$ oscillations. Moreover, unlike neutrinos, heavier quarks decay fast, making the oscillation phenomenon practically not observable.

In the SM, the charge current interactions in the lepton sector has a Lagrangian similar to Eq.1.7, except that weak and mass eigenstates coincide. But since neutrinos oscillates, this assumption is no longer correct, thus it is natural to introduce, again, 2 unitary 3×3 matrices V_l and V_ν such that:

$$\mathcal{L}_{CC}^{leptons} = \frac{g}{\sqrt{2}}\left[\begin{pmatrix}\bar{e}_L & \bar{\mu}_L & \bar{\tau}_L\end{pmatrix} U_{PMNS}\gamma^\mu \begin{pmatrix}\nu_{1L}\\ \nu_{2L}\\ \nu_{3L}\end{pmatrix} W_\mu^+ \quad + \quad h.c.\right] \tag{1.8}$$

where $U_{PMNS} = V_l^\dagger V_\nu$ is the so called Pontecorvo-Maki-Nakagawa-Sakata mixing matrix. It is customary to define left-handed flavor neutrino fields as:

$$\boldsymbol{\nu}_L = \begin{pmatrix}\nu_{eL}\\ \nu_{\mu L}\\ \nu_{\tau L}\end{pmatrix} = U_{PMNS}\begin{pmatrix}\nu_{1L}\\ \nu_{2L}\\ \nu_{3L}\end{pmatrix} = U_{PMNS}\mathbf{n}_L \tag{1.9}$$

with ν_{iL} $(i = 1, 2, 3)$ left-handed neutrino mass eigenstates.

In the case of three light neutrinos, the PMNS mixing matrix can be parametrized by three mixing angles θ_{12}, θ_{23} and θ_{13} and depending on whether the massive neutrinos are Majorana or Dirac particles, by one or three CP violating (CPV) phases. It is customary to express the mixing matrix as a product of 3 3×3 rotation matrices for a reason that will be soon clarified:

$$\begin{aligned} U_{PMNS} &= \begin{pmatrix} U_{e1} & U_{e2} & U_{e3} \\ U_{\mu 1} & U_{\mu 2} & U_{\mu 3} \\ U_{\tau 1} & U_{\tau 2} & U_{\tau 3} \end{pmatrix} \\ &= \begin{pmatrix} 1 & 0 & 0 \\ 0 & c_{23} & s_{23} \\ 0 & -s_{23} & c_{23} \end{pmatrix} \begin{pmatrix} c_{13} & 0 & s_{13}e^{-i\delta_{CP}} \\ 0 & 1 & 0 \\ -s_{13}e^{i\delta_{CP}} & 0 & c_{13} \end{pmatrix} \begin{pmatrix} c_{12} & s_{12} & 0 \\ -s_{12} & c_{12} & 0 \\ 0 & 0 & 1 \end{pmatrix} P \end{aligned} \tag{1.10}$$

Where $P = diag(1, e^{\lambda_2}, e^{\lambda_3})$ and in case neutrinos are Dirac particles $\lambda_2 = \lambda_3 = 1$. In the matrix $c_{ij} = \cos\theta_{ij}$ and $s_{ij} = \sin\theta_{ij}$.
$\delta_{CP} \in [0, 2\pi[$ is usually called Dirac phase, while λ_2, λ_3 are usually referred to as Majorana phases. Since oscillations which involve the θ_{12} angle and Δm^2_{12} where historically investigated in the solar experiments (observation of neutrinos from the Sun) and the ones involving θ_{23} and Δm^2_{23} in the atmospheric experiments (study of neutrinos from cosmic rays in the atmosphere), θ_{12} and θ_{23} are called "solar" and "atmospheric" mixing angle indicated with $\theta_{12} = \theta_{\odot}$ and $\theta_{23} = \theta_{atm}$ respectively. The same applies for $\Delta m^2_{12} = \Delta m^2_{\odot}$ and $\Delta m^2_{32} = \Delta m^2_{atm}$.

1.3.1 Vacuum oscillations of two neutrinos

The mass difference between the three active neutrinos is very different, as shown in 1.5. In most cases, it is practical to consider the dominant oscillation generated by two flavour neutrinos, so that the oscillation probability depends only on one mixing angle and there is no CP violation.

Let's assume a neutrino source that at the production region, $x = 0$, neutrino of a given flavour $|\nu_\alpha\rangle$ are generated with monochromatic energy E. The mixing matrix in Eq. 1.10 in case of two neutrinos it is just a rotation in 2-D space so that, given the neutrino mass eigenstates $|\nu\rangle_{1,2}$, the flavour state is $|\nu(x=0)\rangle = |\nu\rangle_\alpha = \cos\theta\,|\nu\rangle_1 + \sin\theta\,|\nu\rangle_2$. Since ν_1 and ν_2 have different masses, the initial ν_α evolves as a mixture of the mass states, so that after having travelled for a distance x:

$$|\nu(x)\rangle = e^{ip_1 x}\cos\theta\,|\nu\rangle_1 + e^{ip_2 x}\sin\theta\,|\nu\rangle_2 \tag{1.11}$$

The probability of detecting a different neutrino flavour ν_β at the detection point $x = L$ is:

$$P(\nu_\alpha \to \nu_\beta) = |\,\langle\nu_\beta|\nu(L)\rangle\,|^2 = \sin^2 2\theta \sin^2\frac{(p_2 - p_1)L}{2} \approx \sin^2 2\theta \sin^2\frac{\Delta m^2_{12} L}{4E} \tag{1.12}$$

where in the final passage it has been used the relativistic approximation $p_i = E - m_i^2/2E$ and $\Delta m^2_{12} = m_2^2 - m_1^2$. The oscillation length is defined as the value of the baseline L for which the transition probability is maximal, i.e. equal to $\sin^2 2\theta$:

$$L^{osc}[km] = 2.47\frac{E[GeV]}{\Delta m^2[eV^2]} \tag{1.13}$$

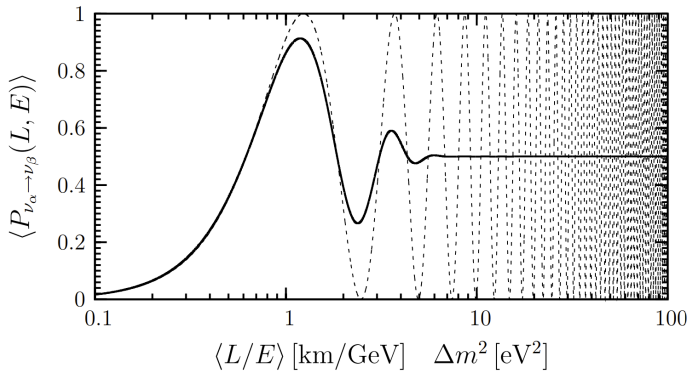

Figure 1.1: (a) Probability of $\nu_\alpha \to \nu_\beta$ for $\sin^2 2\theta = 1$ as a function of $\langle L/E \rangle$ and Δm^2. Solid line: transition probability in Eq. 1.12. Dashed line: averaged transition probability over a Gaussian distribution of L/E that simulates the effect of the experiment's finite spatial and energy resolutions.

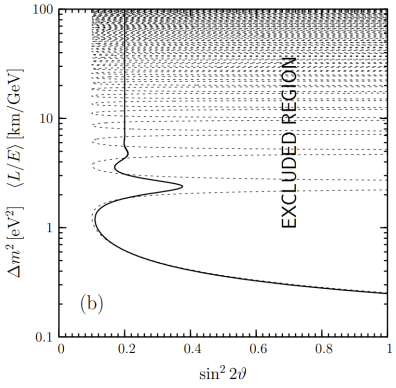

Figure 1.2: (b) Exclusion curve for $\sin^2 2\theta$ as a function of $\langle L/E \rangle$ and Δm^2.

In Fig. 1.1 the dashed line represents Eq. 1.12 as a function of argument of the sine function $\Delta m^2 L/E$. The location of the first dip of the transition probability occurs at $\Delta m^2 L/E = 2.47$ (see Eq. 1.13).

In real experiments the neutrino source is not monochromatic and the detector has finite spatial and energy resolutions, thus it is impossible to measure the oscillation probability for precise values of L/E. Therefore, it is always necessary to average the Eq. 1.12 over an appropriate distribution of L/E, for example a Gaussian distribution $\phi(L/E)$ with average $\langle L/E \rangle$ and standard deviation $\sigma_{L/E}$. A complete derivation of the convoluted oscillation probability can be found in [7], here it is just worth noticing the effect of finite detector resolution on the transition probability in Fig 1.1 solid line.

For distances $\langle L \rangle < L^{osc}$, the average transition probability oscillates as the unavenged one. For $\langle L \rangle \gg L^{osc}$ the oscillation pattern is completely wash out by the effect of the detector finite energy resolution and one can only measure the averaged transition probability.

An experiment, with not enough resolution to observe the oscillation pattern, is able to set an upper limit on the averaged transition probability, which implies an upper limit for $\sin^2 2\theta$ as function of Δm^2. It is possible to construct the so-called *exclusion curve* in Fig. 1.2 that separates the allowed region for the parameter $\sin^2 2\theta$ from the excluded one.

Experiments are designed, choosing the appropriate value of L/E to be sensitive to a given value of Δm^2. A show in Fig. 1.1, if one designs an experiment such that, for a fixed Δm^2, the value of L/E is:

$$\frac{L}{E} \approx \frac{2}{\Delta m^2} \tag{1.14}$$

this experiment, would measure the maximal transition probability in the region where it dominates the uncertainties due to energy and space resolutions.
Commonly, oscillation experiments are classified depending on the average value of L/E:

- **Short Baseline (SBL)** experiments. These include experiments whose sen-

sitivity range is:

$$\frac{L}{E} \approx [0.1, 10^2] eV^2 \tag{1.15}$$

Reactor experiments use large isotropic fluxes of $\overline{\nu}_e$ produced in a nuclear reactor by β^- decays of fission fragments of ^{235}U, ^{238}U, ^{239}Pu, ^{241}Pu. A typical energy for ν_e is of few MeV and the source-detector distance is few meters, so that these experiments are sensitive to $\Delta m^2 \approx 0.1 eV^2$ (see Eq. 1.14). The produced antineutrino is detected via inverse beta decay $\overline{\nu}_e + p \rightarrow n + e^+$ and, since the antineutrino energy is below the threshold for the production of μ and τ , then these experiment can only measure the disappearance probability, that is $P(\overline{\nu}_e \rightarrow \overline{\nu}_e)$. Accelerator experiments exploit neutrinos produced in the decay of pions, kaons and muons, with energy of some GeV and baseline of few kilometers. They have access to Δm^2 from some eV up to $10^2 eV^2$.

- **Long Baseline (LBL)** experiments, with a sensitivity:

$$\frac{L}{E} \approx [10^{-4}, 10^{-3}] eV^2 \tag{1.16}$$

These include the Atmospheric neutrino experiments (ATM) where neutrinos are mostly produced by decay of pions and muons produced by primary cosmic ray interactions with the upper layers of the atmosphere. The energy ranges from few hundreds of MeV to 100 GeV , whereas the source detector distance ranges from few km to 10^4 km. Therefore, an atmospheric neutrino experiment is sensitive to $\Delta m^2 \approx 10^{-4} eV^2$. ATM experiments are Kamiokande, Super-Kamiokande, MACRO and MINOS

Other long baseline experiments, based on accelerators, mainly exploits the disappearance of ν_μ placing the detector at distances of few km. Examples are K2K ($\nu_\mu \rightarrow \nu_e$), Minos ($\nu_\mu \rightarrow \nu_e, \nu_\mu$), ICARUS ($\nu_\mu \rightarrow \nu_e, \nu_\tau$), T2K ($\nu_\mu \rightarrow \nu_e, \nu_\mu$) and OPERA ($\nu_\mu \rightarrow \nu_\tau$).

- **Very Long-Baseline (VLB)** experiments, with a sensitivity:

$$\frac{L}{E} \approx [10^{-12}, 10^{-5}] eV^2 \tag{1.17}$$

Solar neutrino experiments (SOL) detect neutrinos generated in the core of the Sun by β decay from fusion reaction of light elements into heavier ones (for example $p + p \rightarrow^2 H + e^+ + \nu_e$,). Neutrinos are emitted with energies that depend on the type of reaction in the range $0.2 - 15 MeV$ with a baseline that is basically the distance of the Sun to the Earth $1.6 \times 10^8 Km$ that gives a ratio of L/E of about $10^{-12} eV^2$.

1.3.2 Three-flavor oscillations and CP violation

The oscillation of ν_α into ν_β in Eq. 1.12 can be generalized in the case of three flavour channels. Using the ultra relativistic approximation $E \approx p$, it is possible to

show that:

$$P(\nu_\alpha \to \nu_\beta) = \delta_{\alpha\beta} - 4\sum_{i<j} \mathrm{Re}[U_{\alpha i}U^*_{\beta i}U^*_{\alpha j}U_{\beta j}] \sin^2\left(\frac{\Delta m^2_{ji}L}{4E}\right) + 2J\sum_{i<j} s_{\alpha\beta;kj} \sin\left(\frac{\Delta m^2_{ji}L}{2E}\right) \tag{1.18}$$

where $\Delta m^2_{ji} \equiv m^2_j - m^2_i$ is the squared masses difference between two mass eigenstates, and $L \sim ct$ is the travelled distance by the neutrino. $s_{\alpha\beta;kj}$ is ± 1 when (α, β, γ) is an even and odd permutation of (e, μ, τ) respectively. J quantity is called Jarlskog invariant [8] and is defined as:

$$J \equiv \mathrm{Im}[U_{e1}U^*_{\mu 1}U^*_{e2}U_{\mu 2}] \tag{1.19}$$

$$= \frac{1}{8}\cos\theta_{13}\sin 2\theta_{12}\sin 2\theta_{13}\sin 2\theta_{23}\sin\delta_{CP} \tag{1.20}$$

If the Jarlskog invariant vanished, from Eq. 1.18 $P(\nu_\alpha \to \nu_\beta) = P(\overline{\nu}_\alpha \to \overline{\nu}_\beta)$ and $P(\nu_\alpha \to \nu_\beta) = P(\nu_\beta \to \nu_\alpha)$ thus, there would be no CP nor T violation. The CP violation is a genuine effect of three neutrino mixing where:

$$\theta_{ij} \neq 0, \;\; \delta_{CP} \neq 0, \pi \qquad m_1 \neq m_2, \;\; m_2 \neq m_3, \;\; m_3 \neq m_1. \tag{1.21}$$

The J value quantifies the level of CP violation. The asymmetry parameter is defined as:

$$A_{\alpha\beta} \equiv \frac{P(\nu_\alpha \to \nu_\beta) - P(\bar{\nu}_\alpha \to \bar{\nu}_\beta)}{P(\nu_\alpha \to \nu_\beta) + P(\bar{\nu}_\alpha \to \bar{\nu}_\beta)} = 4J\sum_{k>j} s_{\alpha\beta;kj} \sin\left(\frac{\Delta m^2_{ji}L}{2E}\right) \tag{1.22}$$

It is possible to show [7] that:

$$A^{CP}_{e\mu} = A^{CP}_{\mu\tau} = A^{CP}_{\tau e} = -A^{CP}_{\mu e} = -A^{CP}_{\tau\mu} = -A^{CP}_{e\tau} \tag{1.23}$$

which means that CP violation does not depend on the oscillation channel.

1.3.3 Matter effect

Neutrinos with energies around MeV have a minimal scattering probability of approximately 10^{-12} while traversing the Earth. Though neutrinos of typical energies pass through the Earth or the Sun with minimal absorption, the presence of matter significantly alters neutrino propagation. This phenomenon, as in optics, is analogous to how transparent media like air or water minimally absorb light but noticeably reduce its speed based on the refractive index (n). Similarly, neutrinos exhibit similar behavior. As matter primarily consists of electrons (rather than μ and τ), neutrino interactions differ between ν_e and $\nu_{\mu,\tau}$, resulting in a flavor-dependent refractive index.

ν_e undergoes both *CC* and *NC* Coherent scattering interactions (neutrino in final state) with electrons or quarks of the ordinary matter, whereas Coherent scattering of $\nu_{\mu,\tau}$ occurs only via *NC* interactions. This effect, also known as MSW-effect, introduces an effective potential V in the Hamiltonian whose eigenvectors are different

Experiment	L[Km]	E[GeV]	A
T2K	295	0.6	0.046
NOνA	800	1.6	0.12
DUNE	1300	2.6	0.20

Table 1.1: Matter effect parameter for current and next long baseline experiments

from the one of the vacuum oscillation problem.

The potential can be expressed as:

$$V_{CC,\alpha} = \begin{cases} \sqrt{2}\, G_F n_e(x) & \alpha = e \\ 0 & \alpha = \mu, \tau \end{cases}, V_{NC,\alpha} = -\frac{G_F}{\sqrt{2}}\, n_n(x) \quad (\alpha = e, \mu, \tau)\,. \tag{1.24}$$

where G_F is the Fermi constant and $n_e(x)$, $n_n(x)$ are the electron and neutron densities in the medium, which depend on the space coordinate x.

A detailed description of the potential is reported in [9]. The solution of the Schrödinger equation with the additional potential described in Eq. 1.24 gives the matter eigenstates $\nu^m_{1,2,3}$. For the purpose of this work, it is relevant to look at the probability of $\nu_\mu \to \nu_e$ where the matter effect is included:

$$\begin{aligned} P(\nu_\mu \to \nu_e) \simeq\ & \sin^2\theta_{23} \frac{\sin^2 2\theta_{13}}{(A-1)^2} \sin^2\left[(A-1)\Delta_{31}\right] \\ & + \alpha^2 \cos^2\theta_{23} \frac{\sin^2 2\theta_{12}}{A^2} \sin^2(A\Delta_{31}) \\ & + \alpha \frac{\cos\theta_{13} \sin 2\theta_{12} \sin 2\theta_{13} \sin 2\theta_{23} \cos\delta_{CP}}{A(1-A)} \cos\Delta_{31} \sin(A\Delta_{31}) \sin\left[(1-A)\Delta_{31}\right] \\ & - \alpha \frac{\cos\theta_{13} \sin 2\theta_{12} \sin 2\theta_{13} \sin 2\theta_{23} \sin\delta_{CP}}{A(1-A)} \sin\Delta_{31} \sin(A\Delta_{31}) \sin\left[(1-A)\Delta_{31}\right] \end{aligned} \tag{1.25}$$

where

$$\alpha \equiv \Delta m^2_{21}/\Delta m^2_{31} \tag{1.26}$$

$$\Delta_{31} \equiv \Delta m^2_{31} L/4E \tag{1.27}$$

$$A \equiv 2VE/\Delta m^2_{31} = 2\sqrt{2}\, G_F n_e E/\Delta m^2_{31}. \tag{1.28}$$

A derivation of the Eq. 1.25 can be found in [10] and [11]. First terms describe the oscillations due to Δm^2_{13} in the so-called 1-3 sector. Oscillation due to Δm^2_{23} (solar of 1-2 sector), in the second term, are suppressed because of α term. The third term is the CP-violating term that depends on the magnitude of the Jarlskog invariant J . In case $\delta_{CP} = \pm\pi/2$ (maximal violation), this term modifies the oscillation probability up to $\pm 30\%$ variation.

The last term embeds the matter effect on the disappearance probability through the value of A that depends on Δm^2_{13} . This means that the matter effect either enhance or suppress the neutrino oscillation probability $P(\nu_\mu \to \nu_e)$ or the antineutrino one $P(\bar{\nu}_\mu \to \bar{\nu}_e)$ depending on the true mass ordering. Values of the matter parameter for different experiments, baseline and energies are shown in Table 1.1.

1.3.4 Experimental evidences

The present understanding of the parameters within the three-neutrino framework has been derived from a diverse array of experiments. These experiments are typically classified according to the parameters to which they are most sensitive, depending on the varied values of L/E specific to each experiment:

- Solar neutrino experiments, sensitive to $\sin^2\theta_{12}$ and Δm^2_{21};
- Reactor neutrino experiments, sensitive to θ_{13};
- Atmospheric neutrino experiment, sensitive to $\sin^2\theta_{23}$ and Δm^2_{31};
- Long-baseline accelerator experiments sensitive to $\sin^2\theta_{23}$, Δm^2_{31} and θ_{13}.

Solar evidences. Various experiments see an 8σ evidence for a $\sim 50\%$ deficit of solar ν_e using radio-chemicals that exploits the capture of electron neutrinos in Chlorine or Gallium (Gallex [12], GNO [13], SAGE [14]). In these experiments neutrinos produced in the Sun by the fusion reaction $p + p \rightarrow d + e^+ + \nu_e$ with $E_\nu > 233keV$ were detected using the weak charge current interaction $\nu_e + ^{71}Ga \rightarrow ^{71}Ge + e^-$. Results were in agreement suggesting deficit in the detected electron neutrino flux from the Sun compared to the models [15].

Experiments as Kamiokande [16] and SuperKamiokande [17] are experiments that use large water tanks to detect Cherenkov light emitted from the elastic scattering of neutrinos with the electrons present in the water $\nu_x + e^- \rightarrow \nu_x + e^-$, with an energy threshold of 7 MeV. Both experiments provided a 6σ evidence for disappearance of $\overline{\nu}_e$ produced by nuclear reactor but neither of the two could tell whether the deficit was due to a wrong model prediction or to neutrino oscillations phenomena.

The smoking gun to the origin of the reduced neutrino flux was given by Sudbury Neutrino Observatory (SNO) [18] a Cherenkov detector in Canada that operated from 1999 to 2006, based on 1 kt of heavy water D_2O sensible to the channels:

- elastic scattering (ES) on electrons : $\nu_x + e^- \rightarrow \nu_x + e^-$;
- inverse beta decay (CC interaction): $\nu_e + p \rightarrow n + e^+$;
- deuterium knockout (NC interaction): $\nu_x + d \rightarrow +p + n + \nu_x$

In these reactions the free neutron is captured by salt dissolved in water causing the emission of 8 MeV photons which in turn convert in e^+e^- pair detected via Cherenkov radiation.

Given that the cross-section for all the three reaction known, it was possible to compare the expected neutrino flux with the measured event rate. The second reaction provide a measure of the absolute ν_e flux, whereas the third reaction gives a measure of the total incident flux regardless of oscillations. SNO reported the following measure [19] of neutrinos coming from ^8B solar reaction chain which:

$$\phi(\nu_e + \nu_\mu + \nu_\tau)^{SNO} = 4.94 \pm 0.21_{stat} \pm 0.36_{syst} \times 10^6 cm^{-2} s^{-1} \tag{1.29}$$

to be compared with the prediction of the total expected flux from Standard Solar Model:

$$\phi_{tot}(\nu)^{SSM} = 5.49^{0.95}_{-0.89} \times 10^6 cm^{-2} s^{-1} \tag{1.30}$$

Moreover, SNO provided a direct measure of ν_e integrate flux and found:

$$R = \frac{\phi(\nu_e)}{\phi(\nu_e + \nu_\mu + \nu_\tau)} = 0.340 \pm 0.023_{stat} \pm 0.030_{sist} \tag{1.31}$$

which clearly indicates that there is a non vanish flux of $\phi(\nu_\mu + \nu_\tau)$ where the total expected flux is in agreement with the Standard Solar Model. This was explained in terms of electron neutrinos oscillation to muon and tau neutrino during their propagation from the Sun core to the Earth.

Lastly, the Borexino experiment [20], a 278 t liquid scintillator detector installed in the Gran Sasso Laboratory (Italy) running since 2007, measured both the ^{7}Be electron neutrino flux and the pep flux. The measured values found are:

$$\phi(^7Be) = (3.10 \pm 0.15) \times 10^9 \text{ cm}^{-2}\text{s}^{-1} \tag{1.32}$$

$$\phi(pep) = (1.6 \pm 0.3) \times 10^8 \text{ cm}^{-2}\text{s}^{-1} \tag{1.33}$$

around 62% of the SSM predicted flux.

These results were confirmed by the KamLAND experiment in Japan [21]. where a significant portion of electricity is generated by nuclear power plants (over 60 GW). Nuclear reactors produce $\overline{\nu}_e$ in the β- decay of neutron-rich fission fragments. The flux and spectrum of antineutrinos depends practically only on the isotopic composition of the material undergoing fission in the reactor. KamLAND is a long baseline experiment that detects $\overline{\nu}_e$ produced by numerous reactors distributed in the central region of Japan (it is located on average 180 km from the reactors), and has studied the disappearance of $\overline{\nu}_e$ and the energy spectrum of the positrons produced in the interaction. The detector consists of 1000 tons of liquid scintillator and is located in the Kamioka mine, where SuperKamiokande [17] is also located.

KamLAND results are well described in the two neutrino oscillation framework Eq.1.12 where $\theta = \theta_{12}$ and $\Delta m^2 = \Delta m^2_{21}$. Solar neutrino experiments and KamLAND measurements agreed and the combined results, shown in Fig. 1.3:

$$\Delta m^2_{21} = (7.53 \pm 0.18) \times 10^{-5} \text{ eV}^2 \tag{1.34}$$

$$\tan^2\theta_{12} = 0.44 \pm 0.03 \tag{1.35}$$

Atmospheric evidences. Cosmic rays are mainly constituted by energetic protons and heavy nuclei that interact in the upper layers of the atmosphere and produce unstable particles which, in turn, via weak decay produce ν_e and ν_μ with an expected 1:2 ratio.

Atmospheric neutrinos have GeV energies and are generated at tens of km above (or below if detecting neutrino from the opposite hemisphere) the detector level. The first indication of neutrino oscillation in the atmospheric sector was given by the Kamiokande experiment, measuring a deficit in the detected ν_μ rate compared to the expected one. Similar deficits were observed by the Irvine–Michigan–Brookhaven (IMB) [23]. A definitive explanation for the observed deficit were provided by the Super-Kamiokande experiment, and confirmed by the Monopole, Astrophysics and Cosmic Ray Observatory (MACRO) [24] and Soudan-2 [25] experiments. Super-Kamiokande provided results on the distribution of the zenith angle for both ν_e and ν_μ and compare them with the theoretical models that exploits the kinematic of

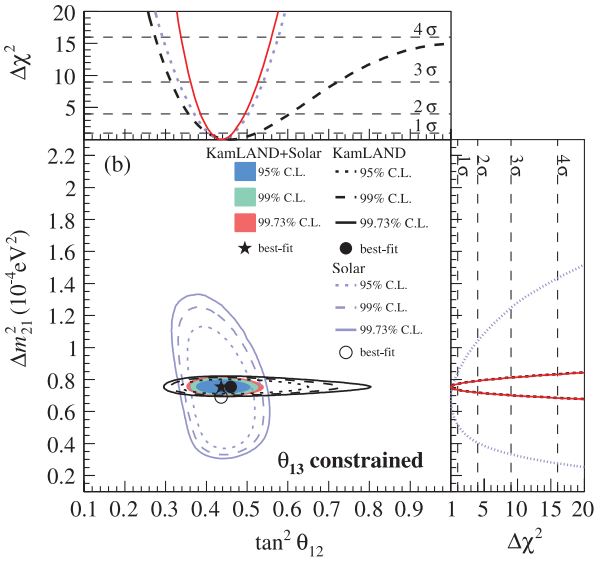

Figure 1.3: Allowed region at different C.L. for the neutrino oscillation parameters from solar data, KamLAND and a combined fit [22].

neutrino-nucleus interaction to constrain the neutrino angle of emission from the direction of the produced charged lepton.

From Eq. 1.12, the probability of observing a given neutrino flavour depends on the ratio $L/\langle E_\nu \rangle$, where L is the distance travelled by the neutrino and span from $L \sim 10$ km for down-going neutrinos and $L \sim 10^4$ km for up-going neutrinos, those that travel through the Earth to the detector, and $\langle E_\nu \rangle$ ranges from 0.5 GeV to 50 GeV. The results presented in Fig. 1.4 show a strong disappearance of up-going ν_μ compatible with two-flavor neutrino oscillation with $\theta = \theta_{23}$ and $\Delta m^2 = \Delta m^2_{31}$.

Recently the ANTARES [26] and IceCube [27] collaborations contributed to the measure of the atmospheric neutrino measurements. These experiments aim to detect neutrinos from the Cherenkov light emitted by muons produced via CC interactions.

Results are show in Fig 1.5 that shows a deficit on the number of detected muon neutrinos in the region of L/E where unoscillated hypothesis would predict more events. The analysis uses neutrinos from the full sky with reconstructed energies from 5.6 to 56 GeV with L/E as long-baseline experiments but with substantially higher-energy neutrinos. The measured values $\Delta m^2_{32} = 2.31^{+0.11}_{-0.13} \times 10^{-3} eV^2$ and $sin^2\theta_{23} = 0.51^{0.07}_{-0.09}$ assuming neutrino normal ordering were consistent with those from accelerator- and reactor- based experiments.

Long baseline evidences. The first two experiments that probed the ν_μ disappearance oscillation channel in the same region explored by the atmospheric sector were KEK-to-Kamioka (K2K) [29] and the Main Injector Neutrino Oscillation Search (MINOS). Both the experiments were in agreement with the previous Super-Kamiokande results as shown in Fig. 1.6.

The two main experiments that have recently played an important role of the atmospheric parameter are NOνA [**a**]nd T2K. Both experiments have provided their best fit for Δm^2_{32} and θ_{23} values and whether data points to either Normal or Inverted mass ordering (see1.4). Values of the mixing angle and mass difference squared are consistent also with previous experiment, as shown in Fig 1.7.

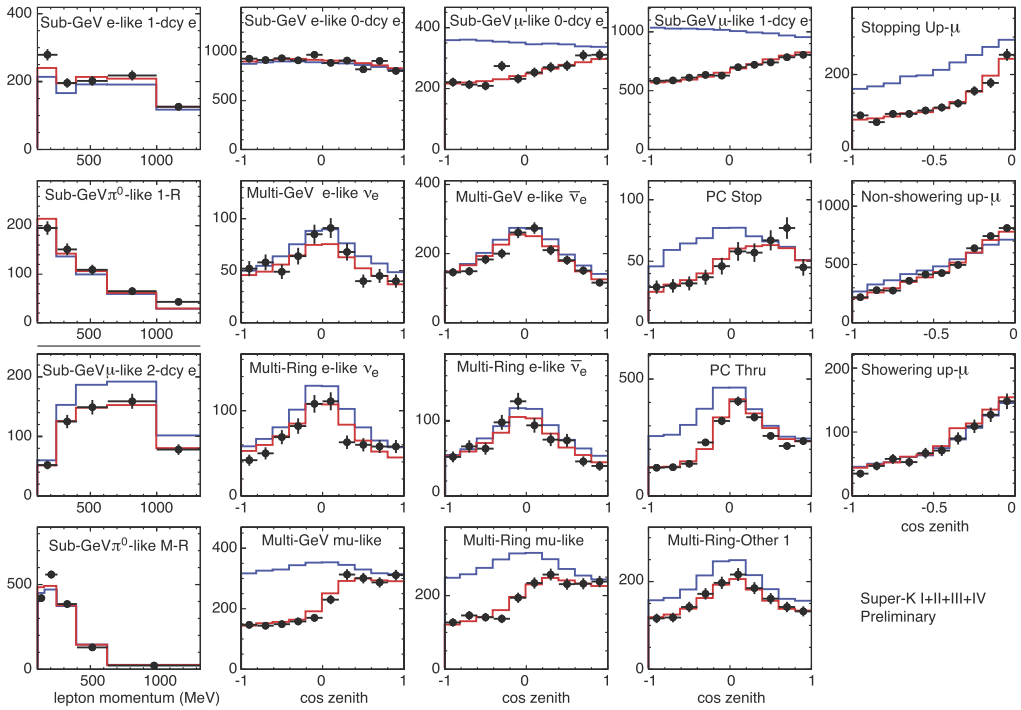

Figure 1.4: Distributions of zenith angle and momentum for muon neutrinos detected by Super-Kamiokande experiments. Blue histograms are the theoretical predictions expected in case of no oscillations and the red ones are the fitted histograms assuming two flavour neutrino oscillations.

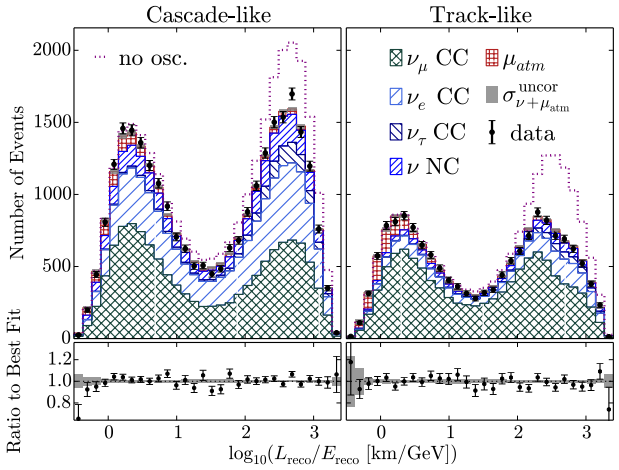

Figure 1.5: : Distribution of the atmospheric neutrinos measured by the IceCube experiment as a function of L/E. The black dots indicate the data along with their corresponding statistical errors. The dotted line shows the expectation in the absence of neutrino oscillations. The stacked hatched histograms are the predicted counts given the best-fit values of all parameters in the fit for each component. The bottom plots show the ratio of the data to the fitted prediction. The bars indicate statistical uncertainties, and the shaded region corresponds to the total uncorrelated statistical uncertainty $\sigma^{uncorr}_{\nu+\mu_{atm}}$ in the expectation. The two peaks represent the down-going and up-going trajectories. A strong suppression of the up-going events is visible due to oscillations [28].

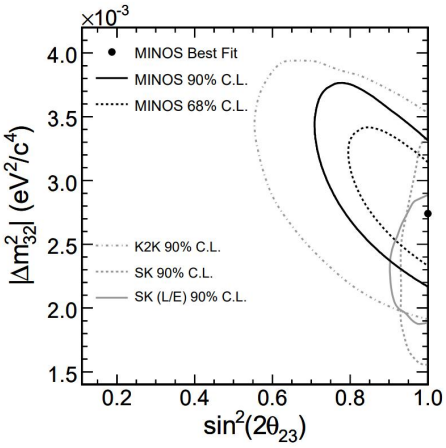

Figure 1.6: Reported Minos confidence intervals [30] for Δm^2_{32} and $\sin^2(2\theta_{23})$ compare to those found for K2K and SK.

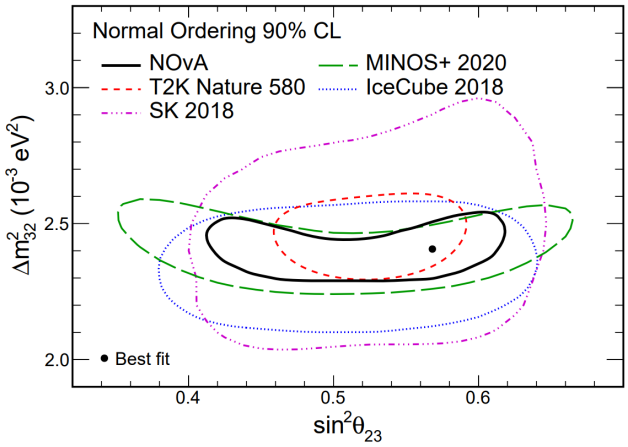

Figure 1.7: The 90% confidence level region for Δm^2_{32} and $\sin^2\theta_{23}$ with the Feldman-Cousin allowed region and the best-fit point for NOνA superposed on contours of other experiments.

Although each experiment reports a mild preference for NO, it has been suggested that a joint fit of the two experiments might converge on an IO solution. Recent results of the two experiments, combined inf Fig. 1.8, show that the T2K best-fit point is in the NO but lies in a region that NOνA disfavor [31]. However, some regions of overlap remain.

Short baseline evidences. Reactor based short-baseline experiments measured θ_{13} mixing angle and Δm^2_{31} using MeV neutrino on 1-2 km baseline measuring the neutrino survival probability. These experiments exploit the e antineutrino induced inverse beta-decay (IBD) in Gadolinium doped liquid scintillators. So far the most accurate measure of the θ_{13} angle is provided by Daya Bay [33] $\sin^2 2\theta_{13} = 0.0851 \pm 0.0024$. Double Chooz[34] and RENO [35] have provided additional measurements but with larger uncertainties. Fig. 1.9 provides a global fit for the three experiments.

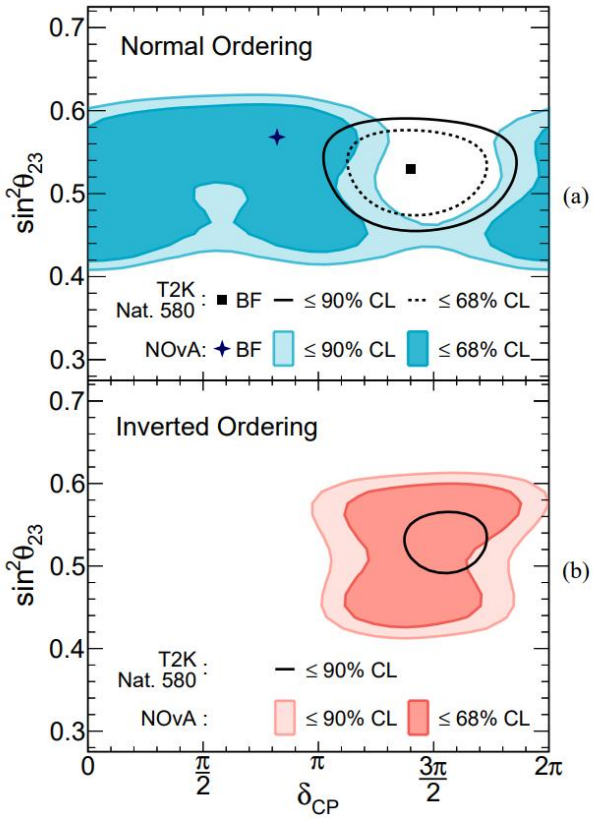

Figure 1.8: The 68% and 90% confidence level contours in $\sin^2\theta_{23}$ vs, δ_{CP} in the (a) normal mass ordering and (b) inverted mass ordering. The cross denotes the NOνA best-fit points and colored region areas depict the 90% and 68% Feldman-Cousins allowed regions. Overlaid black solid-line and dashed-line contours depict allowed regions reported by T2K [32]. Figure reported from [31].

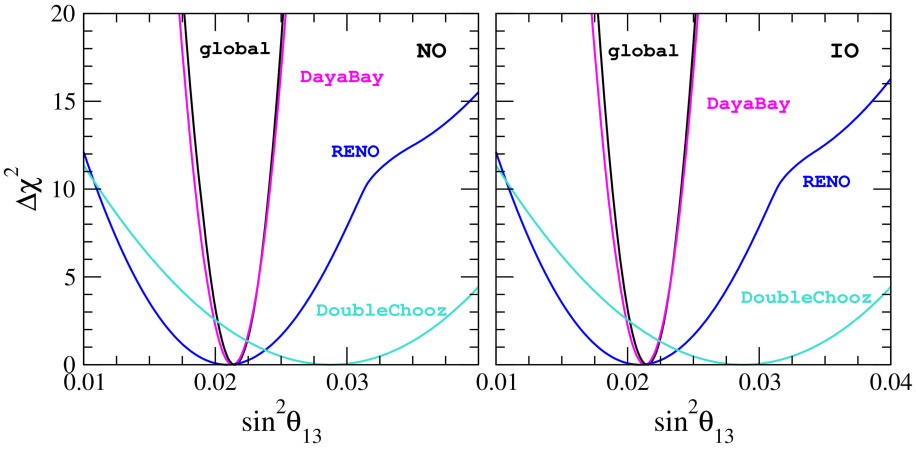

Figure 1.9: Profile of $\Delta\chi^2$ as a function of $\sin^2\theta_{13}$ from global data analysis (black line) and from separate analysis of reactor experiments for both the normal (left) and inverted (right) mass ordering.

1.4 Open questions

1.4.1 Mass ordering

In the minimal scenario of neutrino oscillations within the standard model, experimental results indicate mixing between the three flavor neutrinos, dependent on two distinct squared-mass differences: Δm^2_{21} and Δm^2_{31}. Previously, it was demonstrated in Sec. 1.3.4 that Δm^2_{21} was accurately measured through solar neutrino experiments. The matter effect experienced by neutrinos traversing through the Sun allowed for the determination of the sign of the Δm^2_{21}splitting.

However, the same determination cannot be made for Δm^2_{31}, as measured by atmospheric neutrino experiments, since matter effects are minimal in that context. Consequently, the sign of Δm^2_{31} remains unknown. This uncertainty leads to the possibility of two different neutrino mass orderings based on the sign of Δm^2_{31}:

- spectrum with normal ordering (NO): $m_1 < m_2 < m_3$, with $\Delta m^2_{31} > 0$ and $\Delta m^2_{21} > 0$;
- spectrum with inverted ordering (IO): $m_3 < m_1 < m_2$, with $\Delta m^2_{31} < 0$ and $\Delta m^2_{21} > 0$;

The situation is illustrated in Figure 1.11 that illustrates the flavour content of each mass eigenstate within the 0 to 2π range of the unknown δ_{CP} phase. It is possible to define a lower bound on the sum of the neutrino masses that also depends on the mass ordering:

$$\begin{aligned} \sum m_\nu^{NO} &= m_1 + \sqrt{m_1^2 + \Delta m^2_{21}} + \sqrt{m_1^2 + |\Delta m^2_{31}|} > 0.06 \quad eV \\ \sum m_\nu^{IO} &= m_3 + \sqrt{m_3^2 + |\Delta m^2_{31}|} + \sqrt{m_3^2 + |\Delta m^2_{31}| + \Delta m^2_{21}} > 0.10 \quad eV \end{aligned} \tag{1.36}$$

The current global fit obtained from long-baseline experiments, reactor and solar neutrino experiments show a preference toward the normal mass ordering. The latest global analysis [36] disfavors the inverted ordering by 1.6 σ.

1.4.2 θ_{13} octant

The octant of θ_{23} (whether $\sin^2\theta_{23} < 0.5$ [$\theta_{23} < \pi/4$] or $\sin^2\theta_{23} > 0.5$ [$\theta_{23} > \pi/4$]) remains unknown. The value of δ_{CP} is only poorly constrained. While positive values of δ_{CP} are disfavored, all δ_{CP} values between π and 2π, including the CP-conserving values $\delta_{CP} = 0, \pi$, are consistent with the world's neutrino data. That the best fit to the world's data favors large charge-parity symmetry violation (CPV) is intriguing, providing further impetus for experimental input to resolve this particular question. It is central to the DUNE mission that all the questions posed here can be addressed by neutrino oscillation experiments. Figure 1.12 shows the current fit of $\sin^2\theta_{23}$ for inverted and normal ordering [38]. The bounds on the mixing angle θ_{23} are determined by results from MINOS (green), NOν A (dark-redwood), and T2K (red), with their combination shown in blue. The left panels represent Inverted Ordering (IO), and the right panels represent Normal Ordering (NO). For each experiment, the $\Delta\chi^2$ is calculated relative to the global minimum of both orderings. The upper panels show results using a prior on θ_{23} from reactor experiments, while the lower

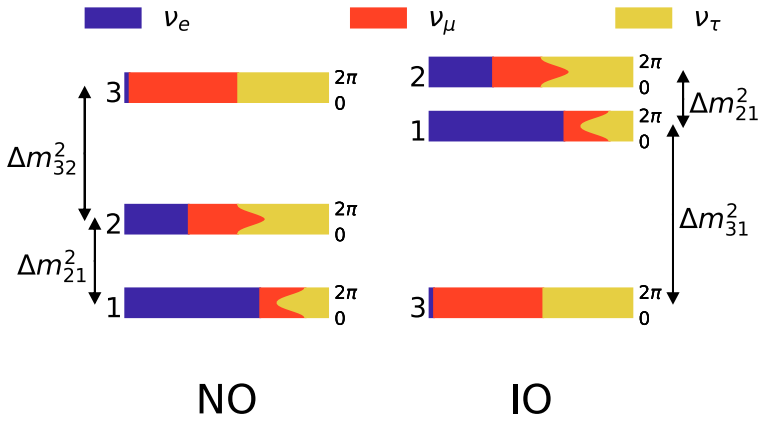

Figure 1.10: Normal and Inverted neutrino mass ordering, depending on the value of the squared mass difference. The colors correspond to the relative composition of each mass eigenstates in terms of flavor eigenstates [37].

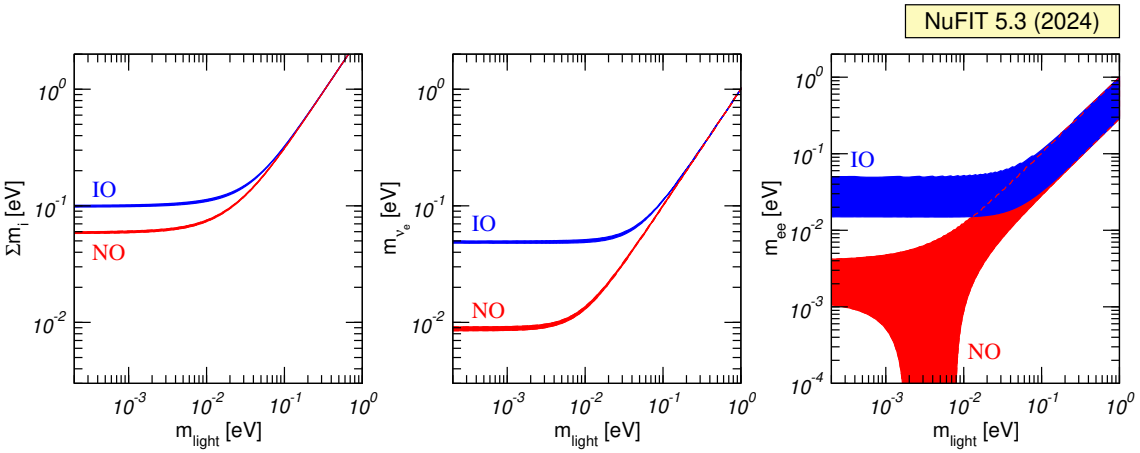

Figure 1.11: Allowed regions for the value of the lightest neutrino mass obtained projecting the results of the global analysis of oscillation data (w/o SK-atm) over the planes $(m_{light}, \sum m_\nu)$ (m_{light}, m_{ee}) . The region for each ordering is defined with respect to its local minimum.

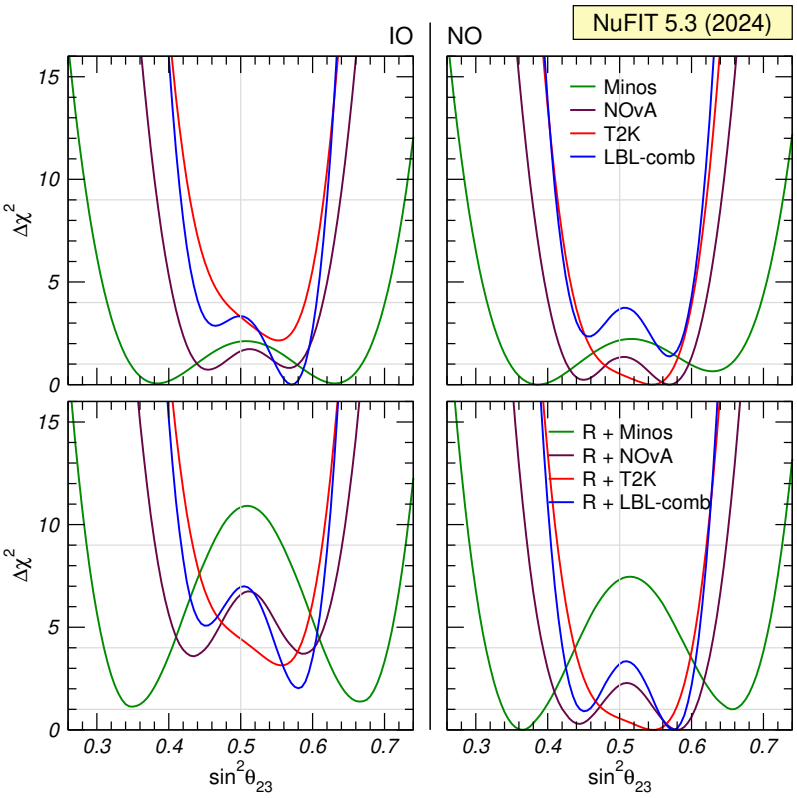

Figure 1.12: Fit of $\sin^2\theta_{23}$ w/o (upper) and w/ (lower) data from reactor experiments [38].

panels incorporate full Long-Baseline (LBL) and reactor data, along with solar and KamLAND data constraining Δm^2_{21} and θ_{12} .

1.4.3 CP violation phase

Figure 1.13 shows the current bounds for δ_{CP} for MINOS (green), NOν A (dark-redwood), T2K (red), and their combination (blue) for inverted (left) and Normal (right) ordering. For NOνA dotted (dashed) lines represent neutrino (antineutrino) data. The upper panels show the $\Delta\chi^2$ results from LBL accelerator experiments, with a prior on θ_{13} to account for reactor data. The lower panels show results with full LBL and reactor information. Solar and KamLAND data constrain Δm^2_{21} and θ_{12}.

1.5 Global fits of neutrino oscillation parameters

The current values of the neutrino oscillation parameters are updated yearly on the basis of the available data from all neutrino oscillation experiments. These are reported in Figure 1.14 that shows the three flavor oscillation parameters from fit to global data of March 2024 [38]. The results compare the effect of including atmospheric neutrino data from Super-Kamiokande (SK-atm) in global neutrino oscillation fits. The upper section shows results without this data, while the lower includes it. esults are provided for both Normal Ordering (NO) and Inverted Ordering (IO). Minimization generally favors NO, except for a difference in the 3σ range

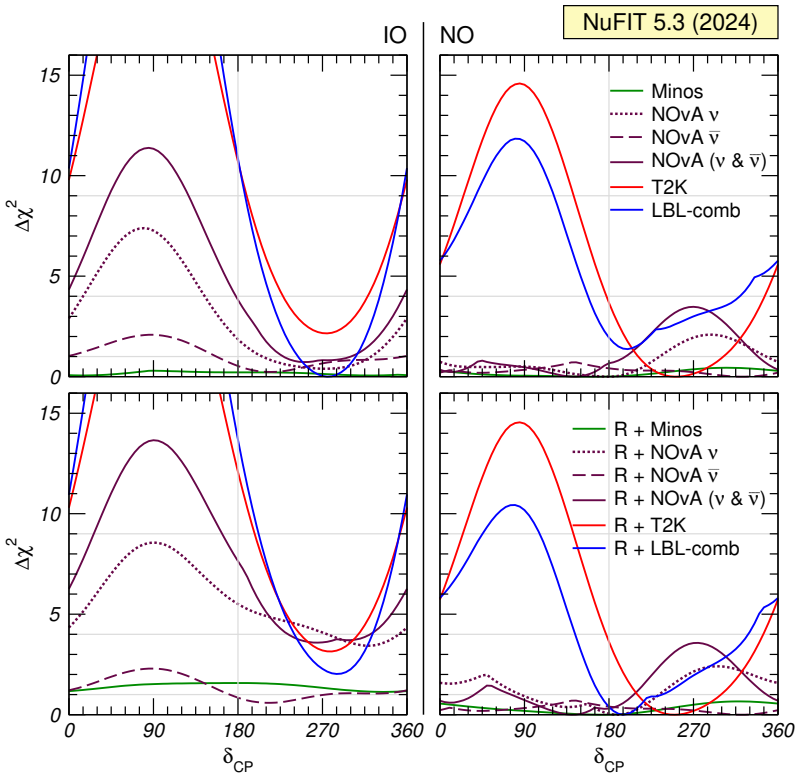

Figure 1.13: Fit of δ_{CP} w/o (upper) and w/ (lower) data from reactor experiments

of Δm^2_{3l} when SK-atm is excluded. Here, $\Delta^2_{31} > 0$ for NO and Δm^2_{32} for IO.

In Figure 1.15 are reported the 3σ confidence level (CL) ranges for the magnitude of the elements in the three-flavor leptonic mixing matrix, assuming the matrix is unitary. These are influenced by correlations between the different matrix entries. This is due to the constraints imposed by experiments, which often restrict combinations of several matrix elements, and the unitarity condition itself. If one element is fixed, the ranges of others are more constrained. The upper (lower) limits are presented with and without the inclusion of Super-Kamiokande atmospheric neutrino data (SK-atm).

NuFIT 5.3 (2024)

		Normal Ordering (best fit)		Inverted Ordering ($\Delta\chi^2 = 2.3$)	
		bfp $\pm 1\sigma$	3σ range	bfp $\pm 1\sigma$	3σ range
without SK atmospheric data	$\sin^2\theta_{12}$	$0.307^{+0.012}_{-0.011}$	$0.275 \to 0.344$	$0.307^{+0.012}_{-0.011}$	$0.275 \to 0.344$
	$\theta_{12}/^\circ$	$33.66^{+0.73}_{-0.70}$	$31.60 \to 35.94$	$33.67^{+0.73}_{-0.71}$	$31.61 \to 35.94$
	$\sin^2\theta_{23}$	$0.572^{+0.018}_{-0.023}$	$0.407 \to 0.620$	$0.578^{+0.016}_{-0.021}$	$0.412 \to 0.623$
	$\theta_{23}/^\circ$	$49.1^{+1.0}_{-1.3}$	$39.6 \to 51.9$	$49.5^{+0.9}_{-1.2}$	$39.9 \to 52.1$
	$\sin^2\theta_{13}$	$0.02203^{+0.00056}_{-0.00058}$	$0.02029 \to 0.02391$	$0.02219^{+0.00059}_{-0.00057}$	$0.02047 \to 0.02396$
	$\theta_{13}/^\circ$	$8.54^{+0.11}_{-0.11}$	$8.19 \to 8.89$	$8.57^{+0.11}_{-0.11}$	$8.23 \to 8.90$
	$\delta_{\rm CP}/^\circ$	197^{+41}_{-25}	$108 \to 404$	286^{+27}_{-32}	$192 \to 360$
	$\frac{\Delta m^2_{21}}{10^{-5}\ \text{eV}^2}$	$7.41^{+0.21}_{-0.20}$	$6.81 \to 8.03$	$7.41^{+0.21}_{-0.20}$	$6.81 \to 8.03$
	$\frac{\Delta m^2_{3\ell}}{10^{-3}\ \text{eV}^2}$	$+2.511^{+0.027}_{-0.027}$	$+2.428 \to +2.597$	$-2.498^{+0.032}_{-0.024}$	$-2.581 \to -2.409$
		Normal Ordering (best fit)		Inverted Ordering ($\Delta\chi^2 = 9.1$)	
		bfp $\pm 1\sigma$	3σ range	bfp $\pm 1\sigma$	3σ range
with SK atmospheric data	$\sin^2\theta_{12}$	$0.307^{+0.012}_{-0.011}$	$0.275 \to 0.344$	$0.307^{+0.012}_{-0.011}$	$0.275 \to 0.344$
	$\theta_{12}/^\circ$	$33.67^{+0.73}_{-0.71}$	$31.61 \to 35.94$	$33.67^{+0.73}_{-0.71}$	$31.61 \to 35.94$
	$\sin^2\theta_{23}$	$0.454^{+0.019}_{-0.016}$	$0.411 \to 0.606$	$0.568^{+0.016}_{-0.021}$	$0.412 \to 0.611$
	$\theta_{23}/^\circ$	$42.3^{+1.1}_{-0.9}$	$39.9 \to 51.1$	$48.9^{+0.9}_{-1.2}$	$39.9 \to 51.4$
	$\sin^2\theta_{13}$	$0.02224^{+0.00056}_{-0.00057}$	$0.02047 \to 0.02397$	$0.02222^{+0.00069}_{-0.00057}$	$0.02049 \to 0.02420$
	$\theta_{13}/^\circ$	$8.58^{+0.11}_{-0.11}$	$8.23 \to 8.91$	$8.57^{+0.13}_{-0.11}$	$8.23 \to 8.95$
	$\delta_{\rm CP}/^\circ$	232^{+39}_{-25}	$139 \to 350$	273^{+24}_{-26}	$195 \to 342$
	$\frac{\Delta m^2_{21}}{10^{-5}\ \text{eV}^2}$	$7.41^{+0.21}_{-0.20}$	$6.81 \to 8.03$	$7.41^{+0.21}_{-0.20}$	$6.81 \to 8.03$
	$\frac{\Delta m^2_{3\ell}}{10^{-3}\ \text{eV}^2}$	$+2.505^{+0.024}_{-0.026}$	$+2.426 \to +2.586$	$-2.487^{+0.027}_{-0.024}$	$-2.566 \to -2.407$

Figure 1.14: Global fits of neutrino oscillation parameters w/ (lower) and w/o (upper) SK atmospheric data based on data available in 2024 [38].

NuFIT 5.3 (2024)

$$|U|^{\text{w/o SK-atm}}_{3\sigma} = \begin{pmatrix} 0.801 \to 0.842 & 0.518 \to 0.580 & 0.142 \to 0.155 \\ 0.236 \to 0.507 & 0.458 \to 0.691 & 0.630 \to 0.779 \\ 0.264 \to 0.527 & 0.471 \to 0.700 & 0.610 \to 0.762 \end{pmatrix}$$

$$|U|^{\text{with SK-atm}}_{3\sigma} = \begin{pmatrix} 0.801 \to 0.842 & 0.518 \to 0.580 & 0.143 \to 0.155 \\ 0.244 \to 0.500 & 0.498 \to 0.690 & 0.634 \to 0.770 \\ 0.276 \to 0.521 & 0.473 \to 0.672 & 0.621 \to 0.759 \end{pmatrix}$$

Figure 1.15: 3σ confidence level (CL) ranges for the magnitude of the elements in the three-flavor leptonic mixing matrix, assuming the matrix is unitary w/o and w SK-atm data.

Chapter 2

The Deep Underground Neutrino Experiment

DUNE will be a world-class, international particle physics experiment that aims to answer fundamental questions about the universe. It is hosted by the U.S. Department of Energy's Fermi National Acceleratory Laboratory (Fermilab). It consists of a FD to be located approximately 1.5 km underground at the Sanford Underground Research Facility (SURF) in South Dakota, at a distance of 1300 km from Fermilab, and a ND that will be located on the Fermilab site in Illinois. The FD will consist of a modular, large, liquid argon time-projection chamber (LArTPC) with a total mass of 70 kt and a fiducial mass of roughly 40 kt. The ND is to be located approximately 574 m from the neutrino source for the LBNF beam, which will be the world's most intense neutrino beam. The ND will consist of several different components described in detail in this volume: a highly modular LArTPC, a magnetized gaseous argon time projection chamber (TPC), and a large, magnetized beam monitor.

2.1 Design and motivation

The LBNF/DUNE strategy has been developed to meet the requirements set by the U.S. Particle Physics Project Prioritization Panel (P5) in 2014. As a benchmark, the P5 report set the goal of reaching a sensitivity to charge-parity symmetry violation (CPV) of better than three standard deviations (3σ) over more than 75% of the range of possible values of the unknown CP-violating phase δ_{CP}. Based partly on this goal, it stated that "the minimum requirements to proceed are the identified capability to reach an exposure of 120 kt per MW per year by the 2035 time frame, the far detector situated underground with cavern space for expansion to at least 40 kt LAr fiducial volume, and 1.2 MW beam power upgradeable to multi-megawatt power. The experiment should have the demonstrated capability to search for supernova neutrino bursts (SNBs) and for proton decay, providing a significant improvement in discovery sensitivity over current searches for the proton lifetime." These requirements are discussed below and in the sections that follow.

Parameter	Phase I	Phase II
FD mass	20 kt fiducial	40 kt fiducial
Beam power	up to 1.2 MW	2.4 MW
ND config	ND-LAr, TMS, SAND	ND-LAr, ND-GAr, SAND

Table 2.1: Summary of parameters for Phase I and Phase II.

2.1.1 Neutrino beam

The neutrino beam will originate from the Long Baseline Neutrino Facility (LBNF) at Fermilab, which utilizes the Proton Improvement Plan II (PIP-II) [39]. This plan will generate a proton beam of up to 1.2 MW from Fermilab's Main Injector, with a potential upgrade to 2.4 MW. The energy of the beam will range between 60 and 120 GeV. The accelerated proton beam will strike a fixed graphite target, producing secondary particles, primarily $\pi^{\pm}$ and $K^{\pm}$, which are then focused by magnetic horns. These particles decay in a 194-meter-long pipe, primarily into $\mu^{\pm}$ and ν_{μ} ($\overline{\nu}_{\mu}$) . An absorber at the end of the decay pipe removes most of the muons, leaving behind ν_{μ}, with a minor presence of ν_e and $\overline{\nu}_{\mu}$ from kaon and muon decays.

By adjusting the polarity of the magnetic field in the horns, it is possible to selectively focus either positive or negative particles. This capability leads to two operational modes of the horn, known as Forward Horn Current (FHC) and Reverse Horn Current (RHC), which produce either a neutrino or antineutrino beam, respectively. The produced neutrinos will have energies peaking between 2-3 GeV and extending up to approximately 10 GeV. This range covers the first two oscillation maxima, which is a distinctive feature of the DUNE experiment.. Figure 2.1 illustrates the unoscillated (anti)neutrino fluxes from a 120 GeV proton beam, while Table 2.2 lists the main parameters of the beam.

Parameter	Value
Energy	120 GeV
POT	7.5×10^{13}
Spill duration	9.6 μs
POT per year	1.1×10^{21}
Cycle Time	1.2 s
Beam Power	1.2 MW
$\Delta p/p$	11×10^{-4} (99%)
Beam divergence (x,y)	(15,17) μrad

Table 2.2: Main parameters of the Phase I neutrino beam [40]

2.1.2 Far Detector Complex

The Far Detector's final design includes four LArTPC modules, each with a mass of 17.5 kton. In DUNE Phase I, only two of these modules, FD1 and FD2, are scheduled for construction. The remaining modules, FD3 and FD4, are planned for Phase II. Both FD1 and FD2 are LArTPCs, but they use different technologies. FD1 is a single-phase, horizontal-drift LArTPC, a design that was successfully tested and validated at CERN using the ProtoDUNE-SP detector, which is roughly 20 times

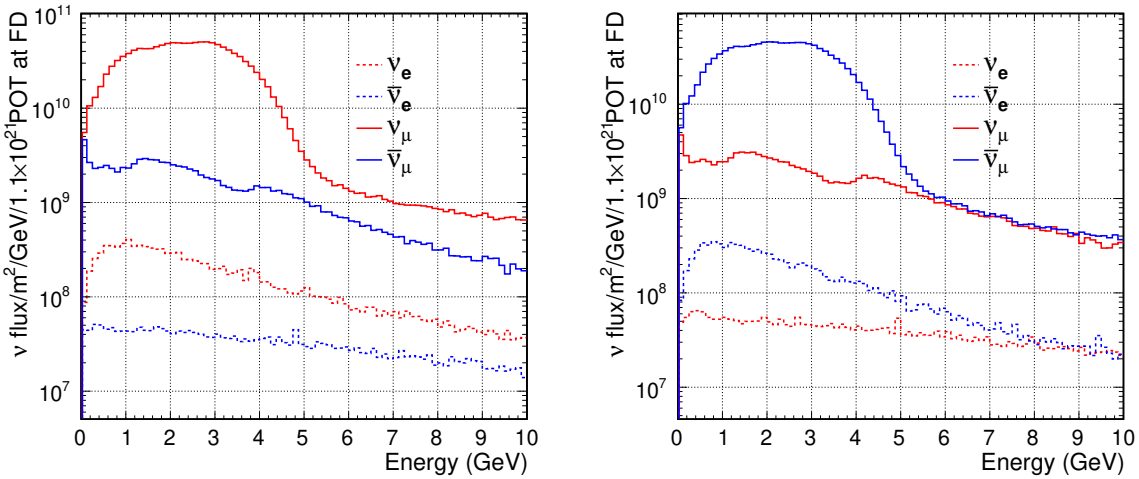

Figure 2.1: Expected unoscillated fluxes at the Far Detector for both muons and electron neutrino with horns working in FHC(left) and RHC(right) modes. [40]

smaller than FD1. FD2 will also be a single-phase LArTPC, but it will feature a vertical drift. The designs for the third and fourth modules have yet to be finalized. Figure 2.2 shows a illustration of the FD cavern with the module dimensions.

Horizontal Drift LArTPC

The DUNE FD1 single-phase horizontal drift LArTPC will be housed within a cryostat measuring 65.8 m × 17.8 m × 18.9 m. This detector will have a total mass of 17.5 kt, with a fiducial mass of at least 10 kt. The design of this first Far Detector module is illustrated in Fig. 2.3 Its internal volume is divided into four drift regions by alternating anode plane assemblies (APAs) and cathode plane assemblies (CPAs). Each drift region measures 58.2 m in length, 3.5 m in width, and 12.0 m in height, with a constant electric field of 511 V/cm generated by applying a -180 kV bias to the cathode planes, causing ionization electrons to drift horizontally toward the anode planes.

The anode walls consist of 50 APAs each, arranged in a 2×25 grid, totaling 150 APAs. Each APA is 6.2 m by 2.32 m and contains three layers of active wires along with ten photon detectors. These wires form a grid that collects the drift electrons resulting from argon ionization. Photon detectors, known as X-ARAPUCAs [41], are used to capture scintillation light, which provides crucial timing information for events. These detectors employ a dichroic short-pass filter to shift the scintillation photons' wavelength, trapping them in a closed box where a SiPM (Silicon Photomultiplier) collects the shifted light, as shown in Figure 2.4. The APA wires' current signals and the X-ARAPUCAs' timing data are used together to reconstruct events. The readout electronics for each pair of APAs in the wall are located at the top of the upper module and the bottom of the lower module, as depicted in Fig. 2.4. The cathode walls consist of 25 CPAs arranged in a 2×25 grid, totaling 100 CPAs. The remaining open sides of the TPC are enclosed by a Field Cage, which ensures that the electric field within the active volume remains uniform to within 1

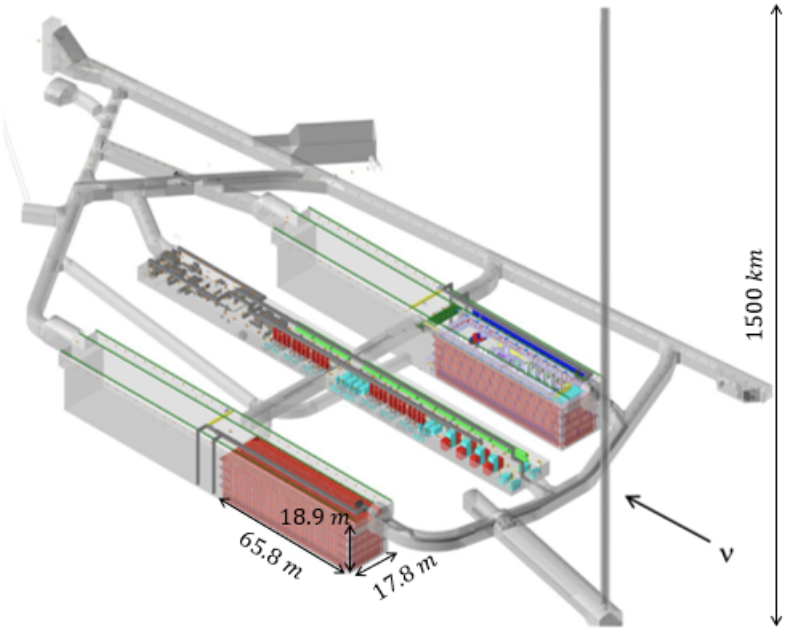

Figure 2.2: FD overview with the location of two underground modules

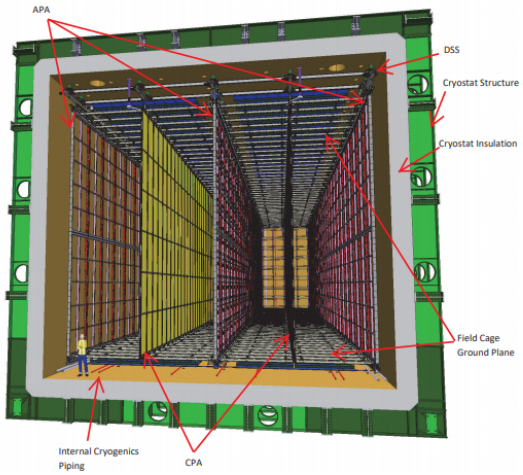

Figure 2.3: Drawing of the Horizontal Drift Far Detector Module 1, showing al ternating APAs, CPAs, the detector support system, the cryostat and cryogenics distribution.

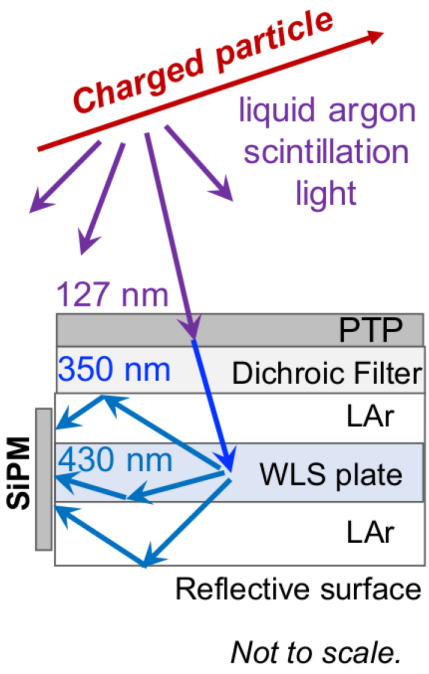

Figure 2.4: Sketch of the working principle of an X-Arapuca [41].

Vertical Drift LArTPC

The FD Module 2 features a vertical drift LArTPC design, as illustrated in Figure 2.5. In this configuration, the cathode is positioned at the mid-height of the module, allowing electrons to drift vertically toward anodes located at both the top and bottom of the detector. Unlike the horizontal drift design, the anodes here are constructed from perforated printed circuit boards (PCBs), which help prevent deformation when positioned horizontally. Each anode consists of two PCBs: the first contains a shielding plane and an initial induction plane, with perforations that allow electrons to pass through to the second PCB, which houses the second induction plane and the collection plane (see Figure 2.6). The two anodes are mounted on charge readout planes, which are different for the top and bottom anodes. The top anode is supported by a stainless steel frame suspended from Kevlar wires, with adjustable positioning to ensure that frame deformation is kept below 10 mm across 3 meters. The bottom anode is supported directly on the cryostat floor. The readout electronics are also distinct for each anode: the electronics for the top anode are located in the cryostat's chimney, while those for the bottom anode are mounted under the support frame (as shown in Figure. 2.7). Similar to the horizontal drift module, the scintillation light in the argon is captured by a photon detection system (PDS), which provides the necessary trigger and timing information for events.

The PDS is installed along the walls of the cryostat and on the surface of the cathode. Its design, depicted in Figure 2.8, is an updated version from the first module and includes 60×60 cm^2 tiles equipped with either 80 or 160 SiPMs. To improve light collection, an X-Arapuca light trap is employed. The SiPMs within the cryostat are powered using a "Power over Fiber" system, which utilizes a high-power photonic laser module and a photovoltaic power converter positioned near the photo-sensors, thus ensuring that the electric field remains unaffected.

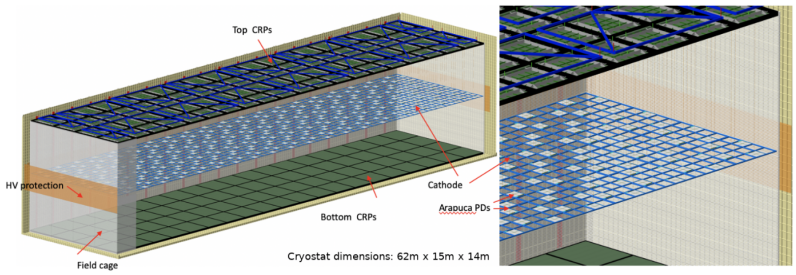

Figure 2.5: Sketch of the full vertical drift module, with a zoomed view of the mounting of the photo-sensors

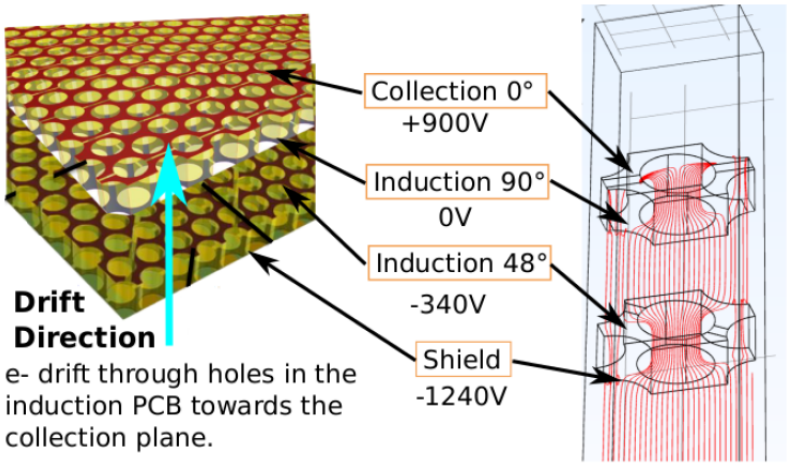

Figure 2.6: Structure of the PCB (left) and electric field simulation between two holes of the anode planes

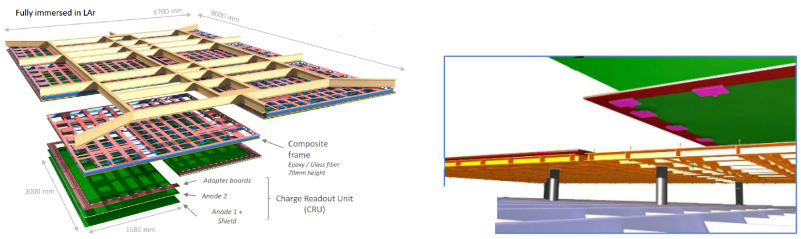

Figure 2.7: Schematic view of the top (left) and bottom (right) charge readout plane of both anodes in the vertical drift module

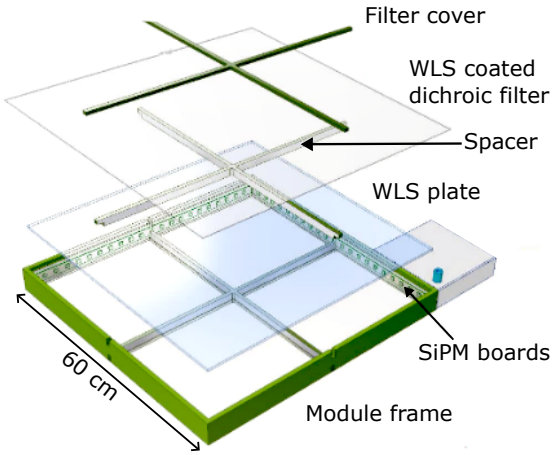

Figure 2.8: Drawing of an x-ARAPUCA detector for the vertical drift module

2.1.3 Near Detector Complex

The Near Detector complex will be situated approximately 600 meters from the neutrino beam source and consists of three main detectors: ND-LAr, the Temporary Muon Spectrometer (TMS) for Phase I of DUNE, which will later be replaced by the gaseous Argon TPC (ND-GAr) in Phase II, and the System for on-Axis Neutrino Detection (SAND). While both ND-LAr and TMS/ND-GAr are mounted on rails to allow them to move off-axis relative to the beam direction, SAND will remain fixed in the on-axis position. The data collection program for off-axis positions is commonly known as Precision Reaction-Independent Spectrum Measurement (PRISM). As mentioned earlier, the Near Detector (ND) is designed to measure the neutrino beam close to its production point, before oscillations can occur. It also plays a crucial role in reducing systematic uncertainties and refining the neutrino interaction model. A brief overview of ND-LAr, TMS, and ND-GAr is provided below, while a more detailed explanation of SAND and its components is discussed in the next section. Figure 2.9 illustrates the positions of the ND detectors, both on-axis and off-axis.

ND LAr

The ND-LAr is a liquid argon time projection chamber (LArTPC) specifically designed to handle the high event rates resulting from the intense neutrino flux at the near site. This innovative design consists of numerous small TPC modules, each optically isolated and equipped with individual pixelated readouts that provide accurate timing information. The current design includes a 5×7 matrix of these modules. The smaller size of each TPC module reduces drift distances and readout times, which in turn helps to minimize event overlap. The data from each module is then combined to reconstruct the full event. The ND-LAr will have a fiducial mass of 67 tons and a total active volume of $5\times7\times3$ m^3, with the capability to detect approximately 10^8 ν_μ events annually. Figure 2.10 provides an illustration of the detector, highlighting one of the module arrays.

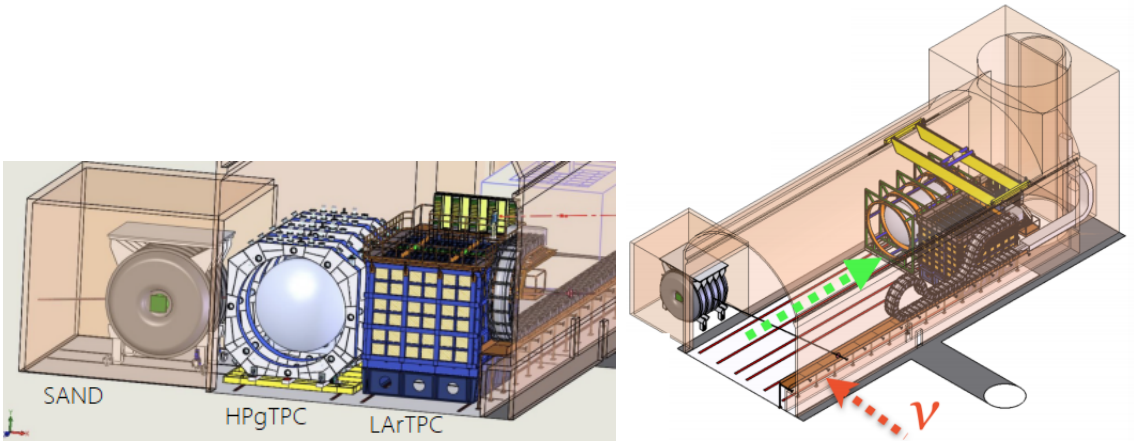

(a) (b)

Figure 2.9: (a) The three detectors of the near detector complex. (b) ND complex with HPgTPC and LArTPC moved along the direction (green) perpendicular to the neutrino beam direction (orange).

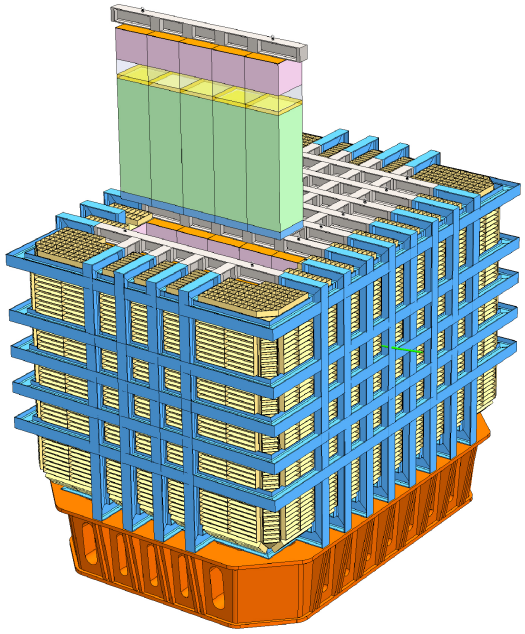

Figure 2.10: Illustration of the ND-LAr detector, highlighting one of the seven rows of five modules.

ND-GAr

The ND-GAr will feature a high-pressure gaseous argon TPC (HPgTPC) enclosed within an electromagnetic calorimeter and subjected to a 0.5 T magnetic field. This setup will enable the reconstruction of muon momentum and charge for events that occur outside the ND-LAr volume. With an approximate fiducial volume of 1 ton, the ND-GAr is expected to detect around 1.6×10^6 ν_μ charged current (CC) events annually when positioned on-axis, providing an independent dataset of neutrino interactions with argon. These events will be analyzed with a low momentum threshold for charged particles, exceptional tracking resolution, and nearly uniform angular coverage, offering systematic uncertainties that differ from those associated with liquid argon detectors. Like ND-LAr, ND-GAr will also conduct PRISM measurements to study off-axis spectra.

SAND

The System for on-Axis Neutrino Detection (SAND) will be the only Near Detector that remains permanently in the on-axis position. SAND's primary role will be to monitor the neutrino flux directed towards the Far Detector, while also facilitating an extensive neutrino physics program. Its design largely incorporates components from the KLOE experiment, including the reuse of the magnet and electromagnetic calorimeter (ECAL). Inside the ECAL, a target/tracking system and a small liquid argon volume are installed. A more detailed description of the SAND detector and its key physics objectives is provided in the following chapter

2.2 Scientific program

The primary science goals of DUNE are to [42]:

- Carry out a comprehensive program of neutrino oscillation measurements using ν_μ and $\overline{\nu}_\mu$ beams from Fermilab. This program includes measurements of the charge parity (CP) phase, determination of the neutrino mass ordering (the sign of $\Delta m^2_{31} = m^2_3 - m^2_1$) , measurement of the mixing angle θ_{23} and the determination of the octant in which this angle lies, and sensitive tests of the three-neutrino paradigm.

- Search for proton decay in several decay modes. The observation of proton decay would represent a ground-breaking discovery in physics, fulfilling a key requirement of the grand unification of the forces.

- Detect and measure the ν_e flux from a core-collapse supernova within our galaxy, should one occur during the lifetime of the DUNE experiment. Such a measurement would provide a wealth of unique information about the early stages of core-collapse, and could even signal the birth of a black hole.

2.2.1 Oscillation parameters sensitivity

The sensitivity to oscillation parameters has been thoroughly evaluated using a complete end-to-end simulation, which includes reconstruction and event selection

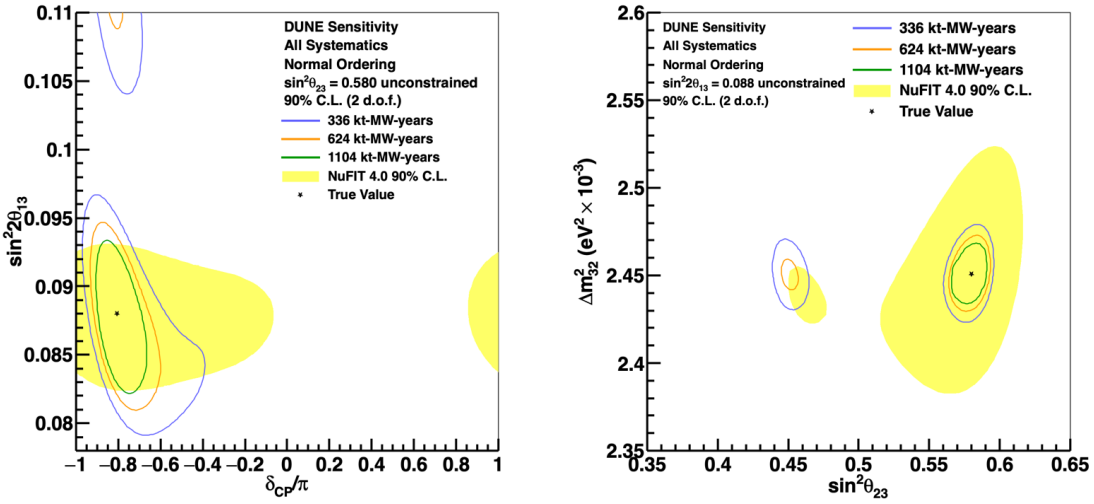

Figure 2.11: 90 % confidence level in the $\sin^2\theta_{23} - \Delta m^2_{32}$ plane (right) for three different values of exposure for neutrino and antineutrino mode. The yellow region correspond to the 90% C.L. of the NuFIT global fit.

processes. This analysis incorporated the geometries of both the Far and Near Detectors, along with flux uncertainties and the neutrino interaction [43]. The results indicate that DUNE will be capable of making precise measurements of long-baseline neutrino oscillation parameters simultaneously, without relying on external constraints. This capability is illustrated in Figure 2.11 which shows the 90% CL regions in the $\sin^2 2\theta_{13} - \delta_{CP}$ and $\sin^2\theta_{23} - \Delta m^2_{32}$ planes for 7, 10, and 15 years of operation. These results are compared with the current global fit from world data, demonstrating how DUNE will be able to resolve potential degeneracies and tightly constrain these parameters. The experiment will also determine the neutrino mass ordering by distinguishing between matter effects and CP violation effects, a process made possible by DUNE's 1300 km long baseline. This long distance enhances the experiment's sensitivity to matter effects, which, result in a significant asymmetry in the oscillation probabilities of neutrinos and antineutrinos, depending on the neutrino mass ordering. At 1300 km, this asymmetry is estimated to be around $\pm 40\%$, a value significantly larger than the maximal asymmetry produced by the δ_{CP} phase enabling DUNE to confidently determine both the mass ordering and δ_{CP} [44]. Figure 2.12 illustrates the sensitivity to these parameters as a function of exposure for a fixed δ_{CP} value. The left panel shows that DUNE will be able to determine the mass ordering with a 5σ confidence level, regardless of the δ_{CP} value, with an exposure of 100 kt-MW-years, equivalent to about 3 years of data. Depending on the values of other oscillation parameters, the same confidence level might be achieved with even shorter exposure times. This is evident in the left panel of 2.13, where sensitivity is significantly influenced by the δ_{CP} value and external constraints on θ_{13}. In the best-case scenario, a 5σconfidence level could be reached in less than a year of data collection. With $\delta_{CP} = -\pi/2$, corresponding to maximal CP violation, 3σ and 5σ confidence levels can be achieved with exposures of 100 or 350 kt-MW-years, respectively. For non-maximal CP violation, a 5σ sensitivity is achievable for half of the δ_{CP} values with 10 years of data, while approximately 13 years are required to achieve a 3σ confidence level for 75% of δ_{CP} [44]. This is illustrated in the right panel of Figure 2.13, where the impact of the θ_{13} constraint

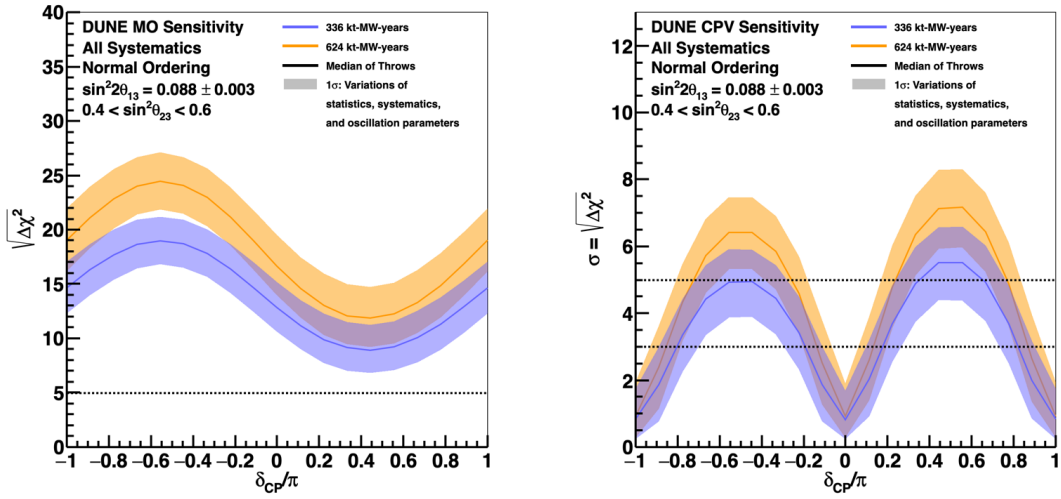

Figure 2.12: Sensitivity to neutrino mass ordering (left) and CP violation (right) with the Phase II Near Detector, shown for different exposure levels as a function of the true δ_{CP} value. The solid lines indicate the median sensitivity, while the shaded bands represent the 68% confidence interval, accounting for variations in statistics, systematics, and oscillation parameters [45].

is again evident.

The $\nu_\mu \rightarrow \nu_\mu$ oscillation probability is particularly sensitive to $\sin^2 2\theta_{23}$ while $\nu_\mu \rightarrow \nu_e$ probability depends on $\sin^2 \theta_{23}$. By measuring both channels, DUNE will be able to probe both the octant and the maximal mixing of θ_{23} . Figure 2.14 shows the sensitivity to the θ_{23} octant as a function of the true value of $\sin^2 2\theta_{23}$ for 10 and 15 years of data collection.

To achieve these precise measurements, DUNE will depend on rigorous control of systematic uncertainties, which will be primarily addressed through measurements made by the Near Detector. The sensitivities discussed in this section were estimated using an advanced treatment of systematic uncertainties that incorporates contributions from both the Far and Near Detectors. The critical role of the Near Detector measurements will be further discussed in 3.

2.2.2 Low energy study of supernovae neutrinos

The substantial mass of the DUNE Far Detector will allow for the detection of low-energy neutrinos in the range of approximately 5 MeV to a few tens of MeV. This capability is particularly significant for observing electron neutrinos from galactic core-collapse supernovas. Given that these events are expected to occur only a few times per century, it is likely that one could be detected during the experiment's operational period. The neutrino signal from a core-collapse supernova evolves over time, beginning with a sharp burst predominantly composed of ν_e neutrinos, corresponding to the neutronization phase of the core collapse.

Following the initial burst, the neutrino signal progresses through the accretion and cooling phases, which last several hundred milliseconds and approximately 10 seconds, respectively. During these phases, the neutrino flux shifts to include nearly equal proportions of all neutrino and antineutrino flavors 2.15. Studying this signal can yield insights into the dynamics of the core collapse, the nature of the

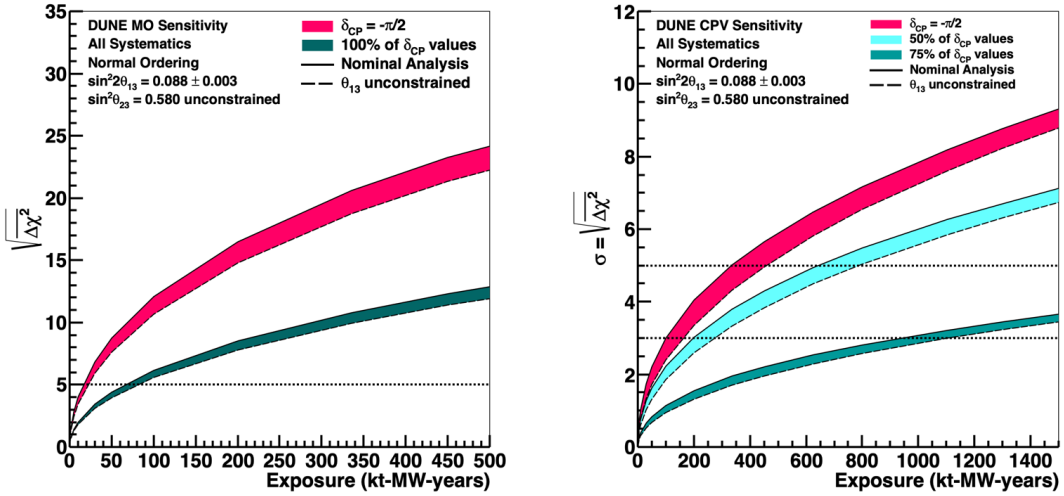

Figure 2.13: Sensitivity to neutrino mass ordering (left) and CP violation (right) with the Phase II Near Detector as a function of exposure in kt·MW-years. The width of the bands illustrates the difference between the nominal analysis (solid line), which includes the external constraint from reactor antineutrino experiments on $\sin^2\theta_{13}$, and an analysis without this constraint (dotted line) [45].

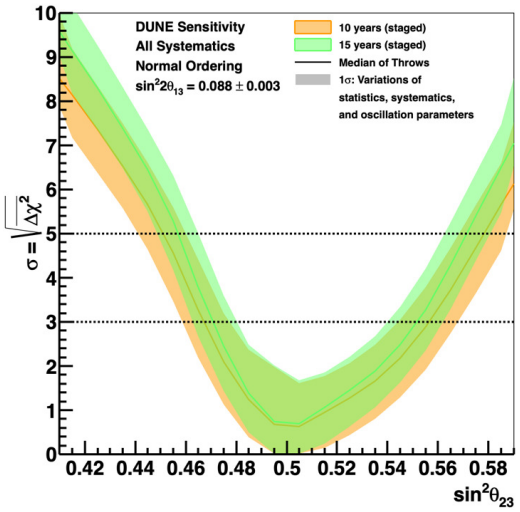

Figure 2.14: Caption

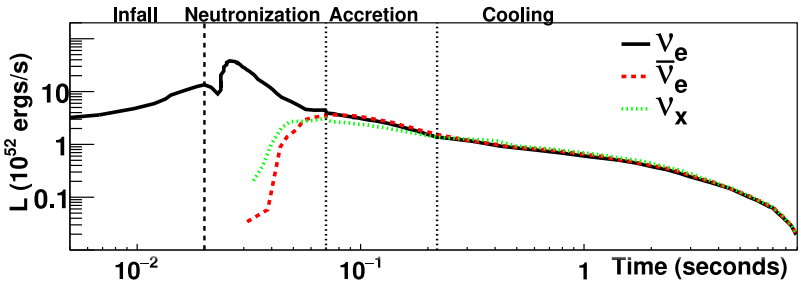

Figure 2.15: Supernova luminosity as function of time from the core bounce of an electron capture supernova, assuming the model in [46].

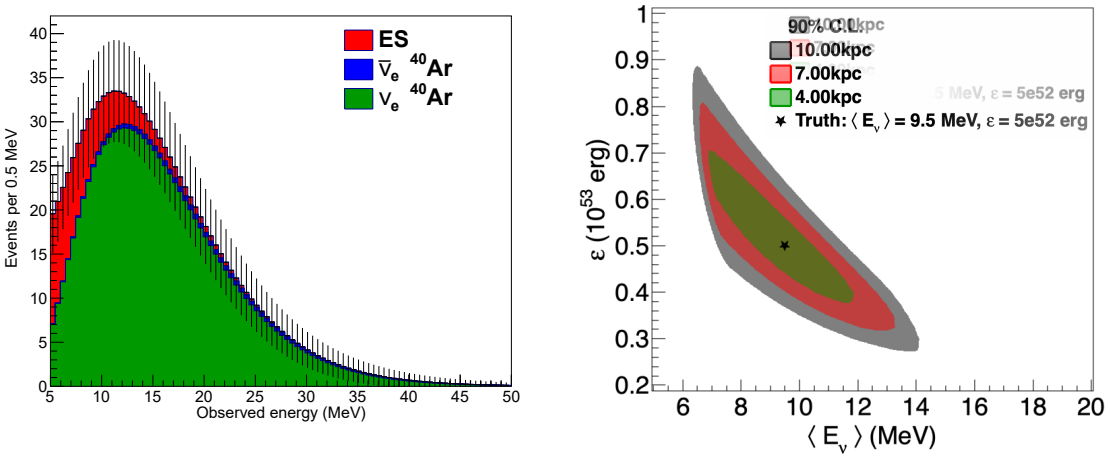

Figure 2.16: (Left) Expected spectrum as a function of the observed energy for the model [48] assuming no flavor transformation. Right: Sensitivity regions to $< E_\nu >$ and supernova energy ϵ for three different supernova distances with 40k fiducial mass.

progenitor star, the explosion mechanics, and also reveal properties of neutrinos themselves. DUNE's sensitivity is primarily to the charged current interactions of electron neutrinos and antineutrinos with argon nuclei, described by the reactions:

$$\nu_e + ^{40}Ar \rightarrow e^- + ^{40}K^* \tag{2.1}$$

These interactions produce a short electron or positron track, followed by gamma rays and other secondary particles as the excited nuclei de-excite. This detection capability is unique to DUNE. Regardless of the specific supernova model, DUNE is expected to observe around 3000 neutrino events from a supernova at a distance of 10 kpc, allowing it to determine the parameters of the electron neutrino spectrum (Figure 2.16). Moreover, by reconstructing the direction of the incoming neutrinos, DUNE can help pinpoint the supernova's location in the sky, contributing to global multi-messenger astronomy efforts.

Additionally, DUNE could investigate the flavor oscillation probabilities of neutrinos during a supernova burst, which are significantly affected by the burst's dynamics. The signal from core-collapse supernovas is also highly dependent on the neutrino mass ordering, with normal ordering expected to suppress the signal significantly. By combining this with DUNE's own measurements of the mass ordering from long-baseline experiments, it may be possible to extract valuable astrophysical information from the supernova signal. Despite the challenges posed by argon's radioactive background, DUNE is also capable of detecting solar neutrinos, leading to significant advancements in the measurement of Δm^2_{21} and in the flux of the *hep* and ^8B solar neutrino fluxes [47]. .

2.2.3 Beyond Standard Model searches

Due to the Far Detector's underground location, which significantly reduces the natural background, DUNE will have enhanced sensitivity to nucleon decay and other rare processes, thereby increasing its potential for BSM searches. Thanks to both the long and short baseline, DUNE will be able to probe a broad range of

possible sterile neutrino mas splitting by looking at the disappearance of charged-current and neutral-current neutrino interactions [49].

Additionally, DUNE foresees an extensive program of dark matter candidate searches, both at near and far detector. With an unprecedented neutrino beam intensity, DUNE can test the production of low mass dark matter (LDM) [50]. The Near Detector will also help to search for heavy particles like Heavy Neutral Leptons (NHLs), where the signal increase with the size of the detector, unlike background events, which depend on the detector mass [51].

DUNE will also be sensitive to baryon number violation processes, such as proton decay in the channel $p \to K^+\overline{\nu}$ or neutron decay as $n \to e^- K^+$. Sensitivities have been evaluated with simulations and, assuming a signal efficiency of 30% , a lower limit on the proton lifetime of 1.3×10^{34} years is foreseen. A more comprehensive description of BSM searches is given in [52].

Chapter 3

The SAND detector

DUNE accelerator-based physics studies rely on assumptions about flux uncertainties, where parameters like horn positions and currents are within set tolerances. While beamline instrumentation monitors these parameters, deviations are best detected by analyzing neutrino energy spectra in the near detector (ND). Beamline distortions are most evident on-axis and become diluted off-axis. The DUNE-PRISM program, which requires the ND-LAr and ND-GAr to collect data off-axis for about 50% of the time, depends on the known relationship between off-axis angles and the neutrino energy spectrum. For DUNE-PRISM to function effectively, beam stability is crucial during data collection, or distortions must be quickly identified and modeled. To ensure this, DUNE employs the System for on-Axis Neutrino Detection (SAND) for continuous on-axis beam monitoring.

Beside the primary goal of monitor, SAND has a rich stand-alone physics program, shown in the following.

3.1 Physics program

3.1.1 Systematic uncertainties constrains

The number of events for a specific process X measured at Near or Far Detectors is:

$$N_X(E_{rec}) = \int_{E_\nu} dE_\nu \; \Phi(E_\nu) \; P_{osc}(E_\nu) \; \sigma_X(E_\nu) \; R_{phys}(E_\nu, E_{vis}) \; R_{det}(E_\nu, R_{rec}) \quad (3.1)$$

where:

- Φ is the incoming (anti)neutrino flux;
- σ_X is the cross-section for the process (QES, RES, DIS) X of neutrino on a given nuclear target;
- R_{phys} is the nuclear smearing, a function that models the effect of primary particles originated from the neutrino interactions to interact with the nucleons before exiting the nuclear target;
- R_{det} is the detector response function (acceptance) for the final state particles;
- E_ν and E_{rec} are the true and reconstructed neutrino energies;

- $P_{osc}(E_\nu)$ is the oscillation probability for a neutrino flavor to oscillate into another flavor.

The measure of P_{osc} as function of the true neutrino energy E_ν is the final goal of DUNE. This requires the accurate measure of the neutrino flavor both at near and far detector, which is not trivial given that terms in equation 3.1 are folded together. Each term has its own uncertainty; flux uncertainties are approximately 8% and arise primarily from uncertainties in hadrons produced off the target and uncertainties in the design parameters of the beamline, such as horn currents and horn and target positioning (commonly called "focusing uncertainties"). The uncertainties on the function R_{phys} are given by the uncertainties in the nuclear models that describe the distribution of nucleon momentum inside the nucleus and on the final state interactions.

As explained in Section 3.2.3, the tracking system of SAND is designed to have a rich sample of Hydrogen as target. Cross-sections of neutrino on free proton have small uncertainties and there are no final state interactions involved in the process (the term $R_{phys} = 1$). This allows to measure the true neutrino energy E_ν once the detector response R_{det} is precisely measured.

3.1.2 Neutrino beam monitoring

SAND will be able to perform on-axis flux measurements of all neutrino flavors at the DUNE near site. In particular, it will measure:

- absolute ν_μ flux from elastic process $\nu\ e \rightarrow \nu\ e$. The experimental signature is just a single electron moving forward in the final state with a very well known cross-section for the process;

- Absolute and relative $\overline{\nu}_\mu$ flux from $\overline{\nu}_\mu\ p \rightarrow \mu^+ n$ QE on H with $Q^2 \sim 0$. For very low Q^2 the cross-section is a constant and determined by neutron β decay;

- Relative ν_μ and $\overline{\nu}_\mu$ fluxes vs. E_ν from $\nu(\overline{\nu}) \rightarrow \mu^\pm\ p\ \pi^\pm$ on H with $\nu < 0.5$ GeV;

- Relative $\overline{\nu}$ flux vs. E_ν from $\overline{\nu} + p \rightarrow \mu^+ + n$ (QE with $\nu < 0.25\ GeV$);

- Ratio of $\overline{\nu}_\mu/\nu_\mu$ fluxes vs. E_ν from coherent π^-/π^+ on C: this is performed by measuring the ratios within the same beam polarity from coherent interactions on C (isoscalar) inside the CH_2 and graphite target;

- Ratio of ν_e/ν_μ and $\overline{\nu}_e/\overline{\nu}_\mu$ from $\nu(\overline{\nu}) - H$ CC interactions;

All these measurements exploit the knowledge of the cross-section of neutrino on Hydrogen. As explained in Sec 3.2.3, SAND will have, in its tracking volume, two types of target, pure graphite (C) and polypropylene CH_2 . From the comparison of selected neutrino event in C and those in CH_2 it is possible to obtain a rich sample of neutrino interactions in free proton (H). This is the foscus of this work and is discussed more in detailed in the Section 6.

3.1.3 Precision measurements and new physics

The availability of large sample of $\nu(\overline{\nu})$-H interactions allows a precision test of the Adler sum rule[1] $S_A = 0.5 \int_0^1 dx/x(F_2^{\overline{\nu}p} - F_2^{\nu p}) = I_p$ which gives the isospin of the target and, in the quark-parton model, is the difference between the number of valence u and d quarks of the target. The value of the S_A can be measured as a function of the transfer Q^2 from the structure functions $F_2^{\overline{\nu}p}$ and $F_2^{\nu p}$ determined from the corresponding differential cross-section on hydrogen. This measurement is sensitive to possible variations of the isospin (charge) symmetry, heavy quark production (charm) and strange sea asymmetries $s - \overline{s}$. Furthermore, the measurement from H can be compared with the values of S_A obtained from the C target for which $S_A = 0$.

From a measurement of the NC elastic scattering off the proton, $\nu_\mu(\overline{\nu_\mu})\ p \rightarrow \nu_\mu(\overline{\nu_\mu})\ p$ it is possible to determine the strange quark contribution to the vector and axial-vector currents of the nucleon, as well as to the nucleon spin Δs. Indeed, in the limit, $Q^2 \rightarrow 0$ the NC differential cross-section is proportional to the axial-vector form factor[2] $d\sigma/dQ^2 \sim (-G_A/2 + G_A^s/2)^2$. This provides the most direct measurements of Δs by extrapolating the NC differential cross-section to $Q^2 = 0$ since in this limit $G_A^s \rightarrow \Delta s$. G_A can be experimentally determined by the measure combined measure of $R_{\nu p}(Q^2) \equiv \sigma(\nu_\mu p \rightarrow \nu_\mu p)/\sigma(\nu_\mu n \rightarrow \mu^- p)$ and $R_{\overline{\nu}p}(Q^2)$.

Finally, a comparison between interactions on H and on the various nuclear targets available in STT can provide a direct model-independent measurement of nuclear effects. In particular, the isospin symmetry provides a determination of the free neutron structure function and hence the one of the average isoscalar nucleon $F_{2,3}^{\nu N} = (F_{2,3}^{\nu p} + F_{2,3}^{\overline{\nu}p})/2$.

3.2 Design

3.2.1 Magnet

The KLOE magnet was engineered to generate a magnetic field of 0.6 T within a cylindrical space measuring 4.3 meters in length and 4.8 meters in diameter. The coil is housed within a cryostat that is 4.40 meters long and 5.76 meters in diameter, situated inside the return yoke. This coil consists of a single conductor layer made from a Rutherford (Nb-Ti) cable co-extruded with high-purity aluminum. Cooling for the coil is achieved by circulating Helium gas at 5.2 K, injected at 3 bar from the cryogenic system and then liquefied into a reservoir in thermal contact with the coil. Figure 3.1 shows the measured solenoidal longitudinal field component during the KLOE installation, compared with the simulation.

[1] $F_2 = x\left(\frac{4}{9}u(x) + \frac{1}{9}d(x)\right)$ where $x = \frac{Q^2}{2pq}$ with $Q = -q$, q is the momentum transferred by the mediator of the interaction to a parton whose momentum is a fraction x of p total nucleon momentum.

[2] G_A is the axial form factor given by $G_A = \frac{g_A}{(1+Q^2/\mathcal{M}_A^2)^2}$ with $\mathcal{M}_A = 1.017 \pm 0.023\ GeV/c^2$ and $g_A = 1.2601 \pm 0.0025$

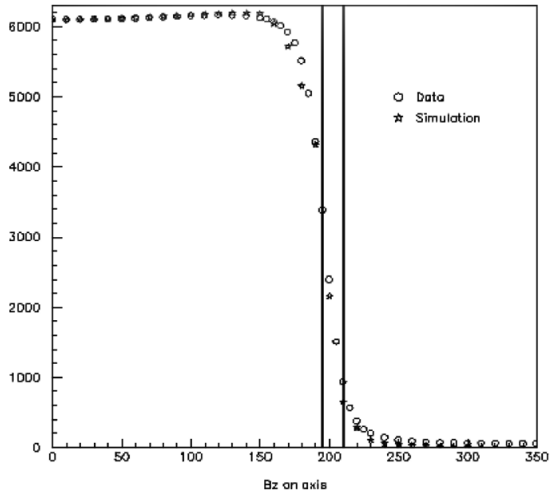

Figure 3.1: KLOE solenoid longitudinal field component (in Gauss) along the magnetic axis.

3.2.2 Electromagnetic Calorimeter

The SAND calorimeter, refurbished from the KLOE experiment [53], is a lead scintillating fiber sampling calorimeter. Scintillating fibers offer high light transmission over several meters, sub-nanosecond timing accuracy, and excellent hermeticity. The calorimeter consists of 24 modules arranged in a nearly cylindrical configuration, with two endcaps each comprising 32 vertical modules. The horizontal modules have a trapezoidal shape, with bases of 52 cm and 59 cm, a length of 4.3 meters, and a thickness of 23 cm. The endcap modules, ranging from 0.7 to 3.9 meters in length, have a rectangular cross-section and both ends are bent into a C-like shape to facilitate insertion into the calorimeter barrel (Figure 3.3a). Each ECAL module is composed of 200 lead foils, each 0.5 mm thick, alternated with 200 layers of cladded scintillating fibers with a 1 mm diameter, all glued together with compatible epoxy. The end faces of each module are divided into a 5×4 grid by light guides, as illustrated in Figure 3.3b, with each cell being read by a phototube, totaling 4880 phototubes. The performance of the calorimeter, evaluated during the KLOE commissioning and operational periods, is [53]:

$$\frac{\sigma_E}{E} = \frac{5\%}{\sqrt{E(\text{GeV})}} \quad \text{and} \quad \sigma_t = \frac{54 \text{ ps}}{\sqrt{E(\text{GeV})}}.$$

3.2.3 Tracking system

The SAND inner tracker, as outlined in the CDR [54], is designed to include the following capabilities:

- low average density $\rho \leq 0.1 g/cm^3$ to minimize multiple scattering and allow precision magnetic spectrometry;
- enough target mass to have enough interaction rate;
- approximately 1 radiation length to allow precise curvature measurements, particularly for $e^{\pm}$;

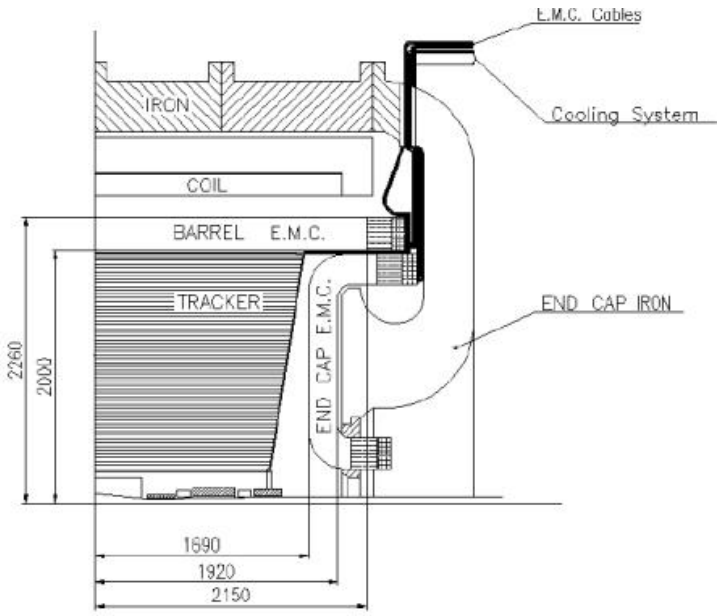

Figure 3.2: Vertical cross-section of the KLOE detector. Units are in mm. Figure adapted from [53]

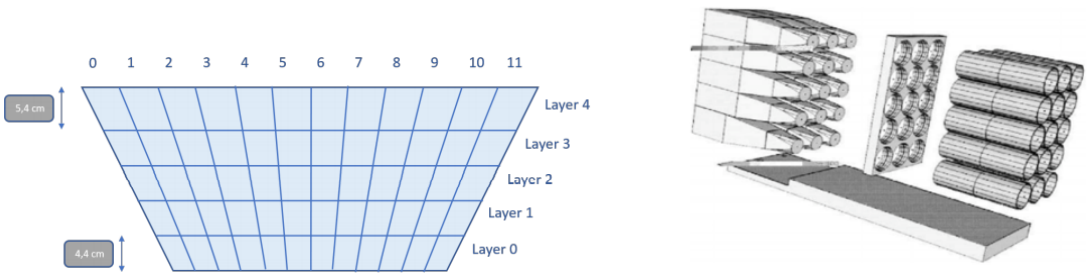

(a) (b)

Figure 3.3: Left: schematic representation of the segmentation of one ECAL module. Right: representation of the light guides at one end of an ECAL barrel module.

- possibility to measure interactions on free protons (hydrogen) by subtracting measurements taken on thin graphite (pure C) and polypropylene (CH2) targets (see 6.1);
- possibility of deploying other nuclear targets to have $\nu - Ar$ versus $\nu - H$ comparison in the same detector (see Section 3.2.4);

There are two viable tracker solutions: a Straw Tube Target Tracker (STT) and a Drift Chamber. Although different, both options distribute target mass uniformly across the tracking volume, maintaining a low overall density while retaining 97% of the total detector mass. This is accomplished by using thin layers of 100% chemically pure material.

Figure 3.4 shows the basic tracking module for the two solutions. Both tracking systems have about the same target mass and average density (~ 0.16 g/cm^3), but the total radiation length is slightly smaller for the STT given the presence of the radiator components, as described in the next section.

STT tracker

The default SST module consists of:

- a 5 mm thick solid polypropylene (CH_2) target slab, whose thickness can be tuned in order to achieve the desired target mass and detector density;
- a polypropylene radiator composed of 105 foils 18 μm thick, alternating with air gaps 117μm thick;
- four layers of straws arranged in an XXYY pattern, with each straw having a 5 mm diameter, 12 µm Mylar walls coated with Al, and a 20 µm tungsten wire coated with gold.

A drawing of the module is reported in Figure 3.4a. The current design has a total number of 86 modules (about 70 with CH_2 target) with a total of 344 straw planes. This configuration foresees about 200k straws, with an average straw length of about 3.2 m giving a total overall length of 700 km.

Drift tracker

The basic volume of this geometry is made of:

- 5 mm (4 mm) solid polypropylene CH_2 (Carbon) target;
- three stations (planes of wires) with alternated signal and field wires spaced along the station by 1 cm. Each station is 1 cm thick and separated from the next one by a 20 μm thickness Mylar plane for a total of 4 planes.

The stations are filled with Ar/CO_2 gas in the proportion 85/15 at 1 atm plus a 10 mbar overpressure and a density 0.002 g /cm^3. The current design foresees 1 module with carbon target, followed by 9 modules with polypropylene target packed in a unique carbon frame that define what we call supermodule.The orientation of wires can be different at each station. For example, at the time of this thesis a solution with wires having +5, 0 and −5 is being studied. For the purposes of this work, wires were simulated with orientation XXY. More details on the design of the chamber are given in the Section 4.1.

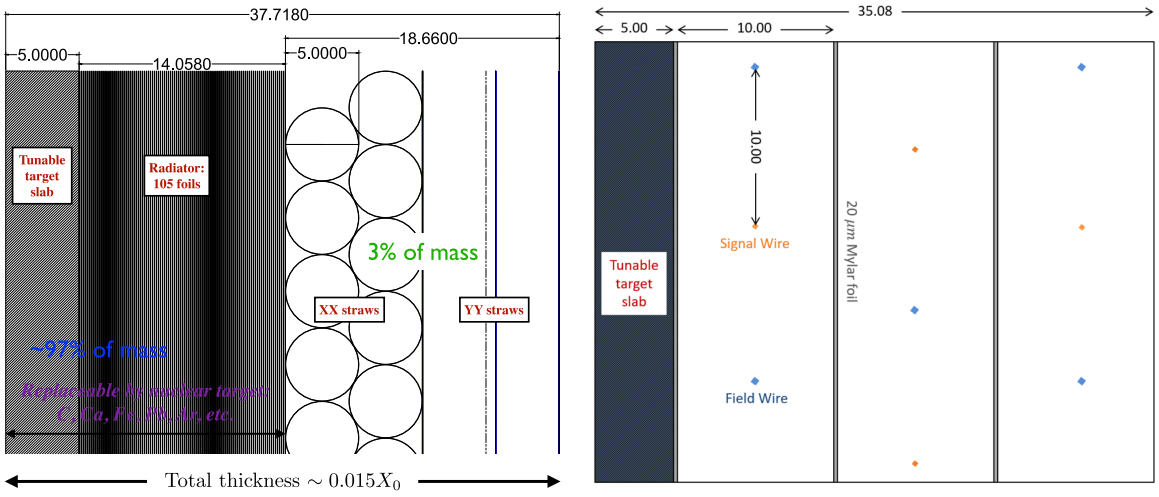

(a) (b)

Figure 3.4: All lengths are in millimeters. Left: default STT module, with a tunable polypropylene target, a radiator, and four layers of straw with a XXYY arrangement. Right : default drift module with a target, three drift planes with alternated field and signal wires interspaced with thin Mylar foils. The height of each module depends on the module position inside the SAND tracking module and can range from about 3 to 4 meters.

3.2.4 GRAIN

In the upstream part of the SAND inner volume, in front of the tracking system, there will be a volume of about 1 ton of active liquid Argon target, GRAIN (GRanular Argon for Interactions of Neutrinos). The insertion of this volume provides on axis data for neutrino-Argon interactions as supplement to those off axis taken by ND-LAr. The design of GRAIN is reported in Figure 3.5. GRAIN is designed not only as a passive target but will also be equipped to actively reconstruct the charged particle trajectories propagating in the LAr volume using only the scintillation light.

While the established technology for tracking and reconstruction with a LAr target is the TPC, the high event rate and pile-up cannot be managed by a traditional TPC due to the millisecond-scale drift time of ionization charges. One potential solution is to use a design similar to ND-Lar, employing arrays of small LArTPCs. Alternatively, a novel R&D program is exploring a tracking and calorimetry system based entirely on imaging LAr scintillation light (see next section). The outer vessel is 190 cm high, 200 cm wide and with a maximum thickness along the beam direction of 83 cm. It is made of multiple layers of Aluminum alloy, honeycomb, and Carbon fiber. The inner vessel is made of Aluminum, with a height of 147 cm, a width of 150 cm and a maximum depth of 47 cm. The overall thickness of vessels- 6 mm was kept as thin as possible to minimize the energy loss, showering and multiple scattering in the passive material.

The design minimizes vessel material, resulting in a thickness that is only a small fraction of a radiation length. The LAr volume's overall depth is kept to just one interaction length to reduce energy loss, showering, and multiple scattering, as outgoing particles will be analyzed by downstream detector elements.

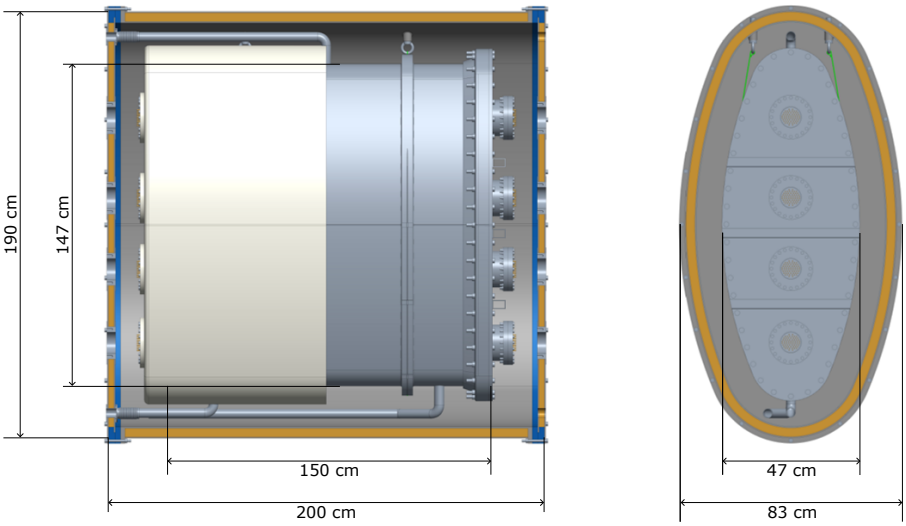

Figure 3.5: GRAIN rendering showing the inner and outer vessels with their dimensions. The inner vessel is made of stainless steel, while the outer vessel is constructed from carbon fiber and honeycomb to minimize external material. A vacuum will be maintained between the vessels to thermally insulate the inner one.

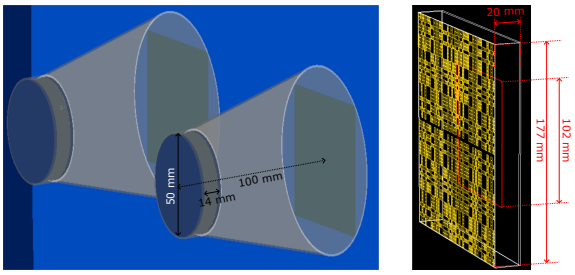

Figure 3.6: 3D models of lens-based (left) and mask-based (right) cameras, both utilizing a SiPM matrix as the sensor behind the optical system. In the left image, blue and grey circles depict the lenses, while in the right image, yellow squares represent the mask.

Photon detection system in GRAIN

GRAIN design is optimized to provide colorimetric information and spatial reconstruction of the neutrino-argon interactions. To this end, an optical system coupled to a fast, segmented photon detector is needed. The light collection in GRAIN is done by instrumenting the inner vessel with Vacuum Ultraviolet cameras operating at LAr temperatures (78 K). Two optical systems are currently being developed, one based on lenses, and one based on Coded Aperture Masks, slabs of opaque material with a certain number of holes (see Figure 3.6). Figure 3.7 shows a simulation of the liquid argon inner volume of GRAIN equipped with coded aperture masks.

Both optical systems have pros and cons. Lens-based cameras provide direct source images but are challenging to construct in cryogenic environments, have limited field of view, and need more space reducing the fiducial volume. On the other hand, mask-based cameras are easier to build, more compact, and provide a larger depth of field, but though they require complex algorithms for image reconstruction. Both use SiPM matrices, currently limited to Hamamatsu S14160 and S13615 arrays [55]. Given the SiPMs poor sensitivity to the 127 nm wavelength of Argon scintil-

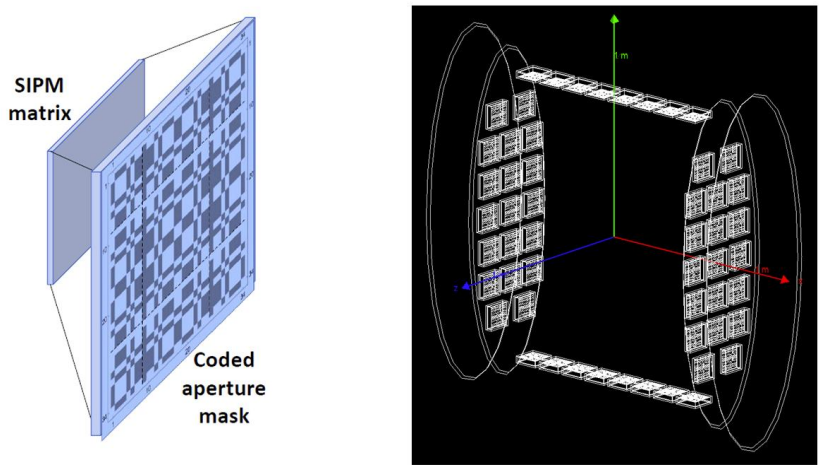

Figure 3.7: Left: Drawing of a coded aperture camera. The mask is perforated, and liquid Argon fills the volume between the SiPM and the mask. Right: placement of coded aperture cameras in GRAIN.

lation light (see Section 3.2.4), a wavelength-shifter (WLS) to convert UV light into visible light, where SiPMs have their optimal photon detection efficiency (PDE) is required.

LAr properties

An ionizing particle crossing a liquid argon volume produces both excitons (Ar^*) and electron-ion pairs ($Ar^+ + e^-$). Both states can interact with other argon atoms, resulting in either an excited molecular state (Ar_2^*) or an ionized molecule (Ar_2^+). The ionized molecules eventually neutralize by recombining with a thermalized electron, once again forming an excited argon molecule, Ar_2^* . This molecule then decays non-radiatively into either the singlet state ${}^1\Sigma_u^+$ or the triplet state ${}^3\Sigma_u^+$, depending on the spin orientation of the excited electron within the excimer molecule:

$$\begin{aligned} \text{Excitation:} \quad & \mathrm{Ar}^* + \mathrm{Ar} \rightarrow \mathrm{Ar}_2^* \\ \text{Recombination:} \quad & \mathrm{Ar}^+ + \mathrm{Ar} \rightarrow \mathrm{Ar}_2^+ + e^- \rightarrow \mathrm{Ar}_2^* \\ \text{Radiative decay:} \quad & \mathrm{Ar}_2^*(1, 3\Sigma_u^+) \rightarrow 2\mathrm{Ar} + \gamma \end{aligned} \tag{3.2}$$

Both single and triplet states decay with the emission of scintillation light of 9.7 eV energy but very different lifetimes: 7 ns for the singlet state ${}^1\Sigma_u^+$ and 1.6 μs for the triplet ${}^3\Sigma_u^+$. These two components of the LAr scintillation light are usually referred to as the fast and slow component, respectively. Figure 3.8 shows the typical scintillation time distribution of liquid argon for different particles, with the narrow peaks and long tails corresponding to the fast and slow component respectively.

The number of emitted photons depends on the total energy deposited by the ionizing particle, with a typical light yield of around 40k photons per MeV of deposited energy. The scintillation photons' wavelength is around 127 nm, in the Vacuum Ultraviolet range [56], [57].

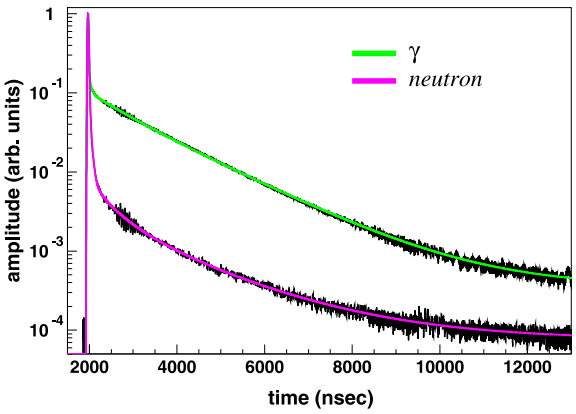

Figure 3.8: Signal shape of liquid argon scintillation light of gammas (green) and neutrons (pink). The first peak of the two distributions in the first bins are the fast component, and the long tails is generated by the slow component [58].

Chapter 4

Simulation Framework

In order to perform the SAND physics analysis, a detail simulation chain was implemented and consists of several steps from the simulation of the geometry to the event reconstruction. Sec. 4.1 describes the implementation of the SAND geometry, mostly developed in this work. The neutrino interactions simulation will be detailed in Sec. 4.2 together with the propagation of the produced particles inside the geometry. Sec. 4.1 describes the simulated electronic response for each SAND component.

4.1 Simulation of the SAND geometry

The General Geometry Description (GGD) [59] is a software officially adopted by the DUNE ND collaboration to generate constructive solid geometries, that is, volumes, of any complexity, constructed starting from basic shapes, such as cubes and spheres, by boolean operations. It is possible to associate to each solid geometry a material and dimensions expressed in units (by means of the Python packages "pint"). The output of *gegede* is a GDML file used to generate neutrino interactions.

As described in Section. 3.2.3 there are currently two solutions for the SAND tracker that were both simulated in this work. A summary of the two configurations is reported in Tab 4.1.

Both solutions are still under study for optimization. The simulation of the two trackers was done in order to perform comparative analysis, running complete neutrino events simulations on both geometry and comparing the physics results. The reconstruction algorithm discussed in Sec. 5.1 and the physics analysis in ref 6 are applicable to the STT tracker as well and will be extended it in the future.

	CH2/C modules	CH2 Mass [t]	C Mass [t]	Radiator Mass [t]	Mylar Mass [t]	Gas Mass [t]	Density g/cm3	Radiation Length [m]
STT	68/8	3.2	0.7	1.3	-	0.1	0.17	2.7
DRIFT	72/8	3.4	0.7	-	0.1	0.1	0.15	3.0

Table 4.1: Main numbers for the two simulated versions of the tracker. The STT-based version does not have clearance between modules, and the thickness of GRAIN is 830 cm.

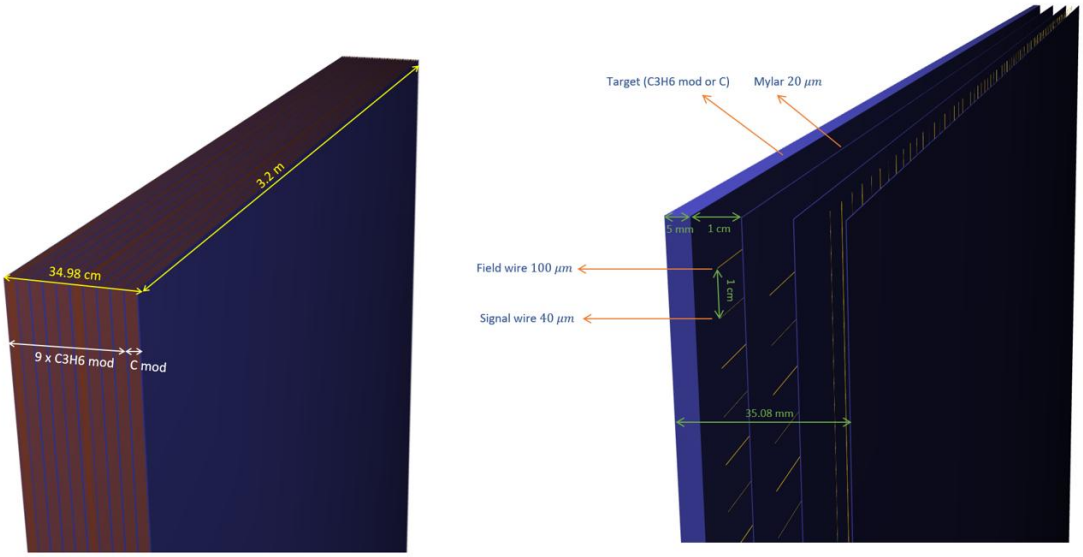

Figure 4.1: Left: Design of one SAND tracker super-module made of 1 C drift module followed by 9 C_3H_6 drift modules. Modules are packed with unique graphite frame of 8 cm thickness, not represented in figure. Right: single C (or C_3H_6) drift module made of a target followed by three layers (also called stations) of wires with orientation XXY. Wires are separated by thin foils of 20 μm mylar.

SAND tracker : Drift chamber and STT tracker

The basic volume of the drift chamber is a single drift module composed by a target followed by three stations (plane of wires). Wires are simulated with XXY orientation, with z being the neutrino beam axis. Total number of simulated signal wires is about 37k. A station consists of alternating signal-field wires spaced 1 cm and 1 cm apart from the Mylar planes. A supermodule is the combination of a drift module with a Carbon target, followed by 9 drift modules with C_3H_6 targets packed inside a unique graphite frame. The illustration of a module and a supermodule is shown in Figure 4.1.

The SAND inner volume, in its current design, is filled with eight symmetrical supermodules with respect to the SAND center. All clearances in the SAND inner volume are aligned with the engineering requirements for the construction. The simulated geometry with the drift chamber as option is simulated in Figure 4.2.

The basic module of the STT tracker is the STT module composed by the target, a radiator and four layers of tubes arrange in XXYY configuration. The SAND inner volume filled with the STT is shown in Figure 4.3. Here each module has diffrent length depending on its position inside SAND. Future simulations are ongoing to include the supermodule structure also in this geometry.

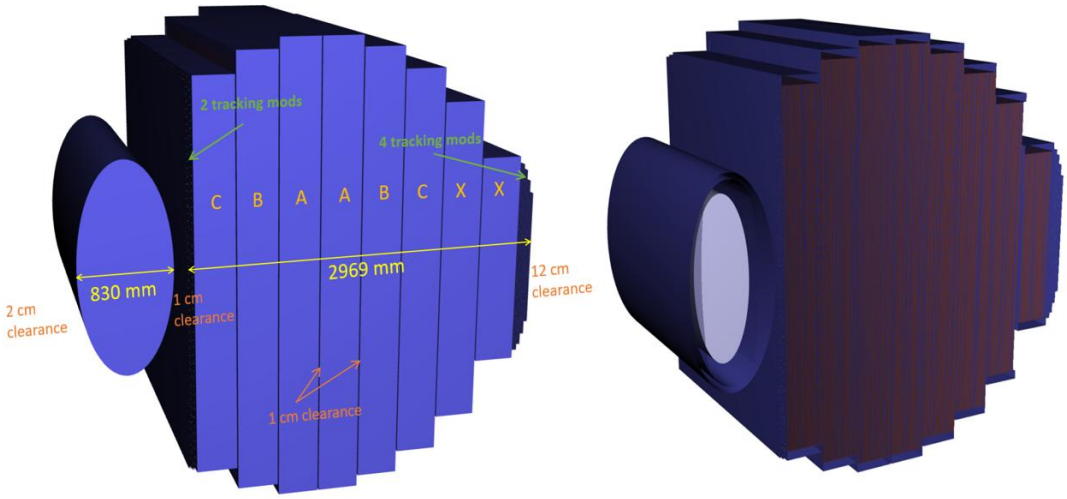

Figure 4.2: Left: SAND inner volume including GRAIN (1 ton liquid Argon active volume) and 8 super-modules, 6 of which with symmetric dimensions with respect to SAND center, plus two additional super-modules placed downstream. Right: Inner structure of GRAIN and supermodules.

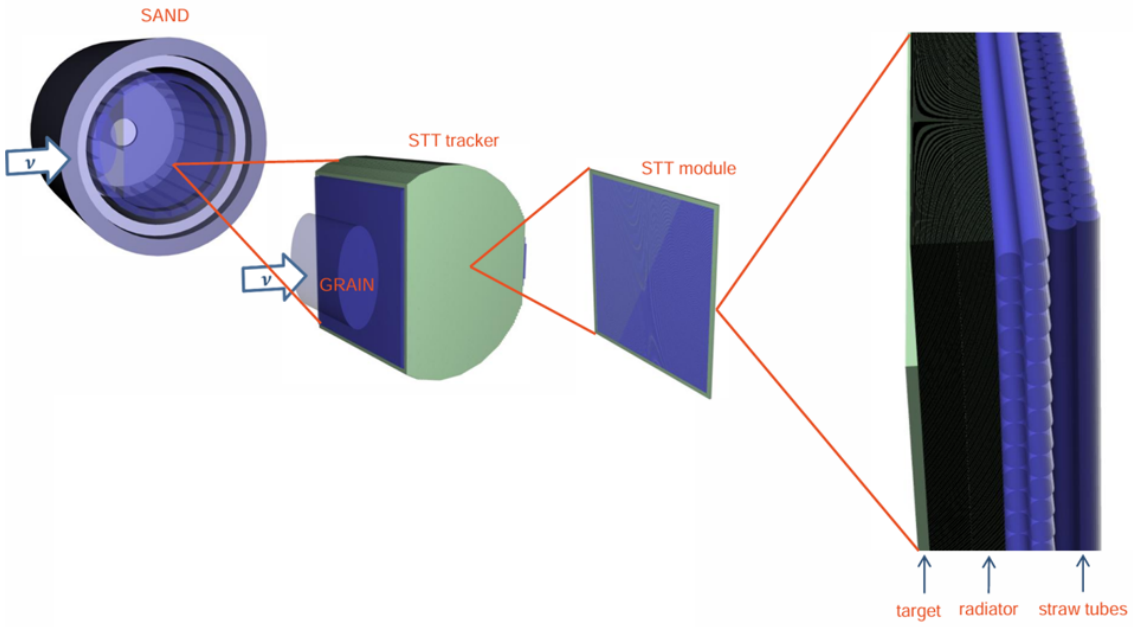

Figure 4.3: Simulation of the SAND tracker in the SAND inner volume. This consists of 82 modules, 8 with Carbon target and the remaining with C_3H_6 target.

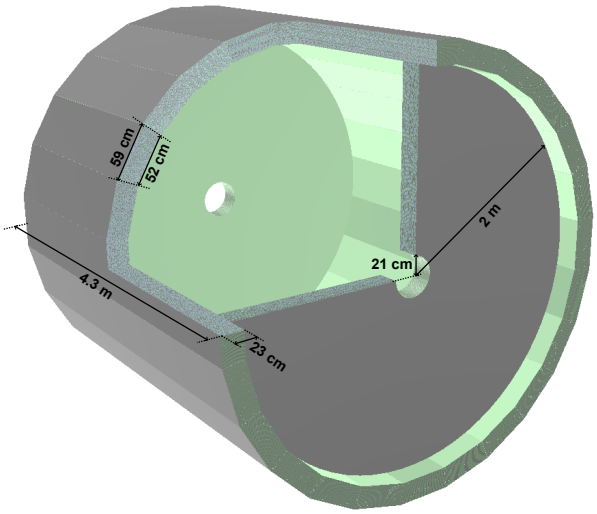

Figure 4.4: Electromagnetic calorimeter geometry with trapezoidal barrel sections and endcaps.

ECAL simulation

The Electromagnetic Calorimeter (ECAL) consists of trapezoidal modules, each 4.3 m long and 23 cm thick, with minor and major bases of 52.5 cm and 59.6 cm, respectively. The ECAL is composed of a total of 24 modules arranged along the profile of a cylinder with a radius of 2 m. The fine structure of each module is simulated by alternating 0.04 cm plastic scintillator slabs with 0.07 cm thick lead slabs, for a total of 418 layers. The endcaps are modeled as disks with a minor radius of 21 cm and a major radius of 2 m. Each endcap is 23 cm thick and divided into 45 vertical modules of varying width and height. A complete view of the calorimeter's geometry is shown in Figure 4.4.

GRAIN simulation

GRAIN: The outer vessel is modeled as a multi-layered structure of carbon fiber and honeycomb, with a total thickness of 62 mm. The endcaps are represented as 16 mm steel plates. The inner vessel is entirely constructed from aluminum. Both vessels are designed as elliptical modules, with the outer vessel having axes of 192.4 cm and 85.4 cm, and a length of 193.2 cm, while the inner vessel has axes of 23.75 cm and 72.8 cm, with a length of 65 cm. The detailed geometry of the cameras inside GRAIN is described in the following section, and an overview of GRAIN's geometry is shown in Figure 4.5.

4.2 Neutrino event generation and particle propagation

The neutrino event generation process relies on the GENIE [60] event generator, a ROOT-based tool [61] widely embraced within the neutrino community. This generator serves as a standard for various beam lines like JPARC and NuMI. While currently focused on the few-GeV range, GENIE aims to expand its applicability

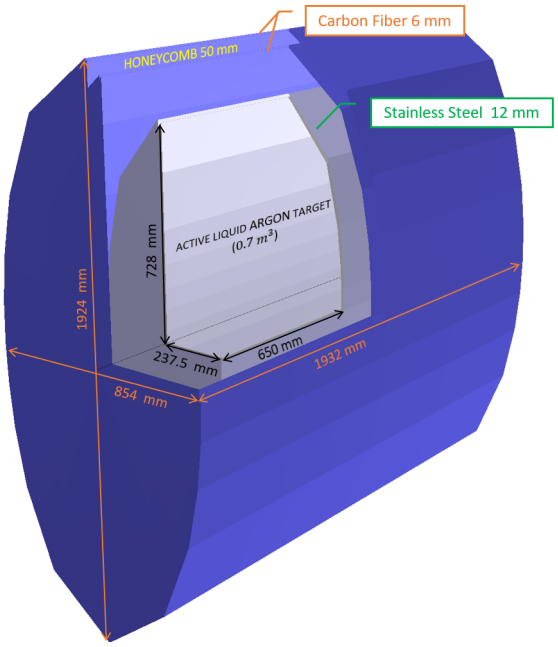

Figure 4.5: GRAIN geometry in the SAND detector. Dimensions are expressed in mm. Both vessels have elliptical shape, the polygonal representation is an effect of the viewer used to render the image.

across all nuclear targets. Its framework encompasses nuclear physics models, cross-section models, and hadronization models, facilitating comprehensive descriptions of neutrino interactions.

GENIE can accommodate both detector geometry and neutrino flux specifications. Leveraging these inputs alongside pre-compiled cross-section libraries, the software determines neutrino energy and interaction types. In the following analysis, all simulated neutrino interactions adhere to the expected LBNF neutrino fluxes (Sec. 2.1.1), calculated at a distance of 574 meters from the horns. These fluxes encompass muon and electron neutrinos and antineutrinos. All the neutrino flux components are reported in Figure 2.1.

After the generation of the neutrino interactions, the primary particles - exiting from the interaction vertex - are propagated in the detector geometry to simulate energy deposition in the various SAND sensible volumes. This step is performed by the EDepSim software [62] a wrapper around the Geant4 simulation tool. It includes a detailed energy deposition model for both ionizing and non-ionizing energy loss cases and, in case of the liquid argon, it uses the NEST (Noble Element Simulation Technique) model.

Edep-sim processes the GENIE output file, providing information about the primary particles produced by neutrino interactions, all the secondary particles produced during the primaries' propagation, and the energy deposit (hit) for each of them. For the last step, it records the starting and stopping position of each deposit, the particle generating the deposit as well as the parent of the depositing particle, i.e. one primary particle or the ultimate parent.

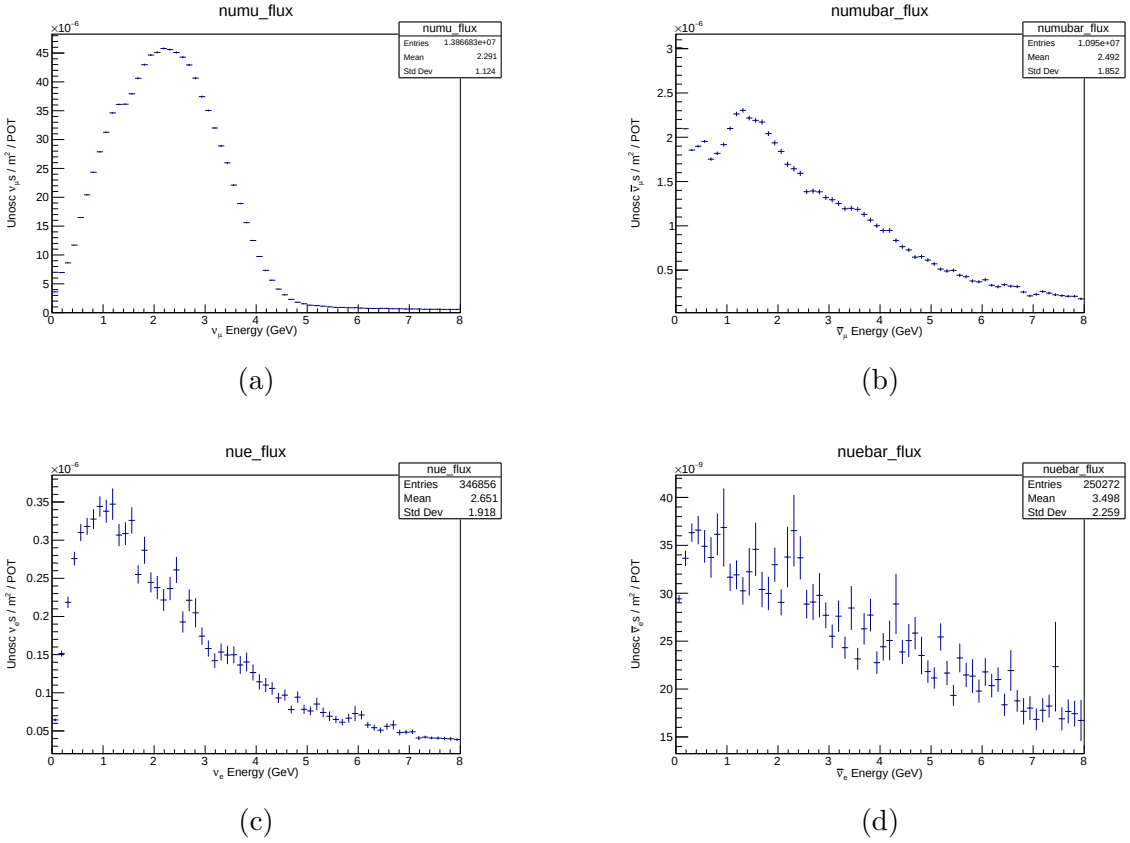

(a) (b)

(c) (d)

Figure 4.6: ν_μ , $\overline{\nu}_\mu$, ν_e ,$\overline{\nu}_e$ neutrino LBNF fluxes used as input for the neutrino event generation in GENIE.

4.3 Detector response simulation

The detector response simulation includes the conversion of the particles' energy deposition (edepsim hits) in the detector sensible volumes into signals as ADC and TDC.

4.3.1 ECAL digitization

The digitization of the ECAL is simulated, dividing each module into a grid 12×5 cells that reproduce the segmentation of the calorimeter readout described in the Sec. 3.2.2 and shown in Figure 3.3. Each cell is read by a PMT on both sides of the module for which a number of photo-electrons, N_{pe} , is computed separately. This procedure takes into account the light attenuation length of the fibers and the energy deposit conversion into photo-electrons. N_{pe} is thus extracted from a Poisson distribution with mean value μ_{pe} given by:

$$\begin{aligned} \mu_{pe} &= dE \cdot A_l \cdot E_{pe} \\ A_l &= p_1 \cdot \exp\left(-\frac{dB}{\text{alt}_1}\right) + (1-p_1) \cdot \exp\left(-\frac{dB}{\text{alt}_2}\right) \end{aligned} \tag{4.1}$$

where A_l is the fiber attenuation length, E_{pe} is the energy to photo-electrons conversion factor, d_B is the distance between the hit position and the PMT, alt_1 and alt_2 are constants. The values of these parameters are reported in the Tab. 4.2.

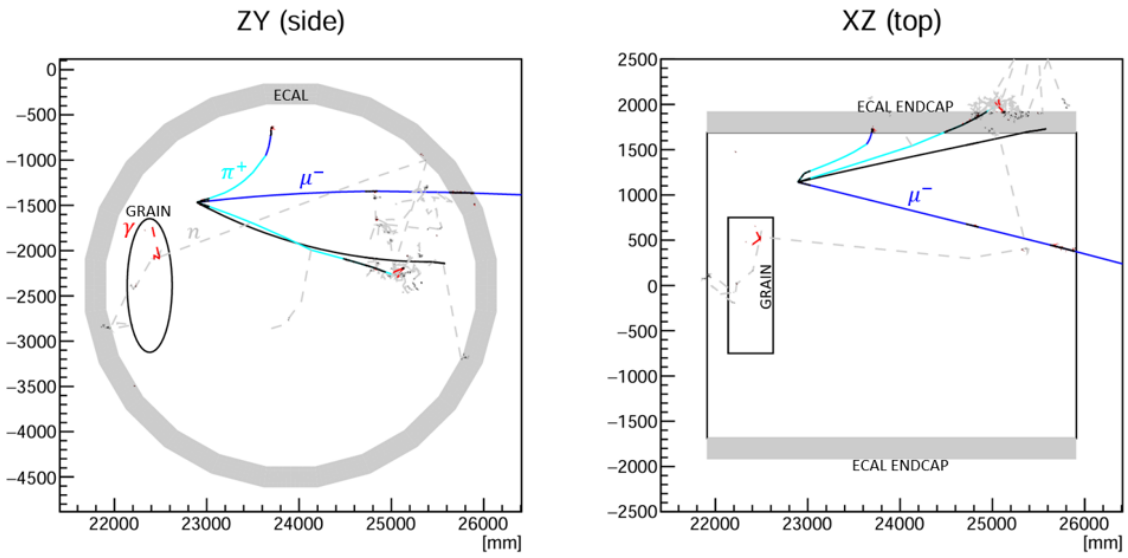

Figure 4.7: Event display of neutrino interaction in SAND in the plane perpendicular to the B field (left) and from the top right. The magnetic field goes along the x-axis. Muon track is blue and typically escape SAND, pions are cyan and neutron are dashed gray lines. They can fly through the tracker with no interaction and get to the ECAL where they can scatter off the lead of the ECAL. Particles entering in GRAIN produce scintillation lights which is represented as dashed red lines in the pciture.

parameter	value
E_{pe}	18.5 eV
alt_1	50 cm
alt_2	330-340 cm
v_{ph}	5.85 ns/m
t_{scint}	3.08 ns
t_{scex}	0.588

Table 4.2: ECAL parameters [53].

For each photon produced in the fiber, an arrival time on the PMT is obtained as:

$$t_{pe} = t_{cross} + t_{decay} + d_B/v_{fiber} + G(1\ ns) \tag{4.2}$$

Here t_{cross} is the time of the hit from the MC truth, t_{decay} is the decay time of the scintillator, and d_B/v_{fiber} is the time of propagation of the photons along the fiber. $G(1\ ns)$ is a Gaussian smearing corresponding to the photo sensor time uncertainty. t_{decay} is obtained applying the same formula used by the KLOE collaboration [53]:

$$t_{decay} = t_{scint}\left(\frac{1}{r_{ph}(1)} - 1\right)^{t_{scex}} \tag{4.3}$$

In Section 5.2 it is described how cells from the digitization steps are grouped to create clusters. The TDC is defined as the time at which the signal recorded on the PMT reaches the 15% of its amplitude (constant fraction method).

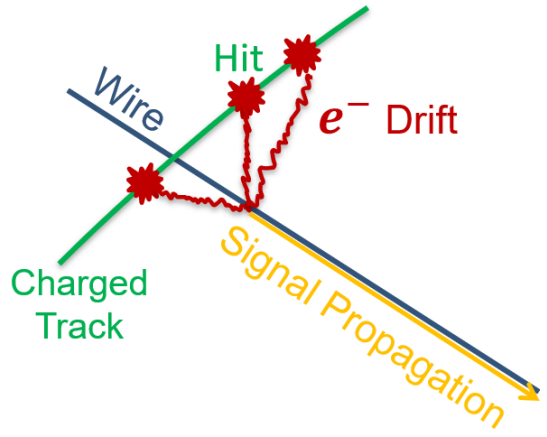

Figure 4.8: Illustration of crossing charged particle that produce ionization around the wire. Electrons drift toward the wire and produce a signal recorded as a TDC.

4.3.2 Drift Chamber digitization

The detector response of the drift chamber was developed in this work. Edepsim gives the energy deposition of each simulated particles in the gas of the drift chamber as hits, that are segments of about 1 mm with constant energy release within the segment. For each segment is found the closest wire that would be then a fired wire by the track. Given a hit and its closest wires, the signal recorded by the wire is a time given by the sum of:

$$t = T_{hit} + T_{drift} + T_{wire} \tag{4.4}$$

where T_{hit} represents the time at which the particles generated the hit, T_{drift} is the drift time calculated assuming a drift velocity of 0.05 mm/ns, and T_{wire} is the signal propagation time in the wire assuming a velocity of 200 mm/ns. The measured TDC for a given wire is the shortest among the times in Eq.4.4 for the segments associated with that wire. The process is illustrated in Figure 4.8. Fig. 4.9 and 4.10 show 2 views of SAND on the zy plane where the particle is bent by the magnetic field and on the xz plane, from the top. The blue dots are the coordinates of the horizontal and vertical wires of the drift respectively and the yellow dots are the wire that have recorded a signal (TDC and ADC) by the passage of the simulated trajectory. Figure 4.11 shows the distribution of the three components in Equation 4.4. The drift time is compatible with a cell of dimension 2 cm^2 and the signal propagation time is compatible with a wire of about 3 meters.

4.3.3 GRAIN response simulation

The scintillation light in GRAIN is simulated from the hits generated by edepsim in the GRAIN LAr volume and converting it to light. The total number of emitted photons is computed considering a light yield of liquid argon as 40k photons/MeV. Fore each hit, a number of emitted photons is extracted from a Gaussian distribution whose mean is equal to the energy deposit times the argon light yield, and whose sigma is the square root of the mean. The wavelength of the photons is extracted randomly from the LAr emission probability distribution reported in [63]. Each photon is emitted at a time extracted from the LAr emission time profile, parametrized

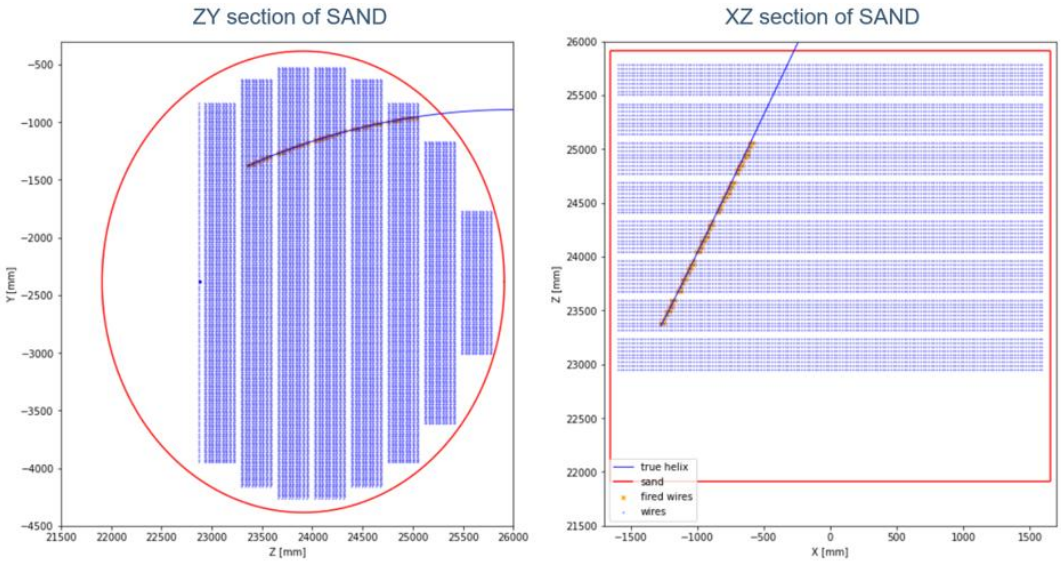

Figure 4.9: SAND zy and xz sections. Blue dots are the coordinates of the wire center with horizontal (left) and vertical (right) orientation. Yellow dots refer to wires fired by the passage of the muon track (blue line).

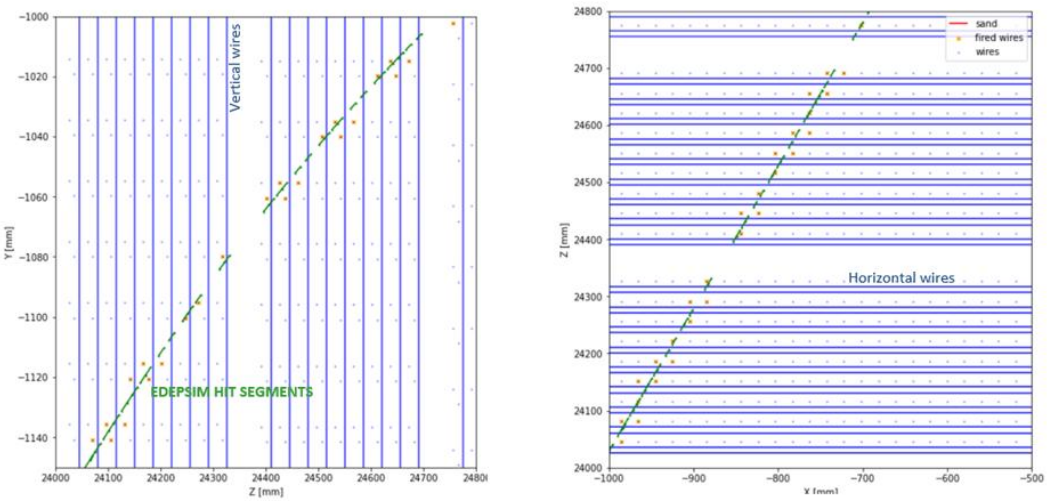

Figure 4.10: Zoom of the Fig. 4.9. Green segments are edepsim hits, that can fire either one or 2 close wires.

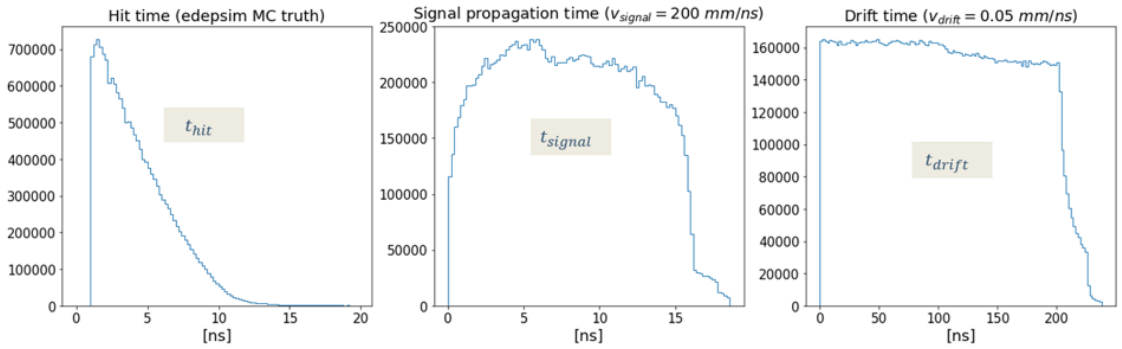

Figure 4.11: Distribution for the components in Equation 4.4 that is: (1) distribution of particle time of flight from vertex to the energy release in the gas (hit), the distribution of the drift times and distribution of the signal propagation times along the wire.

by the fast decay constant of 7 ns and the slow decay constant of 1.6 μs. The value of the single and triplet ration in the range of energy deposition in GRIN is 0.25 and 0.7. The effect of Rayleigh scattering and the absorption is included in the simulation. A more detail description is reported in [64] and [65].

The optical readout of GRAIN is based on SiPM matrices. Each photon is assigned to a pixel (SiPM) of the matrix so that the pixel count a total number of photons that depends on the detection quantum efficiency, the after pulse the dark current rate and the crosstalk. A waveform is simulated for each photon and the final number of photons detected on the pixel is obtained with the time over threshold measurements. This is shown in Figure ??.

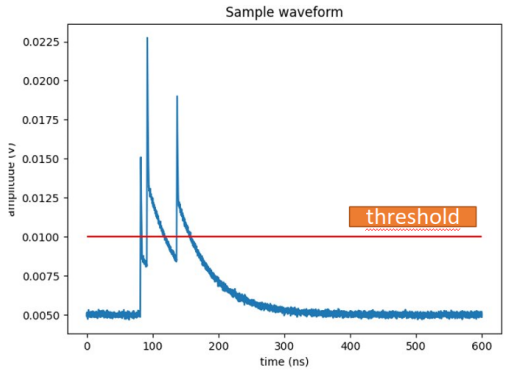

Figure 4.12

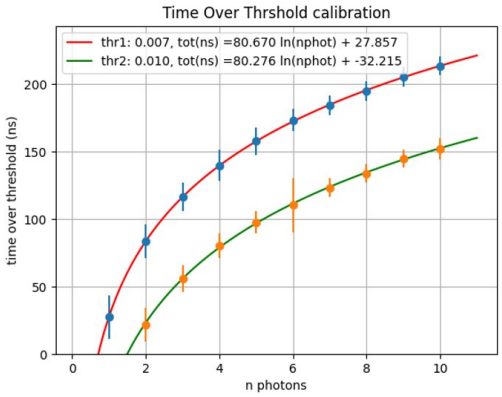

Figure 4.13

Figure 4.14: Left: simulated waveform generated by multiple photon time arrival on the SiPM. The TDC is the time when the signal goes above the fixed threshold in orange. Right: time over threshold as function of the total number of detected photons for two different threshold levels.

Chapter 5

Reconstruction

This chapter outlines the reconstruction methods for each subdetector in SAND. In Section 5.3, a charge track reconstruction algorithm, developed as part of this work, is presented. Although tested using the drift chamber as a tracker for SAND, the algorithm is also applicable to the STT tracker. Section 5.2 describes the clustering algorithm used for particle identification in the ECAL, drawing inspiration from the successful clustering method employed in the KLOE experiment [53]. Additionally, Section 5.3 discusses a strategy for reconstructing charged particle tracks in GRAIN using scintillation photons produced in liquid Argon.

5.1 Track fitting algorithm

The algorithm for reconstructing charged particle tracks in the drift chamber, developed in this thesis, works on drift chamber track reconstructions [66], [67], [68] and has been further refined and adapted for the purposes of this study.

In the following, we shall refer to the presence of a signal on a wire and its relevant information as a "hit". The algorithm's input is a set of hits that have been previously grouped as likely produced by the same particle. Thus, it is assumed that pattern recognition is a preliminary step to the reconstruction step.

5.1.1 Definition of Drift Circle

Charged particles, resulting from ν - nucleus interactions, pass through the drift chamber, generating electron-ion pairs as they move. These ionization electrons, accelerated by the electric fields within each cell, migrate towards the anode wires and producing a signal. Each ionized charge that contributes to the signal, takes a time t to get to the detection point at the end of the wire length:

$$t = t_0 + t_{tof} + t_{drift} + t_{signal} \tag{5.1}$$

where t_0 is a time offset, t_{tof} is the particle time of flight from the track origin to the ionization point, t_{drift} is the drift time, that is the time electrons take to reach the anode with a velocity v_{drift} typically of the order of 0.05 mm/ns, and t_{signal} is the propagation time of the signal along the wire assuming that the signal travels at speed $v_{signal} \sim 200$ mm/ns. The pulse recorded on the wire has a duration and an amplitude that depends on the total charge deposited on the wire. The input of the algorithm is not the entire pulse shape of each wire but rather its TDC, which

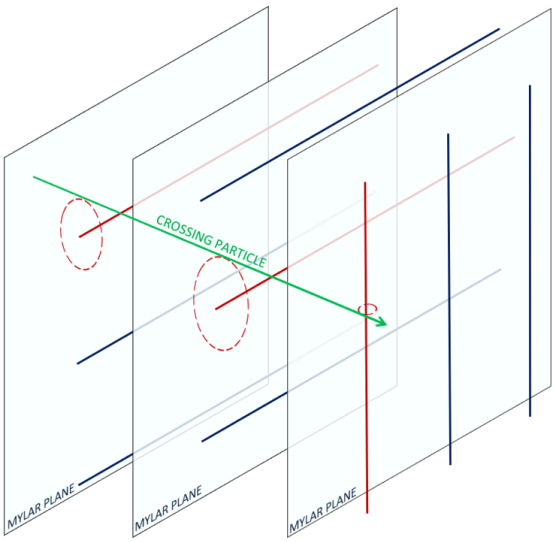

Figure 5.1: Illustration of a crossing charged particles through three station with orientation XXY. As the particle crosses each layer, it ionizes the gas and the signal is collected by the closest wire (red in the picture). The dashed circles are the drift circles tangent to the particle trajectory. The drift circle is obtained as the distance between the particle's trajectory and the wire.

is taken as the smallest among the times t (Eq. 5.1) recorded on the wire. Thus, in the following, Equation 5.1 t is considered the definition of TDC.
Assuming a radial electric field around the wire, where an ionized charge moves toward the wire in a straight line, the TDC is generated by the charges created when the particles reach their closest point to the wire (distance of the closest approach). In a real case scenario, it is possible to infer t_0 and t_{tof} in Eq. 5.1 by using the timing information provided by the experiment's global trigger. As far as t_{signal} is concerned, this not trivial to estimate, because the point where the signal originated along the wire is unknown. However, in the Section 5.1.3, this problem is solved combining the information from multiple wires.
Eventually, one can estimate the drift time t_{drift} from the measured TDC whose value, multiplied by the drift velocity, defines a circle around the wire often referred to as *drift circles*. All the points along a drift circle are compatible with the observed wire's TDC. [1] For a single track passing through the tracker, its trajectory is just the common tangent to a collection of drift circles obtained from the wires fired by the track. The situation is illustrated in Figure 5.1.

For each pair of wires, there are four possible tangent lines to the drift circles along which the particle's trajectory may lie, out of which only one is physical, and the others are referred to as "ghost tracks". The degeneracy can be resolved by combining information from more than three drift circles. Since the particle is immersed in a magnetic field, its trajectory can be approximated as a straight

[1] This is true if one is able to estimate t_{signal} which defines the coordinate, along the wire, where the drift circle lies on. In general, the sum $t_{signal} + t_{drift}$ defines a frustum of a cone around the wire, whose points are compatible with the measured TDC. The minor base of the frustum is close to the wire's readout end, where $t_{signal} = 0$ and its major base is at the opposite end, where $t_{signal} = \frac{L_{wire}}{v_{signal}}$.

line only locally. The reconstruction of the trajectory requires the definition of a track model whose parameters are found, requiring the track to be tangent to all drift circles within the accuracy of the TDC measurement and the precision in the determination of t_{signal}. In this work, the particle's path is modeled as a 3D helix, as described in the next section.

5.1.2 Track Model

A charged particle, that propagates through the SAND tracking volume, experiences a magnetic field of 0.6 T that bends its trajectory in the zy plane, where z is the neutrino beam direction and x the direction of the magnetic field. The reconstruction of the particle track is not trivial because of the cumulative effect of the Multiple Coulomb scattering and particle energy loss. However, in the case of minimum ionizing particle as muons, one can assume the track being approximately a helix that can be parametrized as follows:

$$\begin{cases} x_h(s) = x_0 - s \cdot \sin\lambda \\ y_h(s) = y_0 + R \cdot \left[\sin\left(\Phi_0 + \dfrac{h \cdot s \cdot \cos\lambda}{R} \right) - \sin(\Phi_0) \right] \\ z_h(s) = z_0 + R \cdot \left[\cos\left(\Phi_0 + \dfrac{h \cdot s \cdot \cos\lambda}{R} \right) - \cos(\Phi_0) \right] \end{cases} \tag{5.2}$$

where:

- x_0, y_0, and z_0 are the coordinates of the helix starting point;
- λ represents the dip angle;
- Φ_0 is the initial angle between the z axis and the point (x_0, y_0, z_0);
- R is the radius of the helix.
- h is the sense of rotation.

The starting point of the helix (x_0, y_0, z_0) can be determined through geometrical considerations. Once the helix is fitted, its origin corresponds to the point where it intersects the target, marking the location of the neutrino interaction.

Given a set of n measured TDCs, the reconstructed track is the one whose parameters minimize the quantity:

$$\chi^2 = \sum_{i}^{wires} \left(\frac{r_i^{observed} - r_i^{estimated}}{\sigma} \right)^2 \tag{5.3}$$

where:

- $r_i^{observed} = (TDC - t_{tof} - t_{signal} - t_0) \cdot v_{drift}$ is the radius of the drift circle for wire i obtained from the measured TDC assuming that t_0 is known (a global clock), t_{tof} is provided by the trigger and t_{signal} can be calculated (see next section);
- $r^{estimated}$ is the minimal distance between the assumed track and the wire i; It is a function of the track parameters;

- σ is the spatial resolution associated to each wire measurement, here set to 200 μm.

The sum in Eq. 5.3 runs over all the wires fired by the track to be fitted. Note that $r^{estimated}$ would necessitate a numerical estimation of the minimal distance between the helix and the fired wire, for all the wires, which would make the algorithm less efficient when calculating it for many wires. The approach taken here simplifies the problem by projecting the helix onto two separate planes: the bending plane (zy), which is perpendicular to the magnetic field and where the projected helix forms a circle, and the xz plane, where the projection results in a sinusoidal function with a large amplitude that can be approximated by a line. The distance from the wire to either a line or a circle is then straightforward to calculate, allowing the easy determination of $r^{estimated}$ for each triggered wire, both horizontal and vertical.

5.1.3 TDC to Drift Circle Conversion

The radius $r^{observed}$ of the drift circle is fully determined once t_{tof} and t_{signal} are estimated. For a muon, for instance, the time of flight from the production point to a given wire, is estimated assuming that the particle is traveling at c and the flight length is the distance between the wires' z coordinate (ν beam direction) and that of the earliest fired wire. The signal propagation time, t_{signal}, for a given wire is calculated using the coordinates of the fired wires with opposite orientations. For example, a linear fit of the vertical wires' coordinates (z_c, x_c) provide an initial estimate of the particle's trajectory in the zx plane whose intersection with the coordinate z of a horizontal wire, provide the point x along the wire where the particle crosses and the signal originated. The procedure is illustrated in Figure 5.2 A circular fit of the horizontal fired wires provides an initial estimate of the track's parameters, and its intersection with the vertical wires gives an estimate of the y-coordinate along the vertical wires where the signal originated, thereby determining the signal time (the yellow numbers on the picture).

Fig. 5.2 shows the residuals between the true signal time t_{signal} and the one estimated with the method outlined $t_{signal}^{assumed}$ for as set of muon tracks. The signal time is reconstructed with an accuracy one order of magnitude smaller than that expected for the TDC measurement, typically few nanoseconds. Therefore, the error on the estimation of t_{signal} does not impact the track reconstruction.

5.1.4 Reconstructed Track

The fit of the fired wires coordinates gives a first guess for the track parameters. The reconstructed track is found minimizing Eq. 5.3, where the observed drift radius $r^{observed}$ is a function of both the measured TDCs and of the track parameters (via the determination of t_{signal}) . $r^{estimated}$ is also a function of the track parameters and of the coordinates of the fired wires $\vec{x}_i$:

$$\begin{aligned} r_i^{observed} &= r^{observed}(\text{pars}(\vec{x}_i),\ TDC_i) \\ r_i^{estimated} &= r^{estimated}(\text{pars}(\vec{x}_i),\ \vec{x}_i) \end{aligned} \tag{5.4}$$

The distance of the closest approach for the track model assumed in Sec. 5.1.2

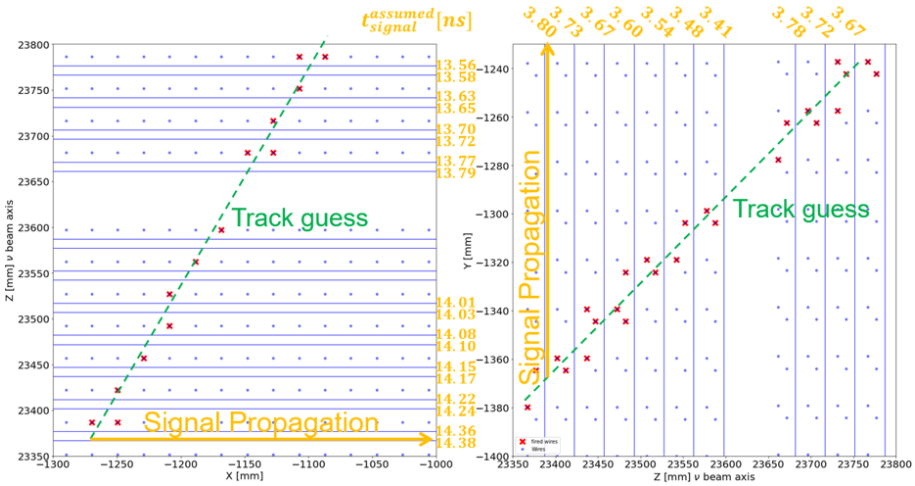

Figure 5.2: The image presents two zoomed-in views of the wires in the SAND tracker. On the left is the zx plane, aligned parallel to the magnetic field (with B oriented along the x-axis), while on the right is the zy plane perpendicular to the magnetic field, where the particle's trajectory curves. The red crosses indicate the wires fired on the opposite plane by the passing particle. Blue dots represent wires with no signal, while solid lines depict the arrangement of horizontal (on the left) and vertical (on the right) wires. The dashed green line is the linear and circular fit of the fired wires coordinates that provide an estimate of the signal propagation time (values in yellow) for the wires with opposite orientation.

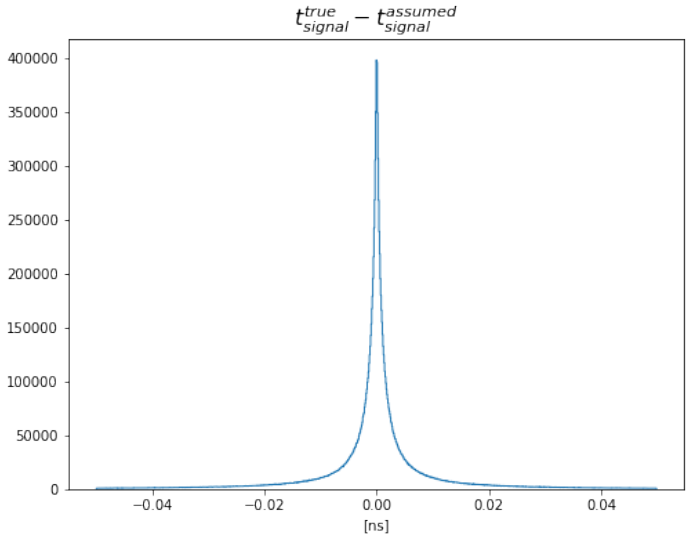

Figure 5.3: Residuals between true time of signal propagation along the wire and its assumed value.

is the distance between the fired wires coordinates and a circle in the plane perpendicular to the magnetic field:

$$r_i^{estimated}(\vec{x}_i) = |\vec{x}_c - \vec{x}_i| - R \tag{5.5}$$

where $\vec{x_c} = (x_{c,z}, x_{c,y})$ and R , the parameter to be fitted, are the center and radius of the circle. On the opposite view, the parameters to be found are the one of a line tangent to the drift circle, that is an angular coefficient $tan\lambda$ and a point x_0 . These two are linked to the parameter of the circle via:

$$\begin{cases} x = x_0 + \rho \tan\lambda \\ \rho = z\cos(\pi/2 - \Phi_0) + y\sin(\pi/2 - \Phi_0) \end{cases} \tag{5.6}$$

The total number of parameter to be fitted is then five. The χ^2 minimization process is executed using the TMinuit ROOT package, which takes as input the information from the fired wires and the parameters of the track model. Figure 5.4 illustrates the reconstruction algorithm. In the final stage of the algorithm, the track obtained from the fitted parameters can serve as a seed for a more accurate estimation of $r^{observed}$, leading to a refinement of the fitted parameters. After a couple of iterations, the values of χ^2 stabilize, and the algorithm terminates. Figure 5.5 portrays the same event as in Figure 5.2, with the addition of dashed red drift circles. The blue curves represent two perspectives of the helical trajectory constructed from the true parameters, while the yellow curves depict those derived from the fitted parameters.

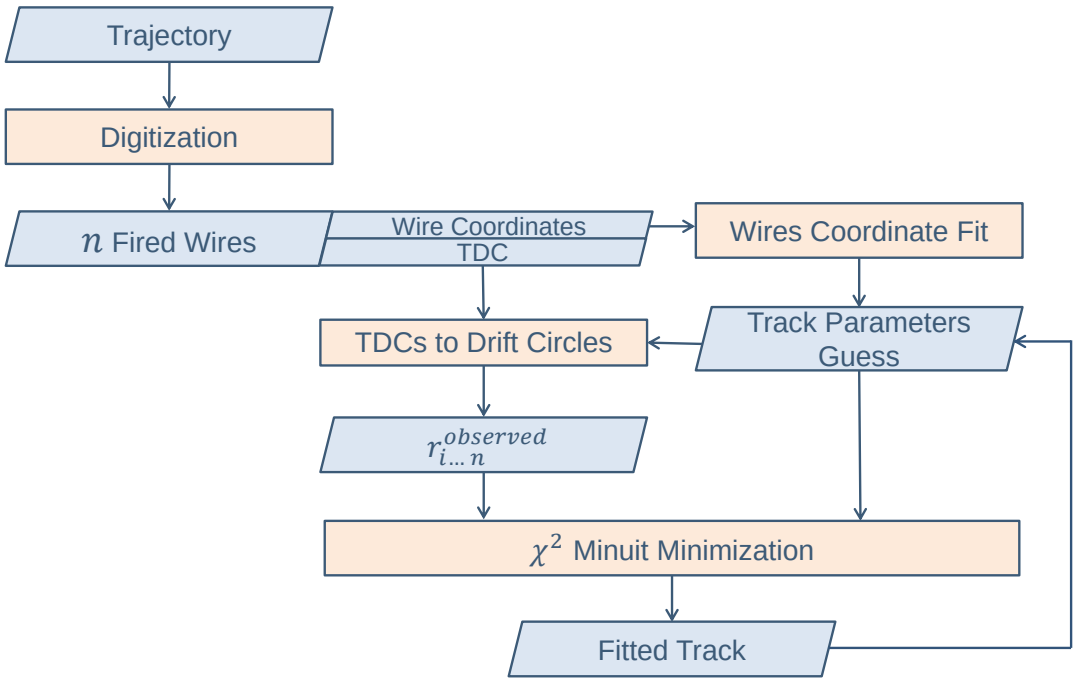

Figure 5.4: Description of the track reconstruction algorithm.

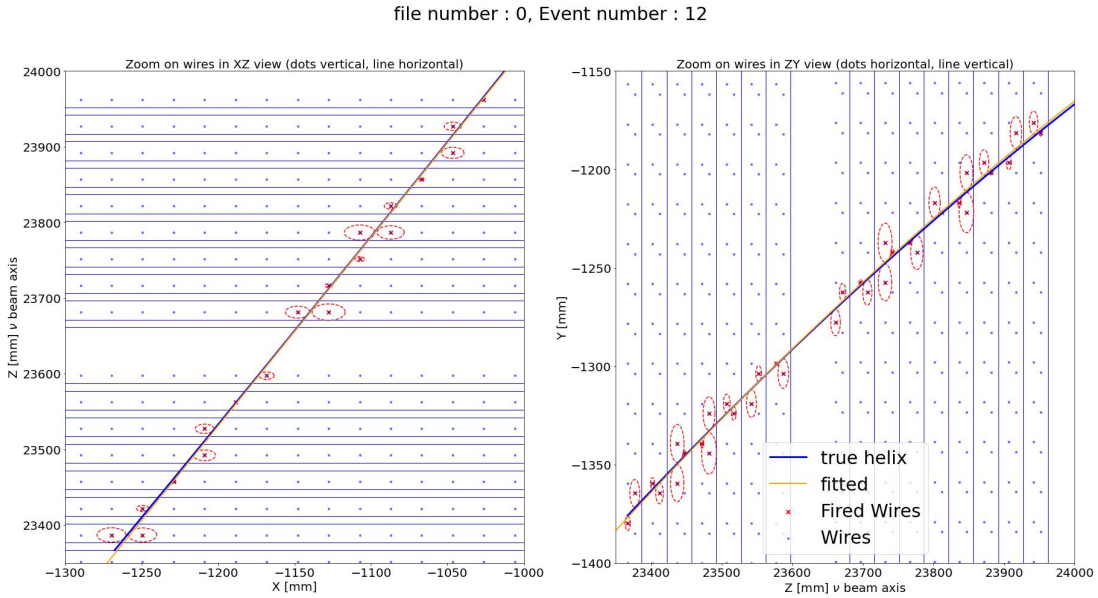

Figure 5.5: Same event represented in Fig. 5.2 where the red dashed circle depicts the drift circles found after t_{signal} estimation. The solid yellow line is the final-fitted track, which is tangent to the drift circles.

5.1.5 Reconstruction Algorithm performances

The algorithm's performance was evaluated using antimuons (μ^+) generated from neutrino charged current interactions. While the algorithm was also tested on muons, in the final chapter it will be applied specifically to the reconstruction of μ^+. Therefore, in this section, I present only the plots related to antimuons.

Neutrino CC interactions were generated using the GENIE event generator within the tracker. The final state particles were propagated using EDepSim. Energy deposition in the drift gas of the tracker was digitized in order to simulate the detector readout and obtain for each fired wire a measured TDC. For this analysis, it was assumed a pattern recognition stage that preselect digits belonging to the muon track.

The fit of the drift circles, as described above, provide the reconstructed particle trajectory. The curvature radius R of the track, obtained from the fit of the horizontal drift circles, is a direct measure of the particle momentum transverse to the B field: $p_T[GeV] = 0.3 \cdot R[m] \cdot B[T]$, whereas the single components of the momentum are found as:

$$\begin{cases} p_x = p_T \tan\lambda \\ p_y = p_T \sin(\pi/2 - \Phi_0) \\ p_z = p_T \cos(\pi/2 - \Phi_0) \end{cases} \tag{5.7}$$

The goodness of the fit and thus of the reconstruction, depends on the number of wires fired by the track. Figure 5.6 displays the χ^2 values (overall value on the left) for the fitted tracks as a function of the true muon momentum perpendicular to the magnetic field (on the right). Using a helix as track model to fit the drift circles means neglecting the effect of multiple scattering and energy loss. The less the momentum of muons, the more these two effects negatively impact the overall goodness of the fit.

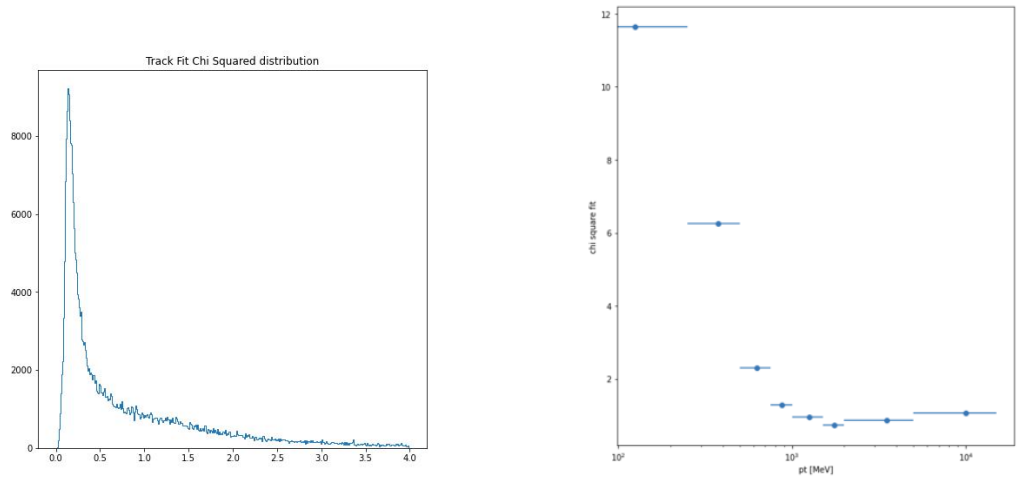

Figure 5.6: Left: distribution of the variable χ^2/n with n number of fired wires, for the fitted parameters of the reconstructed track. Right: value of χ^2/n as function of the muon momentum perpendicular to the magnetic field.

Figure 5.7 shows how the resolution on the reconstruction of p_t improves when increasing the threshold on the minimum number of fired wires necessary to perform the fit. The red curve, on the other hand, shows the percentage of excluded events

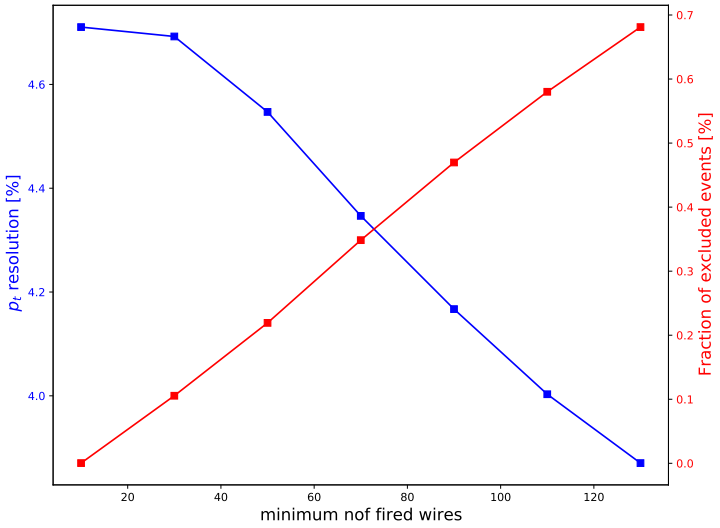

Figure 5.7: Blue curve: momentum transverse to the B field (p_t) resolution as function of the threshold on the minimum number of fired wires used to perform the fit. Red curve: fraction of excluded events from the simulated sample as function of the threshold.

when the threshold is increased. The optimal lower limit is at the intersection of the curves, which gives roughly 70 fired wires.

Figure 5.8 shows the residuals between the true and reconstructed transverse momentum as function of the true transverse momentum for the sample with no required minimum number of fired wires (on the left) and requiring at least 70 fired wires (on the right). When the fit is performed with few fired wires, it systematically gives a reconstructed momentum almost zero, which gives the events on the diagonal of the left plots. In Figure 5.9 the comparison between the true and the reconstructed momentum for the selected sample. The transverse momentum resolution was obtained as the sigma of a Gaussian distribution that fits the residuals $(1/p_{true} - 1/p_{reco})/(1/p_{reco})$. The transverse momentum resolution was evaluated to 4.3% (Figure 5.10a), whereas, the same resolution evaluated as function of the true transverse momentum, gives about 4% for 1 GeV (anti)muons (Figure 5.10b).

The fit provides the reconstructed transverse momentum and dip angle. The single components of the momentum are obtained from Equation 5.7. The comparison between the true and the reconstructed dip angle are show in Figure 5.11 and the residuals in Figure 5.12a. The resolution taken as the height at half maximum is about 4 milliradians, and the same evaluated for values of the dip angles close to zero is 2.5 milliradians (Figure 5.12b). The reconstructed momentum components are reported in Figure 5.13 and the results for the total momentum are show in Figure 5.14 and 5.15a and 5.15b.

Results are summarized in Table 5.1

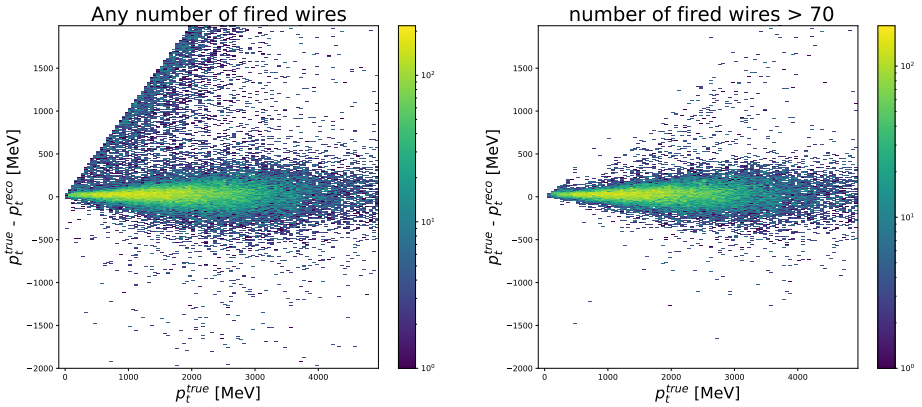

Figure 5.8: Residuals on p_t as function of the true p_t for the sample with no lower limit on the number of fired wires (left), and with a minimum number of fired wires set to 70.

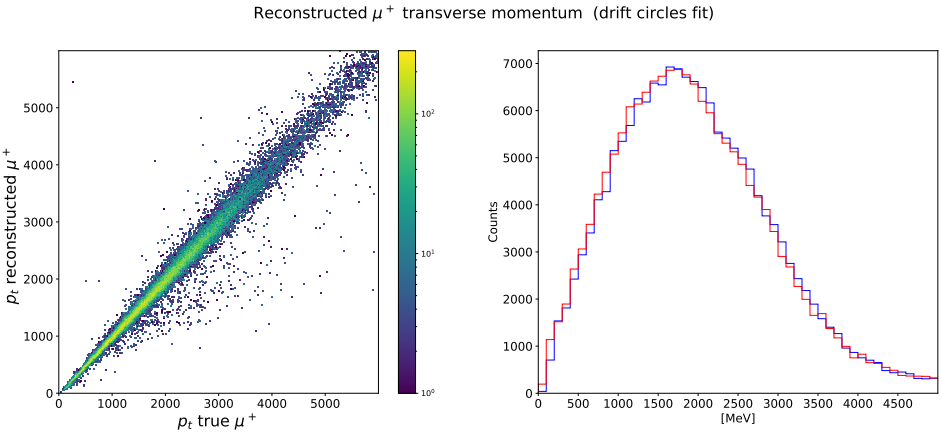

Figure 5.9: Left: true versus reconstructed transverse momentum. Right: true and reconstructed transverse momentum spectrum.

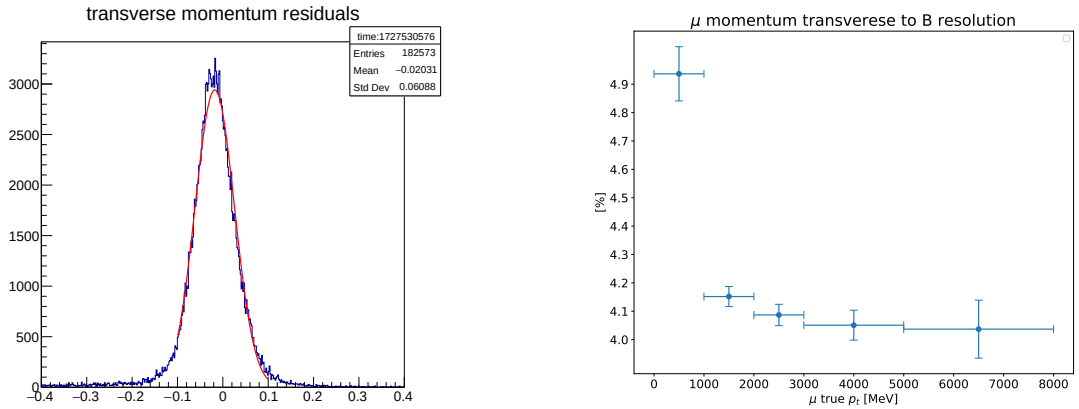

(a) (b)

Figure 5.10: Left: Distribution of the residuals $(1/p_t^{true} - 1/p_t^{reco})/(1/p_{reco})$ fitted with a Gaussian distribution. Right: transverse momentum resolution as function of the true transverse momentum.

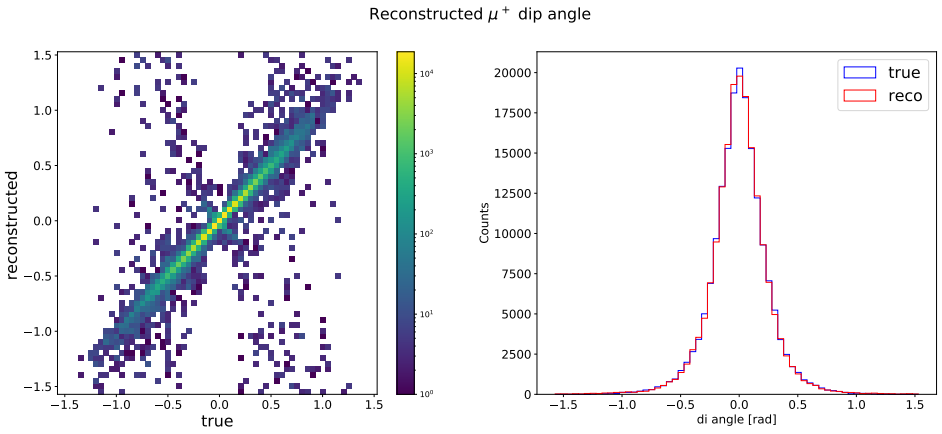

Figure 5.11: Left: true versus reconstructed dip angle. Right: true and reconstructed dip angle distributions

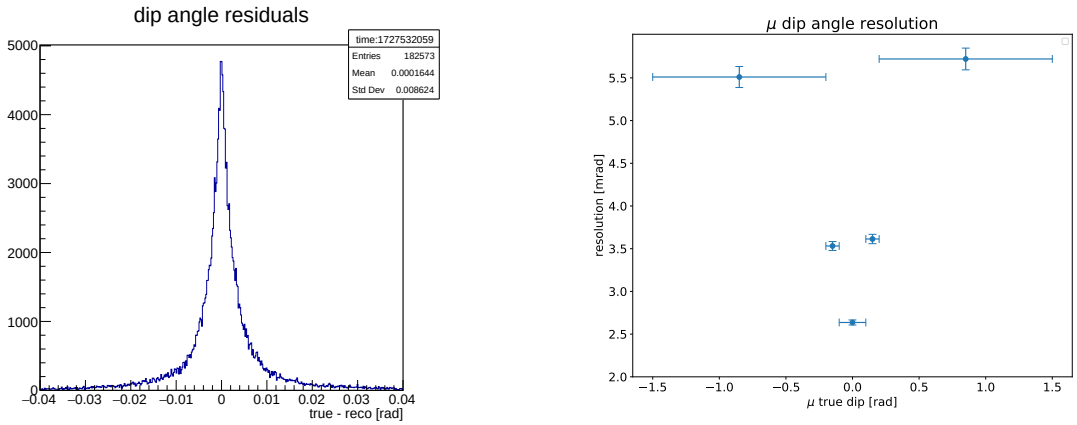

(a) (b)

Figure 5.12: Left: Distribution of the residuals $\lambda_{true} - \lambda_{reco}$. Right: dip angle resolution as function of the true dip angle.

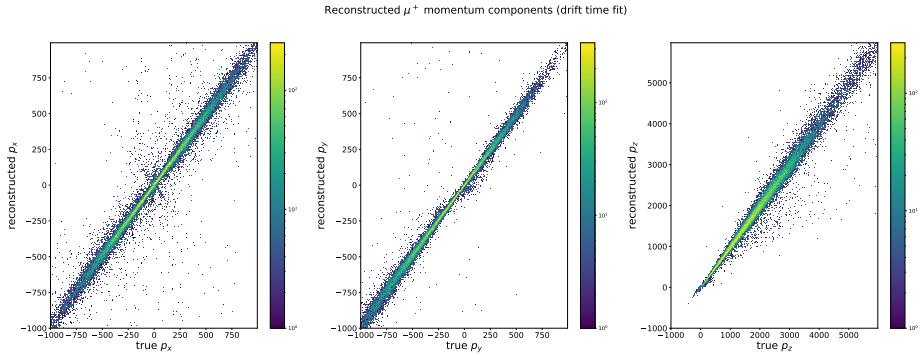

Figure 5.13: Comparison between true and reconstructed momentum components. Antimuon in the final state is boosted along z (mostly positive), being this the direction of the incoming neutrino.

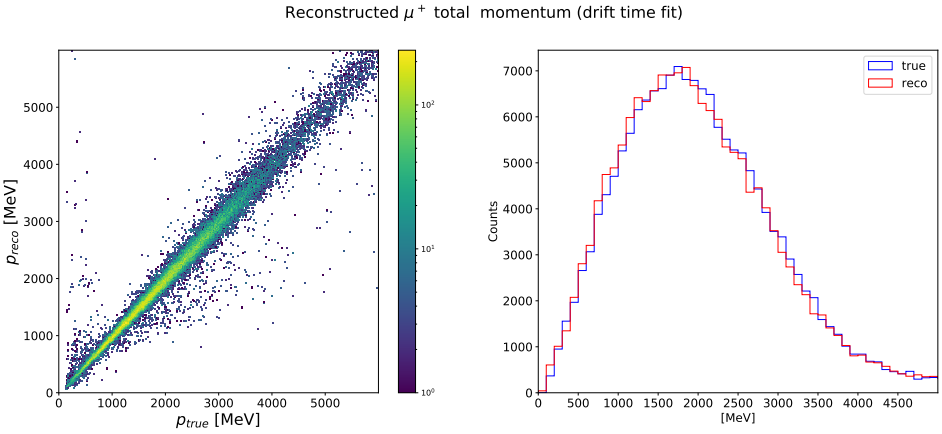

Figure 5.14: Left: True versus reconstructed total momentum. Right: True and reconstructed momentum spectra.

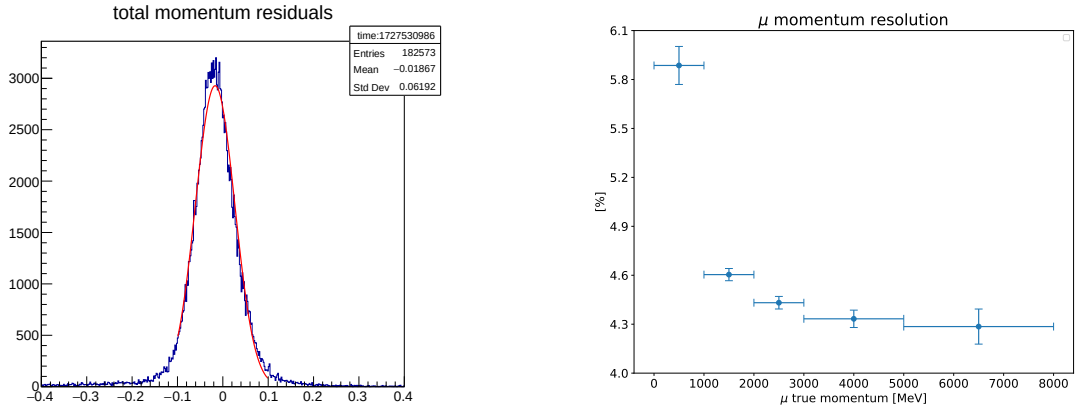

(a) (b)

Figure 5.15: Left: Distribution of the residuals $(1/p^{true} - 1/p^{reco})/(1/p^{reco})$ fitted with a Gaussian distribution. Right: total momentum resolution as function of the total true momentum.

Sample	p_t [%]	p_{tot} [%]	λ [mrad]
Any nof fired wires	5.0 ± 0.1	5.5 ± 0.2	4.0 ± 0.2
> 70 fired wires	4.3 ± 0.1	4.4 ± 0.1	3.5 ± 0.1
> 70 fired wires (2 GeV)	4.0 ± 0.1	4.1 ± 0.1	2.5 ± 0.1

Table 5.1: Transverse momentum p_t, total momentum p_{tot} and dip angle λ overall resolutions for antimuons.

5.2 ECAL clustering

As described in Section 4.3.1, the ECAL readout is segmented into 24 modules and 2440 cells each read at both ends by PMTs. The photo sensor readout provides both an amplitude signal and a time signal. Thus, for each cell, there are two amplitude signals, S^A and S^B , expressed in ADC counts and two time signals, t^A and t^B, obtained from the TDC counts using the calibration constants $c^{A,B}$ (ns/TDC counts) : $t^{A,B} = c^{A,B} \times T^{A,B}$. The constants measure by the KLOE collaborations are $c \sim 53$ ps/counts with an uncertainty of $\leq 0.3\%$ [53].

The arrival time t and the impact point s along the fiber direction are reconstructed as:

$$t = \frac{t^A + t^B}{2} - \frac{t_0^A + t_0^B}{2} - L/2v \quad [ns] \tag{5.8}$$

$$s = \frac{v}{2}\left(t^A - t^B - t_a^0 + t_b^0\right) \quad [cm] \tag{5.9}$$

where t_0^A, t_0^B are the overall time offsets, L is the cell length (cm) and v is the light velocity (cm/ns) in the fiber.

The amplitude signals on each side of the cell i is given by:

$$E_i^{A,B} = \frac{S_i^{A,B} - S_{0,i}^{A,B}}{S_{M,i}} \times k_E \quad [MeV] \tag{5.10}$$

where $S_{0,i}$ are the offsets of the amplitude scale, $S_{M.i}$ is the response in ADC counts of a minimum ionizing particle incident at the center of the calorimeter's cell and k_E is the overall energy scale factor around 40 MeV/S_M [53].

A correction factor $A_i^{A,B}$ is applied to the energy measurements taken at each side in order to take into account the attenuation along the fiber length. Eventually, the cell energy is obtained as the mean:

$$E_i = \frac{E_i^A A_i^A + E_i^B A_i^B}{2} \quad [MeV] \tag{5.11}$$

After the digitization, the algorithm starts an iterative process, beginning with cells that have hits on both sides. It forms a cluster by including adjacent hit cells around these starting cells. Cells with time differences exceeding 5 ns are separated into distinct clusters, whereas clusters that are within 40 cm and 2.5 ns of each other are merged into a unique cluster. A comprehensive explanation of the clustering algorithm can be found in [69].

5.3 GRAIN

The reconstruction of tracks in GRAIN is not trivial and is still under development. A comprehensive description of this technique can be found in [65]. The technique is based on a combinatorial approach to perform a 3D reconstruction of charged particles' track. The GRAIN volume is first segmented in voxels. The main idea is to identify a group of voxels in the 3D space compatible with the activated pixels of each sensor. The situation is illustrated in Figure 5.16. The core concept of this

technique is the maximization of the likelihood with an iterative algorithm:

$$\lambda^{k+1} j = \frac{\lambda_j^k}{\sum_s p(j,s)} \cdot \sum_s \frac{H(s) \cdot p(j,s)}{\sum_j \lambda_j^k \, p(j,s)} \quad \text{with } \lambda^{(0)} = 1 \tag{5.12}$$

where:

- k is the iteration number, s is the index for sensors and j for voxels;
- λ_j is the unknown photon emission from the voxel j,
- $p(j,s)$ express the probability of each photon to be emitted from the voxel j reaching the sensor s;
- $H(s)$ is the number of photons detected by the sensor s.

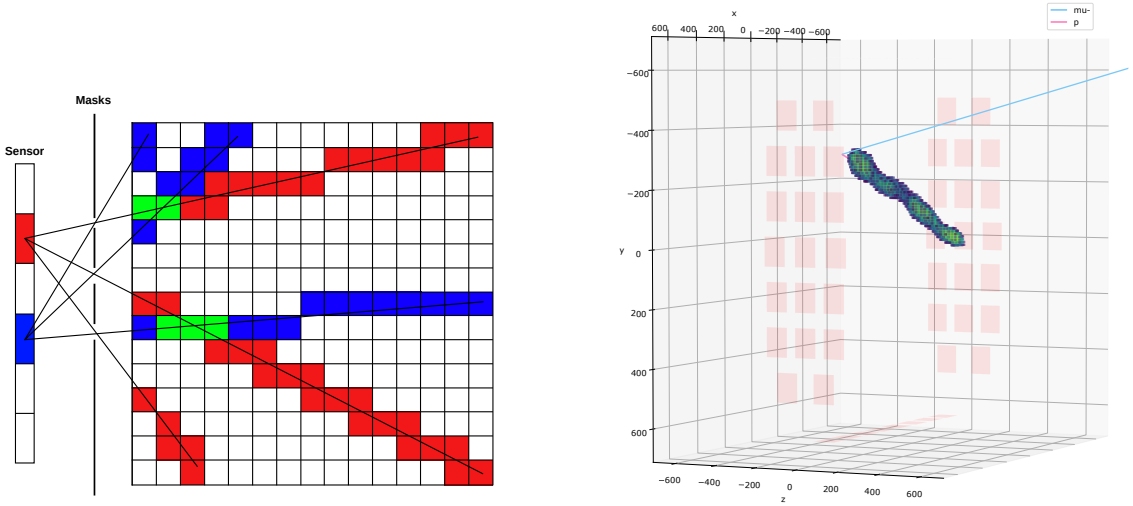

(a) (b)

Figure 5.16: Left: 2D view of the combinatorial approach to track reconstruction in GRAIN. The photons detected on each pixel of the sensor are projected in the segmented volume. The intersection of the photon's directions identifies the voxels where photons are originated (green in the picture). Right : Neutrino event with a muon and a reconstructed proton in the GRAIN volume

Chapter 6

Analysis of $\overline{\nu}_\mu + H \rightarrow \mu^+ + n$ interactions

LBNF (anti)neutrino beam with its unprecedented high intensity flux will offer the possibility to study $\nu(\overline{\nu})$-H interactions as never done before. The only available data from $\nu(\overline{\nu})$-H interactions were collected by the early bubble chamber experiments ANL [70], BNL [71], BEBC [72], and FNAL [73]. In spite of the excellent experimental resolution of those measurements, the overall statistics is limited to about 16,000 events and is insufficient for current needs.

This chapter shows SAND's ability to select a sample of antineutrino interactions on hydrogen, obtained by subtracting measurements on graphite from those on polypropylene CH_2. The channel used for this purpose is $\overline{\nu}_\mu + H \rightarrow \mu^+ + n$ (CCQE on H), where the antimuon is reconstructed in the tracker using the technique described in Section 5.1, and the neutron is reconstructed from the excellent ECAL timing resolution. The signal selection is done using a technique called "solid hydrogen" [1] in which the channel is selected exploiting only the kinematic information of the final state particles, without relying on nuclear models describing the initial state.

6.1 Kinematic Selection

The selection of $\overline{\nu}$ interactions on hydrogen is done on particle final state kinematics. Since the hydrogen target is at rest, charged current (CC) events are expected to be perfectly balanced in a plane transverse to the beam direction, with the muon and hadron vectors back-to-back in the same plane. In contrast, events from nuclear targets are affected by the energy-momentum distribution of bound nucleons (Fermi motion and binding), off-shell modifications, meson exchange currents, nuclear shadowing, and final state interactions (FSI). These nuclear effects lead to a significant missing transverse momentum and smearing of the transverse plane kinematics.

To study the signal channel, a sample of about half million antineutrino charged current events was generated in the SAND drift chamber, with final state particles propagated using edepsim. The hadron momentum vector, $\vec{p}^H$, is defined as the sum of the momentum vectors of all detectable hadrons in the final state (i.e., protons, neutrons, pions, and heavy hadrons). Excluded from this vector are hadrons absorbed in the nucleus as effect of FSI, final state leptons ($e^\pm$) and photons resulting from nuclear de-excitation. In the case of the signal channel, $\vec{p}^H$ coincides with the

momentum vector of the final state neutron. The missing transverse momentum is defined as:

$$p_T^m = |\vec{p}_T^{\,\mu} - \vec{p}_T^{\,H}| \tag{6.1}$$

where the suffix T refers to the projection of the momentum vectors onto the plane transverse to the neutrino beam direction. The situation is illustrated in Figure 6.1a where an incoming muon antineutrino interacts with a nucleus via charge current interaction producing a final state antimuon and hadrons making up the hadron momentum vector. Figure 6.1 shows the distribution of the missing transverse momentum obtained from the true momenta of the final state particles, for events occurring on H and those on CH_2. Signal events have a zero missing transverse momentum, whereas for background events, this is non-vanishing due to nuclear effects, such as nucleon's Fermi motion and final-state interactions (FSI). By reconstructing the final state particles' momenta, it is possible to use the missing transverse momentum as a powerful variable to select interactions on H.

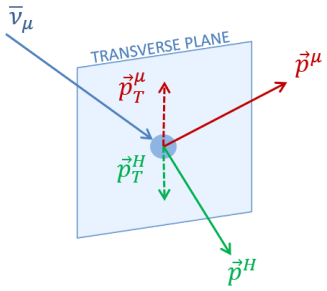

(a)

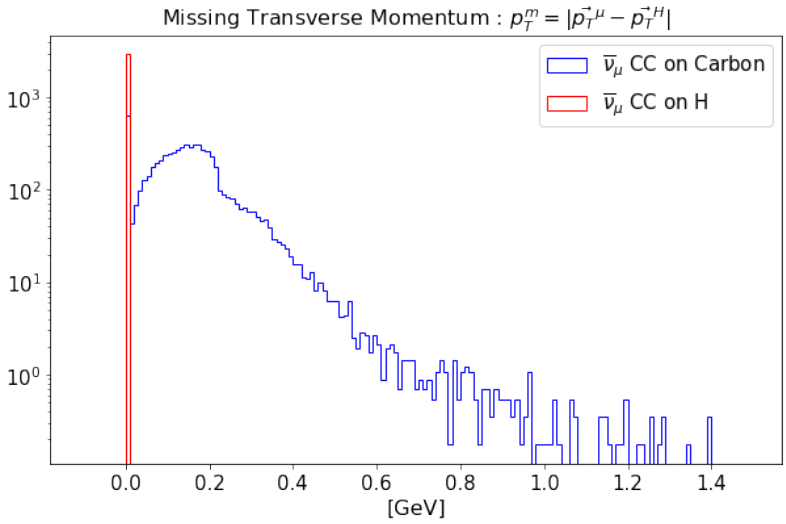

(b)

Figure 6.1: (a) Schematic representation of $\overline{\nu}_\mu$ interaction on a proton, where a μ^+ and hadrons are produced. If the interaction happens on a free proton (i.e. Hydrogen), final state particles' momenta in the plane transverse with respect to the neutrino direction are expected to be perfectly balanced. (b) Missing transverse momentum distribution for CC events on Hydrogen (red) versus CC interactions on Carbon.

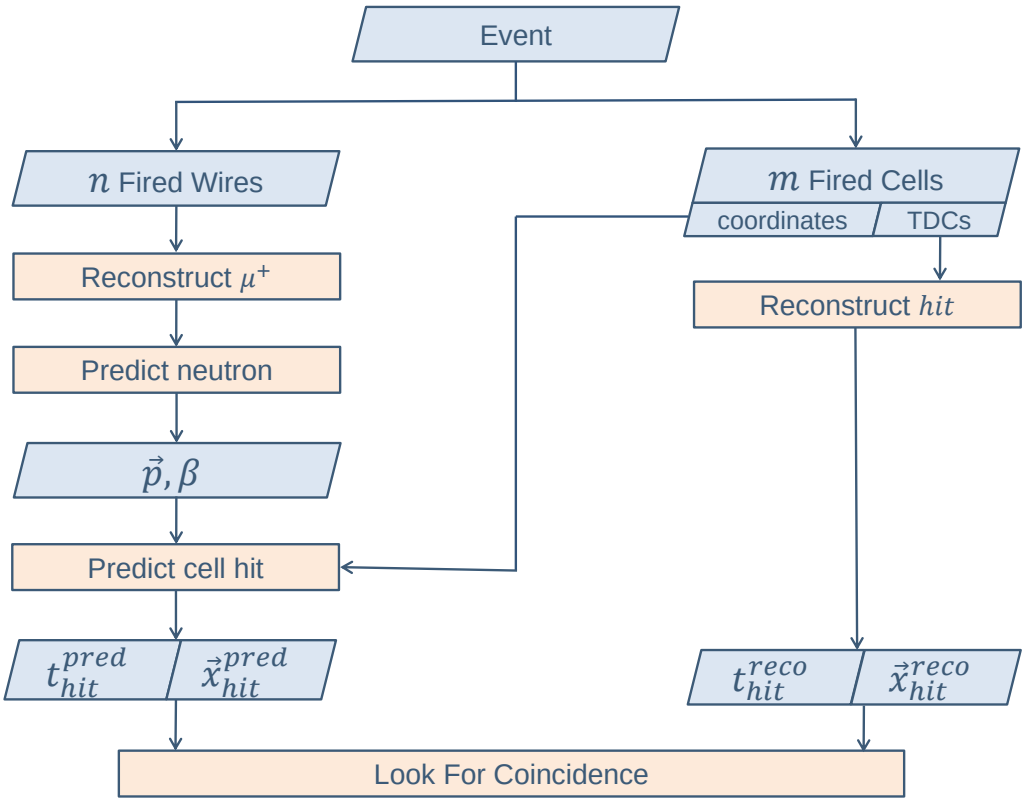

Figure 6.2: Diagram showing the steps of the analysis to select the signal.

The channel used for the selection is $\overline{\nu}_\mu + H \rightarrow \mu^+ + n$ where the antimuon's momentum is reconstructed in the drift chamber (see 5.1) and the neutron's momentum is reconstructed from its time of flight to the calorimeter from the interaction vertex. For a signal event, once the μ^+ is reconstructed, the neutron trajectory is fully determined and can be used to predict a region in the calorimeter where the neutron is expected to release energy. Moreover, this energy deposit should be compatible with the neutron's time of flight from the vertex to the calorimeter's cell. This two constrains, the position and the time of the expected hit in the calorimeter, are used to select the signal. The procedure is illustrated in the diagram 6.2, where the calorimeter's reconstructed hits are compared to the one predicted from the reconstructed muon. This will be treated more extensively in the next section.

6.2 Predictions on final state neutron

Neutrons from the signal channel are crucial for distinguishing signal events from background noise. When the direction and momentum of the antimuon are reconstructed (Sec: 5.1), the energy and direction of the neutron are fully determined. Indeed, assuming that the antineutrino interacts with a target proton at rest, its energy is:

$$E_\nu = \frac{M_n^2 - m_\mu^2 - M_p^2 + 2M_p E_\mu}{2(M_p - E_\mu + |\vec{p}_\mu| cos\theta_\mu)} \tag{6.2}$$

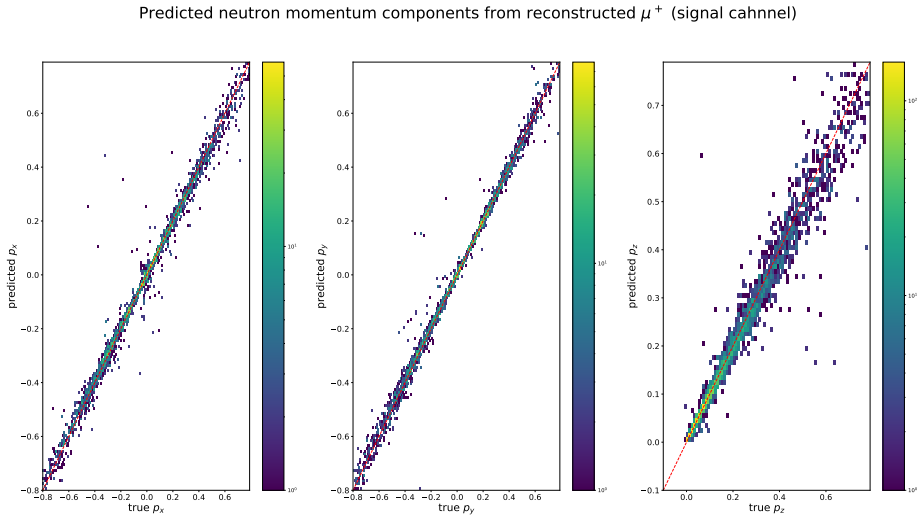

Figure 6.3: Comparison between the neutron true momentum components and the predicted from the reconstructed antimuon from signal events.

where M_p, M_n, m_μ are the masses of the proton, neutron and muon and $E_\mu, \vec{p}_\mu, \theta_\mu$ are the energy, momentum vector and angle of emission of the outgoing antimuon. The expected energy of the neutron is given by the conservation of energy, $E_n = E_\nu + M_p - E_\mu$ and its momentum vector is obtained from the momentum conservation as $\vec{p}_n = \vec{p}_\nu - \vec{p}_\mu$. Since the quantities E_n and $\vec{p}_n$ are used to predict possible fired cells in the calorimeters compatible with a neutron from signal, we shall refer to them as the predicted quantities $E_n^{predicted}$ and $\vec{p}_n^{predicted}$. When the neutron crosses the calorimeter, it may scatter off lead nuclei of the calorimeter's cells and eventually produce a TDC and ADC signal in the PMTs at the two ends of the cell. The situation is illustrated in Figure 6.6 that shows the passage of a particle through the calorimeter's cells, producing hits in a point $\vec{x}_{hit}$ at a time t_{hit}. Assuming that the neutron travels along a straight line with no interactions inside the drift chamber, the predicted point $\vec{x}_{hit}^{predicted}$ where the neutron is expected to produce a hit is calculated as the points along the neutron's line where it crosses the calorimeter's cells. The time when the hit happens is estimated as:

$$t_{hit}^{predicted} = t_0 + \frac{|\vec{x}_{hit}^{predicted} - \vec{x}_{vtx}|}{\beta c} \tag{6.3}$$

where $\vec{x}_{vtx}$ is the interaction vertex, t_0 is the interaction time and $\beta = E^{predicted}/p^{predicted}$. It is important to note that if the neutron produces a hit inside a cell interacting with some nucleus, it deviates its trajectory and the following predicted hits can substantially differ from the true ones. For this reason, the first cells fired in time are those for which the predicted hits are expected to be more accurate.
Figure 6.4 shows the comparison between the hit true quantities and those obtained from the predicted neutron for the earliest cells fired by signal neutron. The first plot compares the neutron true flight length from the interaction vertex to the hit in the cell, and the same obtained considering the predicted hit in the cell instead on the true one. The right plot compares the true time of the hit and the predicted one. The hit is predicted with a precision in the space comparable to the cell dimension ($\sim$ 5 cm) and in the time about 1 ns. In Figure 6.4 entries, very far from

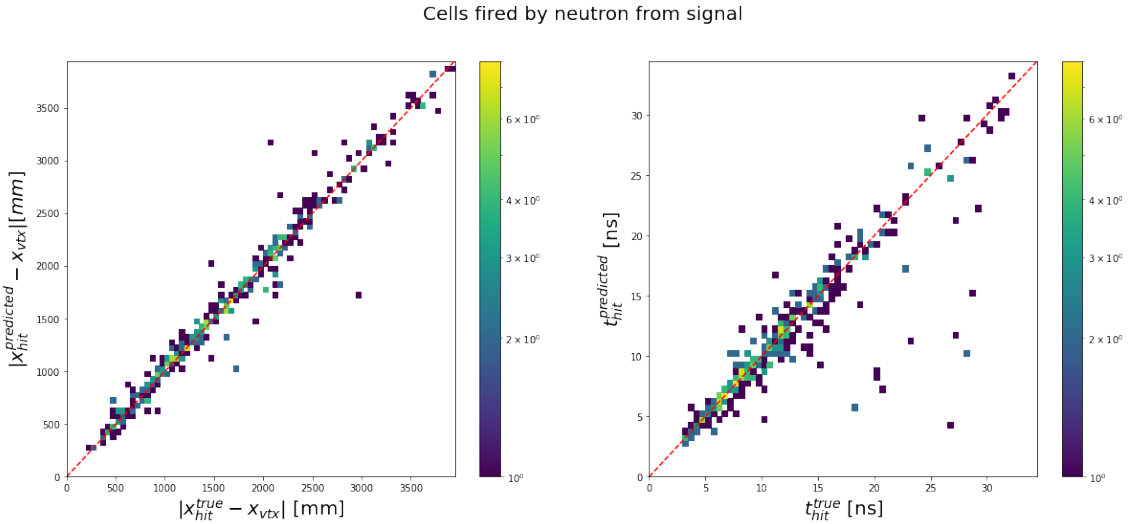

Figure 6.4: Left: comparison between the true neutron flight length from the vertex to the true hit in the cell, and the flight length calculated using the predicted neutron hit in the cell. Right: comparison between the true and the predicted neutron hit in cell.

the diagonal, are mainly given by neutrons that interact before reaching the ECAL for which the prediction cannot be valid.

6.3 ECAL Reconstruction

Signal events are selected by requiring at least one reconstructed hit in the calorimeter's cells to match the expected neutron time of flight. A coincidence between a reconstructed and a predicted hit is required within the calorimeter space and time resolutions for neutrons. These are evaluated by taking a sample of neutrons from signal events and considering the cells of the calorimeter fired by them. Figure 6.5 shows the calorimeter detection efficiency for as function of the neutron kinetic energy, calculated as the ratio between the number of neutrons that have produced two TDC signals in at least one cell of the calorimeter over the total number of simulated neutrons. For neutrons at very low energies ($\beta < 0.2$) neutrons inside the calorimeters'cells scatter several times without producing a detectable signal. The overall fraction of detected neutrons is about 65 %. For a particle that crosses a cell of the calorimeter, the time associated to the energy deposit is obtained from the measured TDCs t_1 and t_2 as:

$$t_{hit}^{reco} = (t_1 + t_2 - L_{cell}/v_{fiber})/2 \tag{6.4}$$

where v_{fiber} is the velocity of propagation of the photoelectrons along the fiber (see Section 4.3.1) and L_{cell} is the length of the cell. The coordinate along the cell where the hit is reconstructed, is given by:

$$x_{hit}^{reco} = (t_1 - t_2) \cdot v_{fiber}/2 \tag{6.5}$$

Figure 6.7 and 6.8 show the linear relation in Eq. 6.5 between the particle entry point along the cell and the difference in the measured TDCs, for neutrons and

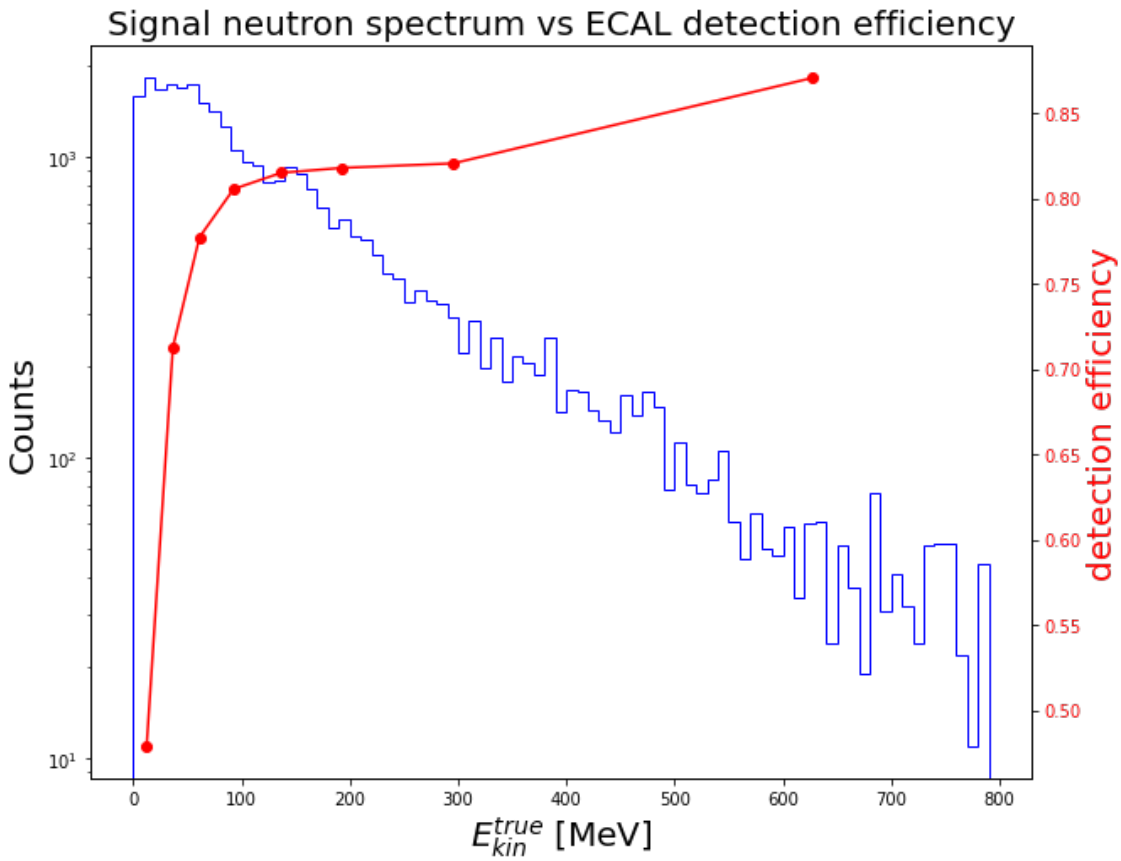

Figure 6.5: Neutron kinetic energy spectrum (blue) and ECAL detection efficiency (red).

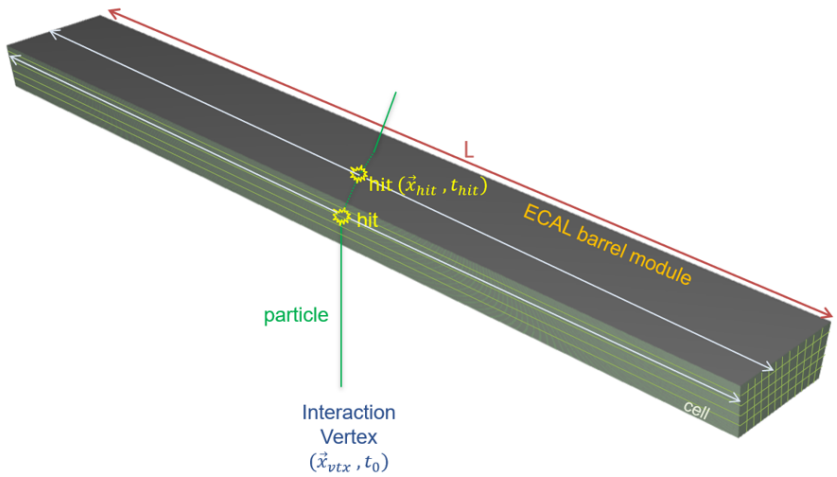

Figure 6.6: Illustration of an ECAL barrel module, showing the trajectory of a particle passing through the module and producing hits at two points, represented by $(\vec{x}_{hit}, t_{hit})$. The particle originates from the interaction vertex, denoted as $(\vec{x}_{vtx}, t_0)$. The energy released is converted in photoelectrons (white arrows) which travel to both ends of each fired cell and eventually produce a pulse in the PMTs characterized by an ADC and a TDC.

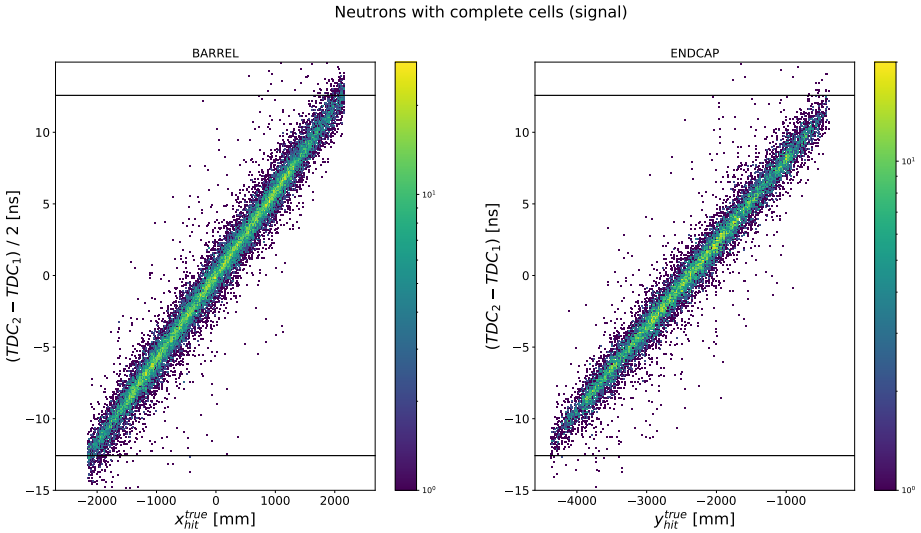

Figure 6.7: Linear relation (Eq. 6.4) between the reconstructed neutron hit coordinate along the fiber and the TDC difference. The slope is given by $2/v_{fiber}$.

μ^+ from signal. This difference is compatible with the maximum TDC difference (black horizontal lines), defined by $\pm L_{cell}/2v_{fiber}$. Figure 6.9 shows the comparison between the true and reconstructed time of the hits estimated from Equation 6.4.

The precision with which the time and space coordinate of the hit are reconstructed, depends on the energy deposition in the cell's fiber, or equivalently, on the ADC counts recorded. For a minimum ionizing particle, this is about 150 ADC counts, and for neutrons about 40. Neutrons' hits are reconstructed with a precision in the coordinate along the cell of about 15 cm and 1 ns in time, calculated the FWHM of the distributions in Figure 6.10. For μ^+ the resolutions are 6 cm and 330 ps, obtained fitting with a Gaussian distribution the distributions in Figure 6.11.

The reconstructed time of the hit provides a measure of the neutron relativistic beta factor, or equivalently, its kinetic energy. The calorimeter resolution on the neutron kinetic energy is essentially constrained by the resolution on time of the hit. Figure 6.12 shows the comparison between the time resolution obtained by considering all reconstructed hits (the same in Figure 6.10), and the resolution when only the earliest reconstructed hits are taken into account. From the reconstructed hit time, the relativistic beta factor is obtained as:

$$\beta^{reco} = \frac{|\vec{x}_{hit}^{reco} - \vec{x}_{vertex}^{reco}|}{(t_{hit}^{reco} - t_0) \cdot c} \tag{6.6}$$

where $\vec{x}_{vertex}^{reco}$ is the vertex where the neutron was originated at time t_0[1] and c is the velocity of the light. Figure 6.13 shows the residuals on the reconstructed beta of the neutron.

[1] this is taken from the Monte Carlo truth, assumed to be given by some general trigger.

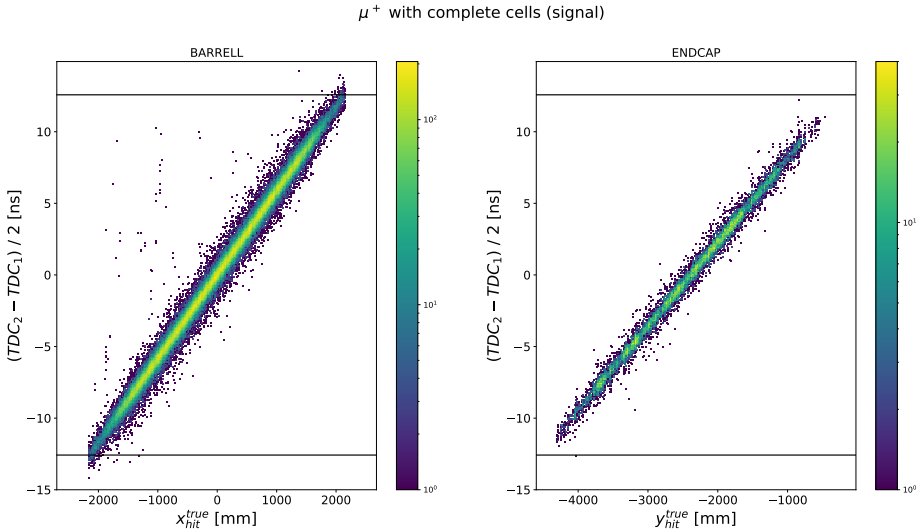

Figure 6.8: Linear relation (Eq. 6.4) between the reconstructed μ^+ hit coordinate along the fiber and the TDC difference.

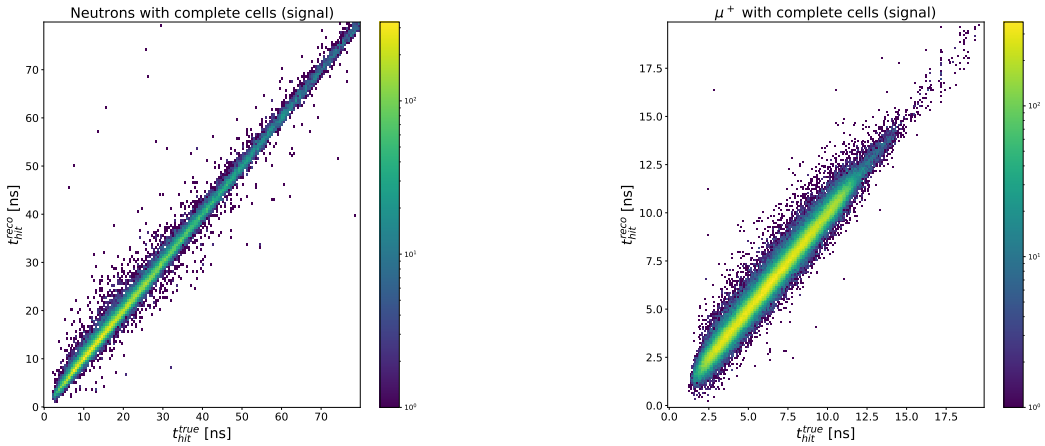

(a) (b)

Figure 6.9: Comparison between particle true hit time in the cell and the same reconstructed using the formula in Equation 6.4, for neutrons (left) and μ^+ (right) of the signal channel.

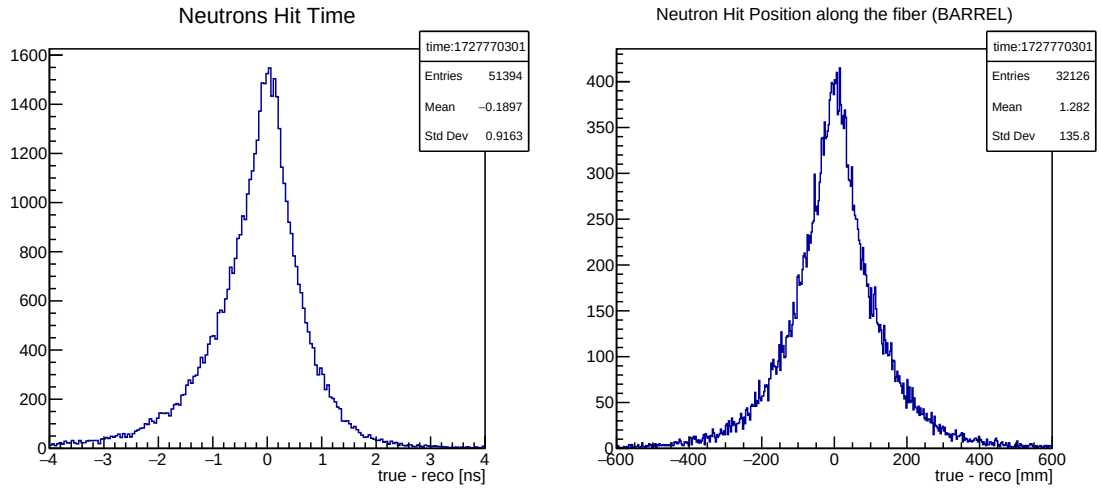

Figure 6.10: Right: distribution of the residuals $t^{hit}_{true} - t^{hit}_{reco}$. Left: distribution of the residuals $|x_{true} - x_{reco}|$ with x being the coordinate of the hit along the cell. Both plots refer to neutrons.

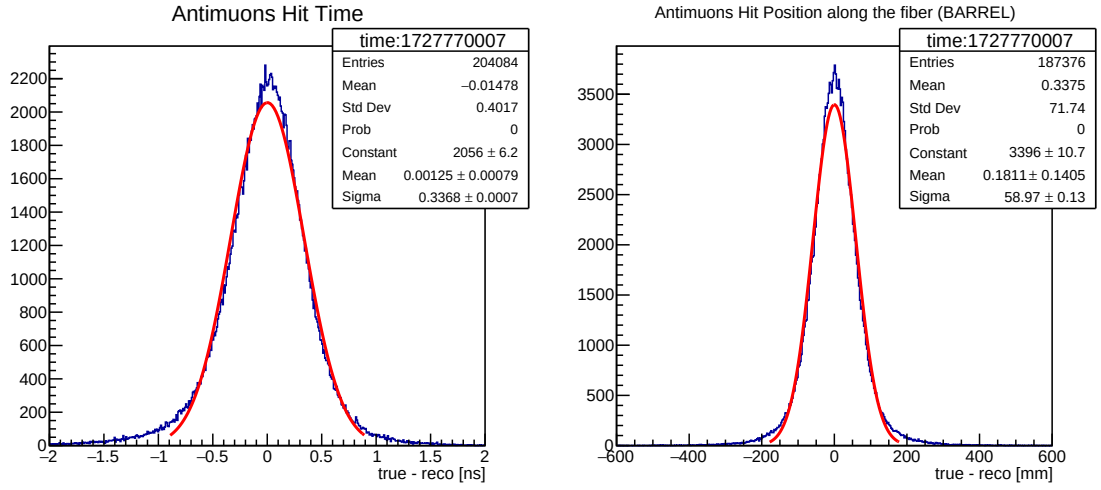

Figure 6.11: Right: distribution of the residuals $t^{hit}_{true} - t^{hit}_{reco}$. Left: distribution of the residuals $|x_{true} - x_{reco}|$ with x being the coordinate of the hit along the cell. Both plots refer to μ^+.

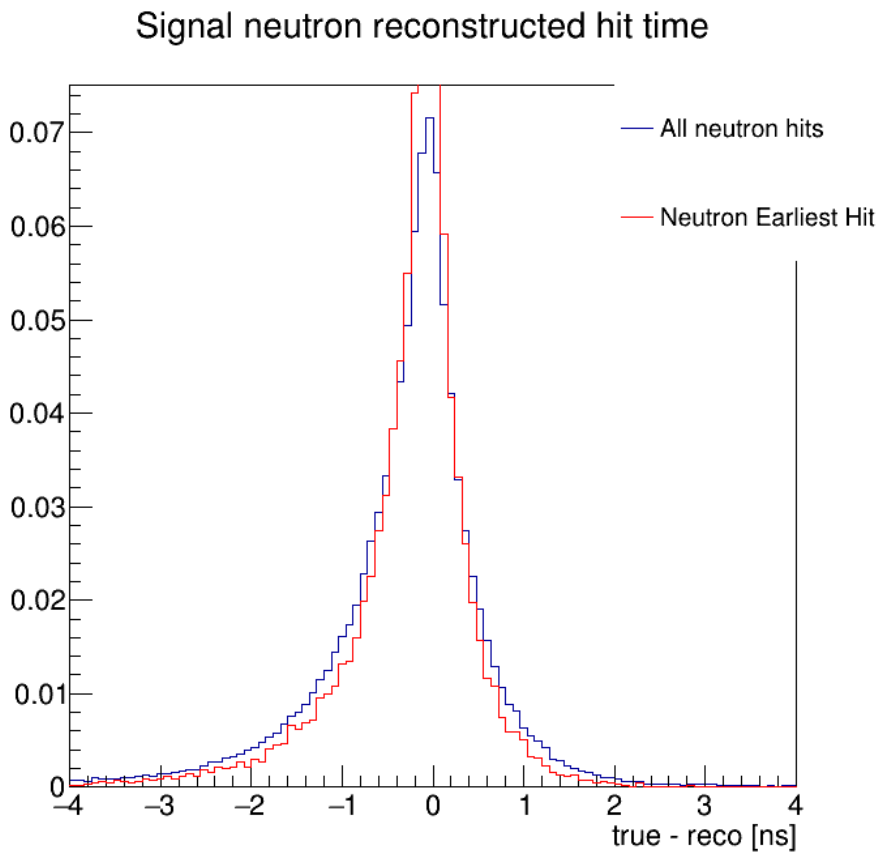

Figure 6.12: Residuals on the reconstructed neutron hit in the ECAL for all cells fired (blue) and earliest fired cells.

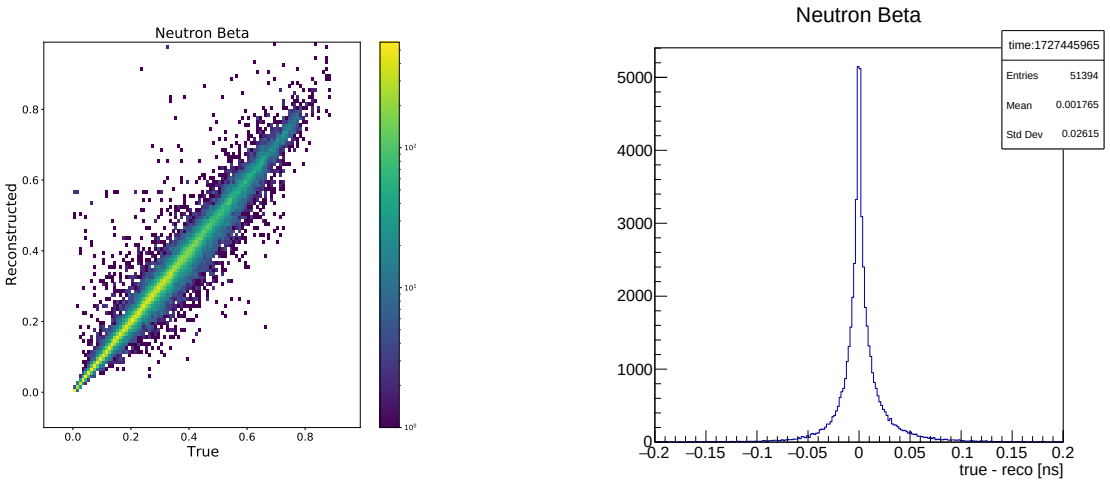

(a) (b)

Figure 6.13: Comparison between the true and the reconstructed neutron relativistic beta (left) and the distribution of the residuals (right).

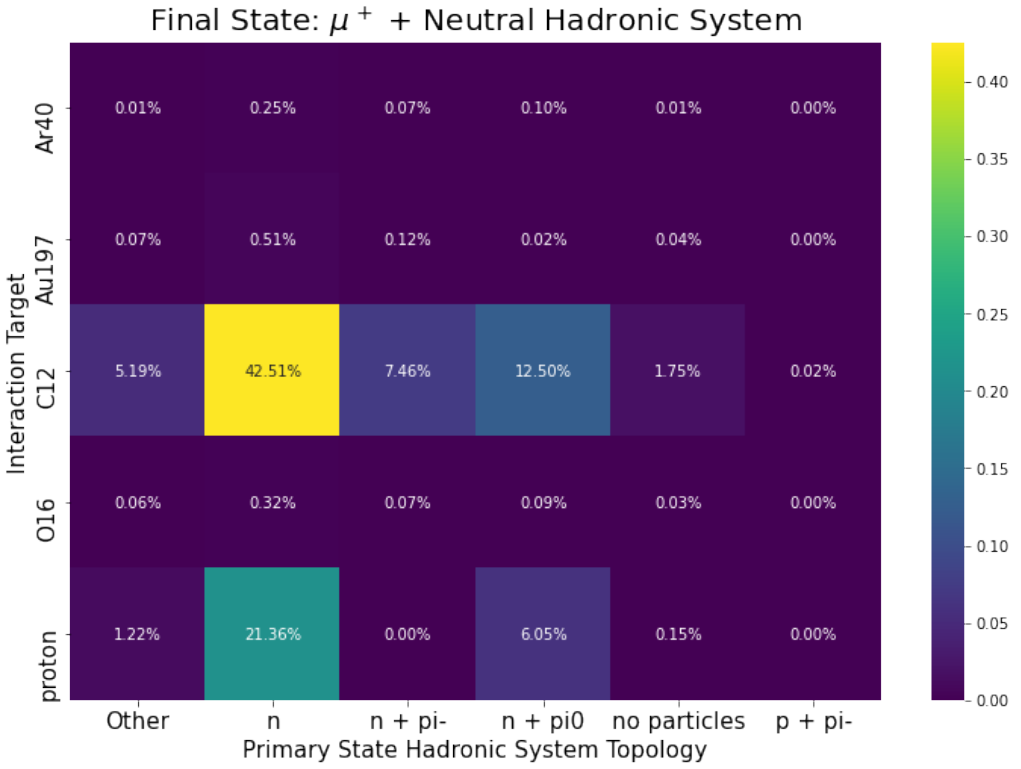

Figure 6.14: Nuclear target versus primary hadronic system (before FSI) for events with a final state topology having a μ^+ and a neutral hadron system.

6.4 Signal channel selection criteria

The signal channel is characterized by a $\overline{\nu}_\mu$ interacting with a free proton and producing in the final state an antimuon μ^+ and a neutron. Figure 6.14 shows all possible $\overline{\nu}_\mu$ CC current interactions with final state topology consisting of a μ^+ and a neutral hadronic system. On the horizontal axis, the primary hadronic system is the set of all the hadrons produced in the primary interaction of neutrino with a nucleon of the target, before any FSI occurs. Hadrons and mesons, produced with low energy in the primary neutrino interactions, can be re-absorbed within the nucleus along FSI giving rise to a single neutron in the final states. For the signal channel, primary and final hadronic coincide with the single neutron.

Background events are:

- CCQE interactions on Carbon $\overline{\nu} + p \rightarrow \mu^+ + n$;
- CCRES interactions on Carbon $\overline{\nu} + p \rightarrow \mu^+ + \Delta^-(\Delta^0) \rightarrow \mu^+ + n + \pi^-(\pi^0)$. Primary pions can be absorbed in the nucleus or, in the case of π^0 , decay in a pair of photons;
- CCRES on Hydrogen $\overline{\nu}_\mu + p \rightarrow \mu^+ + \Delta^0 \rightarrow \mu^+ + n + \pi^0$

The signal selection criteria are based on kinematic selection of the final state neutron. Indeed, as discussed earlier, interactions on free proton are characterized by a null transverse momentum. To select the signal, we require:

- a minimum number of wires to reconstruct the μ^+ track in the drift chamber;

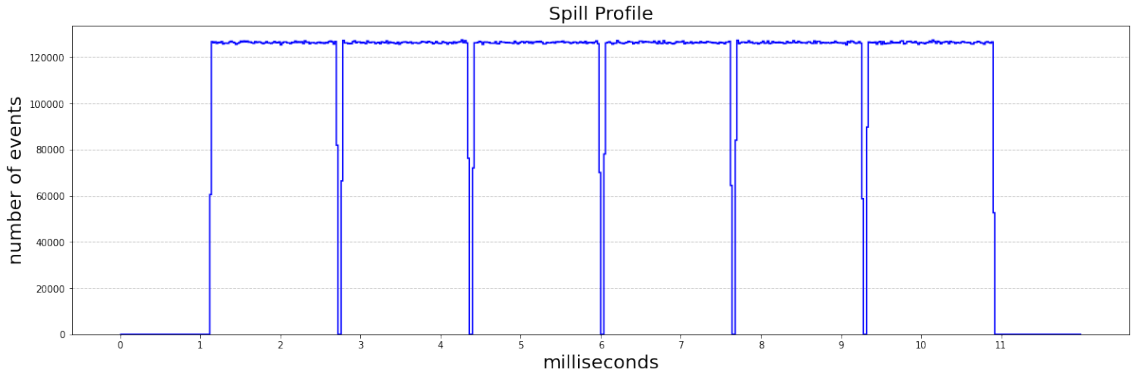

Figure 6.15: DUNE Beam spill profile.

- a single charged track reconstructed (μ^+) associated with the interaction vertex [2]

- at least one reconstructed hit in the calorimeter located within 15 cm of the neutron's predicted trajectory from the reconstructed μ^+, with a measured time of flight that matches the neutron's expected time resolution for neutrons $2.4\ ns/\sqrt{E[GeV]}$ [53], where E is the reconstructed neutron energy deposition in the cell from the measured ADCs value.

The primary background for this selection is given by $\overline{\nu}_\mu$ CCQE interactions on carbon, whose final-state neutron that can be misidentified as the neutron expected from $\overline{\nu}_\mu$ CCQE interactions on hydrogen, within the detector's resolution. However, we can estimate the contamination from this background in the selected sample by applying the same kinematic selection to the antineutrino interactions occurring on graphite targets, which consist solely of background, and then comparing them to those on C_3H_6 targets. This comparison requires an appropriate rescaling to account for the differing masses of the samples. The final H sample is therefore obtained from the difference between events from the CH_2 and graphite (C) targets. This is discussed more in extensively in Section 6.5.

6.4.1 Random neutrons from spill

An additional source of background to be considered is given by random neutrons originated from interactions in the large amount of materials surrounding the drift chamber, that is the magnet, ECAL, and yoke. In order to account for this background, a comprehensive simulation of expected timing structure of the beam spill was implemented. Each neutrino spill has a duration of 9.6 μs, a repetition cycle of 1.2 s, and an average number of 7.5×10^{13} protons on target (pot). The spill is subdivided into 6 bunches, each of them composed of 84 protons bunches at a base frequency of 53.1 MHz. Individual bunches are separated by 19ns and distributed over a time with an RMS of about 1 ns. The spill structure is shown in Figure 6.15.

For this simulation, all neutrinos flavor ($\overline{\nu}_\mu$, ν_μ, $\overline{\nu}_e$, ν_e) were simulated using reverse horn current beam mode that has an expected rate of 0.072 / ton / spill, resulting in about 44 interactions / spill. The majority of the interactions occur in

[2] The charged track vertex is localized inside a target with a precision given by the thickness of the target (few millimiters).

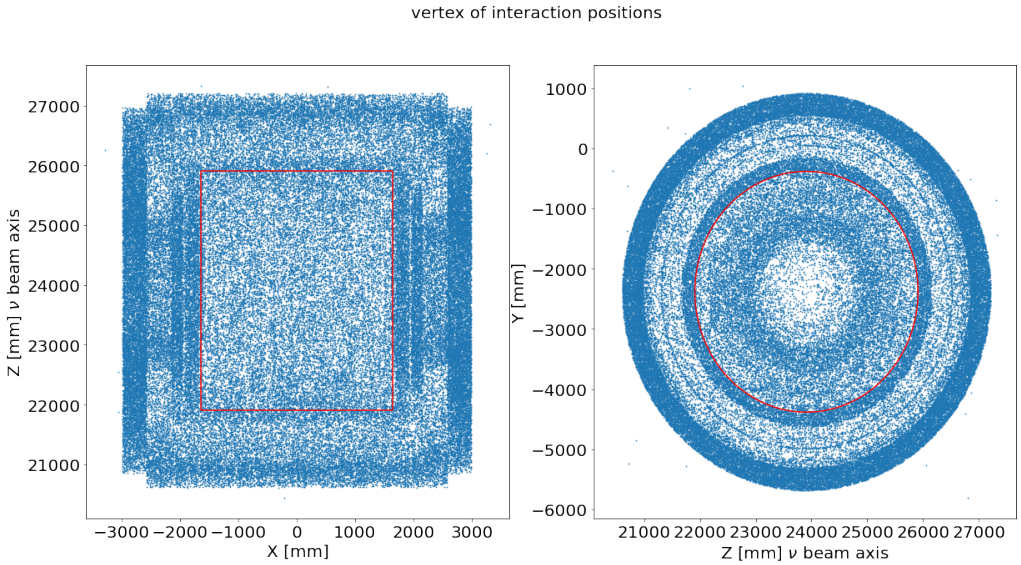

Figure 6.16: Two views of the neutrino interaction vertices in the SAND volume for multiple simulated spills. The red lines are the profile of the SAND inner tracking volume.

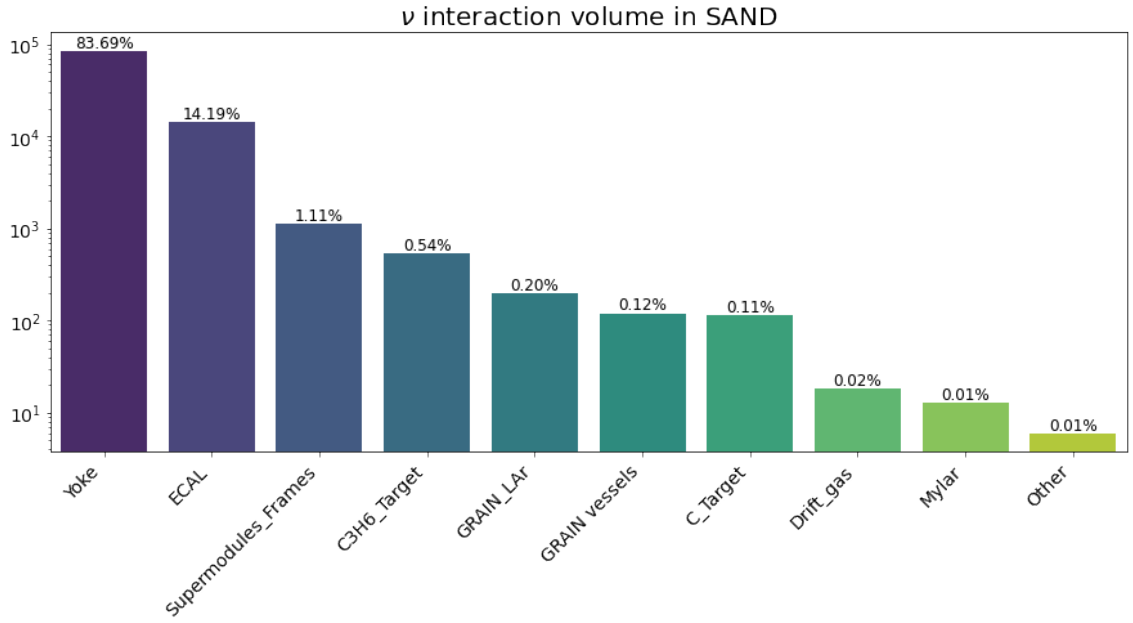

Figure 6.17: SAND components, where the (anti)neutrino interactions occur.

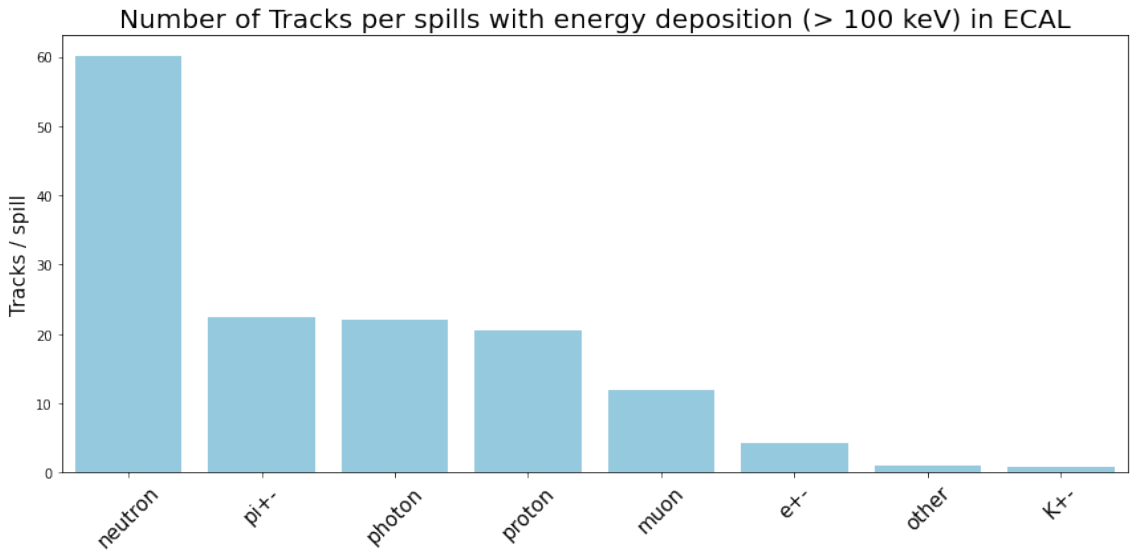

Figure 6.18: Number of tracks per spill that have some energy deposition in ECAL of at least 100 keV.

the Yoke and ECAL volumes, while less than one event per spill is expected in the tracking volume, as shown in Figure 6.17. Particles from the interactions' vertices were propagated using edepsim and energy depositions in ECAL and drift chamber were digitized and converted into ADC and TDC signals.

Figure 6.18 shows the number of tracks generated neutrino interactions, primaries and secondaries, that have some energy deposition in the ECAL. On average, there are 60 neutrons trajectories produced per spills, either from primary neutrino interactions or from elastic scattering of secondary particles with CH present in the calorimeter' fibers. On the other hand, Figure 6.19 shows the average number of cells fired by neutron tracks per spill. Among all the fired cells in a spill, we can select only those whose TDCs signals are compatible with the cell's length [3]. On average, we count about 120 cells fired per spill by random neutrons generated in the large amount of materials surroundings the tracking volume. Given the selection criteria listed in the previous section, where we look for a coincidence in a time window of 1 ns in a specific region of the calorimeter of 15 cm, we can conclude that the background induced by random neutrons (120 cells over a spill duration of 9,6 μs) is negligible.

6.5 Selection of $\overline{\nu}_\mu$ interactions on Hydrogen

To evaluate the performance of SAND in selecting antineutrino interactions in hydrogen from a kinematic selection of final-state particles, a sample of 2 million $\overline{\nu}_\mu$ CC interactions was simulated in the inner tracking volume of SAND. A minimum of 70 fired wires are required to reconstruct the final-state antimuon, which is a trade-off between the resolution of the momentum and the fraction of excluded events 5.7. The neutron time of flight is predicted from the reconstructed final-state antimuon, with its accuracy determined by the resolution of the muon's total momentum. An

[3] the sum of the TDCs has to be equal to the cell length divided by signal propagation velocity.

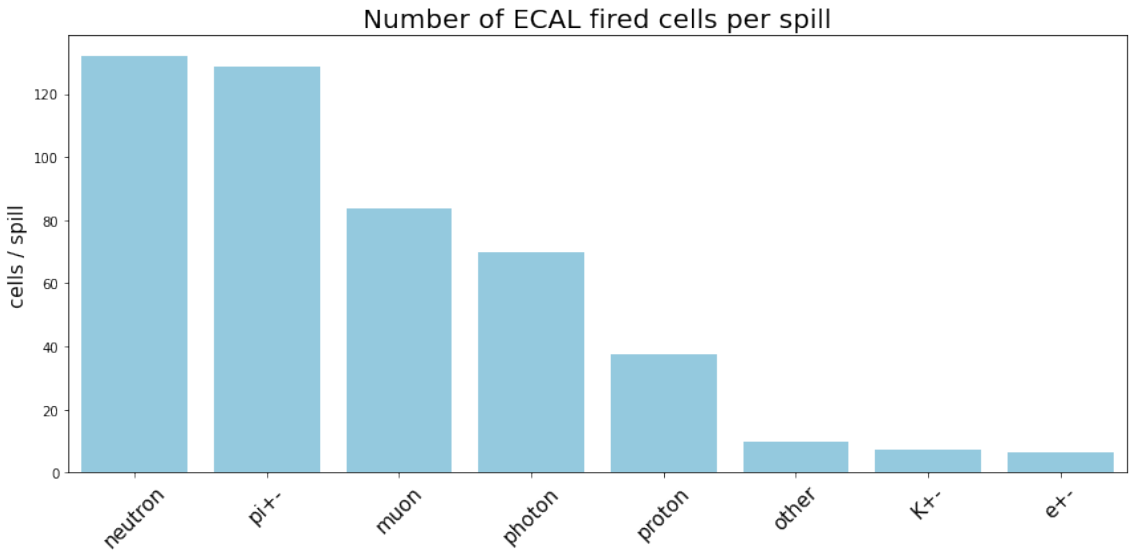

Figure 6.19: Number of cells fired per spill divided by the track type that fired them. In this plot, only cells with TDC signal on both ends are considered.

additional cut requires the charge multiplicity to be 1 (only a final state μ^+), significantly reducing any background that does not include a neutron hadronic final-state system. Eventually, the signal is selected, requiring a time and space coincidence of at least one hit in the calorimeter compatible with the signal neutron's time of flight. It has to be empathized that the following cuts:

- 70 fired wires on final state muon;
- neutron's tof to ECAL determined with precision of 55 $ps/\sqrt{E[GeV]} \times 3$ (3 σ cut);
- neutron's ECAL hit coordinate determined with precision of 5 $mm/\sqrt{E[GeV]}$ (1 σ cut);

do not represent stringent cuts to achieve the SAND requirements on the measured flux nor are optimized. The current values were evaluated in a preliminary study and showed, given the current simulated statistics, to produce better systematic uncertainties on the reconstructed neutrino flux. Future studies based on incremented statistics and better reconstruction algorithms, will refine these cuts and may adjust their thresholds as needed.

Figure 6.20 shows an example of a selected signal event, with a reconstructed $\mu+$ track and a neutron tagged in the calorimeter from its reconstructed hits. Table 6.21 summarizes the overall statistics for each selection cut in the analysis. These numbers correspond to approximately one year of data-taking, assuming a beam runtime of 10^7 s/year with one spill every 1.2 seconds. The expected statistics for the signal rate ($\vec{x}$ is the number of events per energy bin) is approximately 95k in the fiducial volume. As expected, the primary source of background rate arises from $\overline{\nu}_\mu$ CC interactions on carbon within the plastic (second row). These are predominantly CCQE interactions where the final-state neutron is indistinguishable from a signal neutron within the detector's resolution limits. A source of irreducible background is given by $\overline{\nu}_\mu$ CCQE on carbon with perfectly balanced total transverse momentum. This sets the maximum signal-to-background ratio achievable for this channel

to ∼5, essentially given by the ratio in the first bin of distributions in Figure 6.1b.

A residual background rate occurring for events originated in plastic, is given by CCRES interactions on Hydrogen with a final state π^0 (third row). This background can be excluded from the sample by reconstructing the pion invariant mass from the excellent ECAL energy resolution for photons [53]. At the moment of this writing an algorithm to reconstruct the pion in the final state is under development, and for now we can assume that this background can largely be reduced. The first three rows in Table 6.21 represent the total measured rate for events with a vertex in plastic. The corresponding reconstructed energy distribution, shown in Figure 6.22, is the sum of the three components listed above, with signal events (true CCQE on H selected) being the dominant contribution.

SAND will have the unique opportunity to measure the primary background contamination of selected signal-like events in plastic (red component in Figure 6.22) using the selected sample of CC interactions in graphite, which serves as a pure background control sample. Given the same dector acceptances for the two samples[4]it is possible to directly measure the contribution of CC interactions on carbon by using the graphite sample of events and scaling it according to the different fiducial masses of carbon in graphite and plastic. The comparison between the background rate of CC interaction on carbon of graphite and those in plastic is show in Figure 6.23. The mass ratio between the two sample has been estimated to be 4.02.

The last rows in Table 6.21 represent residual events originating from other materials in the SAND inner volume, such as Mylar, drift gas, or wires. These events can be largely excluded by requiring the absence of a fired wire in the plane preceding the location of the event's vertex.

6.6 Systematic Uncertainties on $\overline{\nu}_\mu$ Flux

Once the background rate has been measured using the control sample, it can be subtracted bin-by-bin from the reconstructed rate of selected events in plastic, as discussed in [1]. Figure 6.24 compares the reconstructed neutrino spectrum for selected true CCQE interactions on plastic with the spectrum obtained by bin-by-bin subtraction of the measured carbon background from the plastic reconstructed spectrum. This corresponds to the last row in Table 6.1. The main goal of SAND will be to measure the neutrino flux, specifically for this work, the $\overline{\nu}_\mu$ flux. The reconstructed rate obtained after subtracting the carbon background differs from the original flux due to the combined effects of the cross-section σ_S, signal selection cuts' efficiencies ϵ_S, and, ultimately, the detector response R:

$$\vec{x}^{Reco}_{plastic-graphite} \sim m_H(\Phi_{\overline{\nu}_\mu} \otimes \sigma_S \otimes \epsilon_S \otimes \ R) \tag{6.7}$$

[4]The detector acceptance is nearly identical, with only a second-order difference due to the geometric acceptance of the two samples. Although the targets are distributed uniformly across the entire tracking volume, carbon targets are always located in the most upstream region of each supermodule with respect to plastic targets.

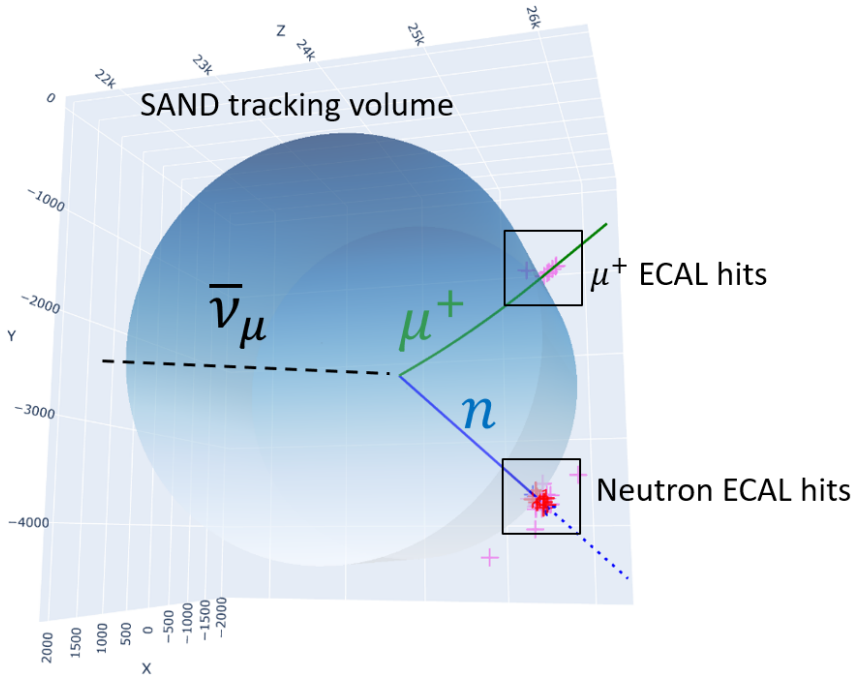

Figure 6.20: Display of a CCQE antineutrino interaction on Hydrogen with a positive muon and neutron in the final state. The green and blue lines represent the particle trajectories, whereas the pink crosses are the coordinates of the reconstructed hits in the calorimeter. The red crosses are hits whose reconstructed time and space coordinates are consistent with the expected hits from a signal neutron.

		SELECTION STEPS				
True Rate	Fiducial volume	Wires cut	Charge multiplicity	ECAL	Vertex position	Measured Rate
$\vec{x}_S^{True}$	95.578	68.877	68.877	15.696	Plastic	
$\vec{x}_{B,\,plastic}^{True}$	805.213	566.410	178.141	7.143	Plastic	$\vec{x}_{S\ like,\,plastic}^{Reco}$
$\vec{x}_{Other\ on\ H}^{True}$	203.911	154.043	47.774	1.764	Plastic	
$\vec{x}_{B,\,graphite}^{True}$	101.393	70.704	26.696	1.023	Graphite	$\vec{x}_{S\ like,\,graphite}^{Reco}$
$\vec{x}_{Others}^{True}$	51.042	35.408	8.644	467	Mylar and Gas	$\vec{x}_{S\ like,\,others}^{Reco}$

Figure 6.21: Summary of expected statistics at each selection step, assuming a beam runtime of 10^7 s/year with one spill every 1.2 seconds. Summary of expected statistics at each selection step, based on a beam runtime of 10^7 s/year with one spill every 1.2 seconds. The subscript S indicates signal events (true antineutrino CCQE interactions on hydrogen), while B represents background events. The vector $\vec{x}$ represents the event rate per unit of beam energy, with the reported numbers integrated over the entire energy distribution.

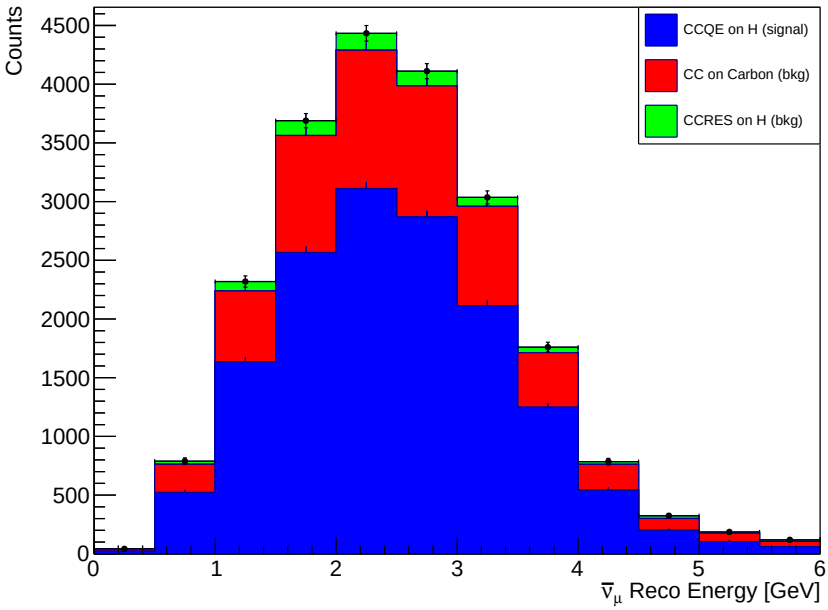

Figure 6.22: Reconstructed neutrino energy for selected event in plastic (black dots). The selected sample in plastic is mainly composed by neutrino events on Hydrogen (selected true positive) in blue and as main background neutrino CC interactions on Carbon with a single final state muon. The green component are residual background events of neutrino CCRES interactions on Hydrogen.

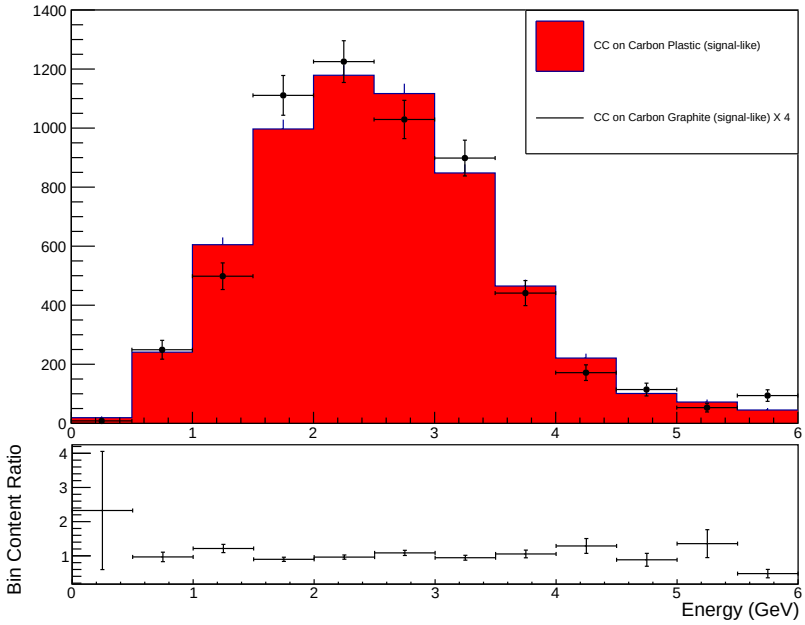

Figure 6.23: Reconstructed background rates of neutrino interactions on carbon in plastic (red) and on carbon in graphite (black dots), which represent the control sample. The two rates are consistent within the detector effects and the different total masses of carbon in plastic and graphite

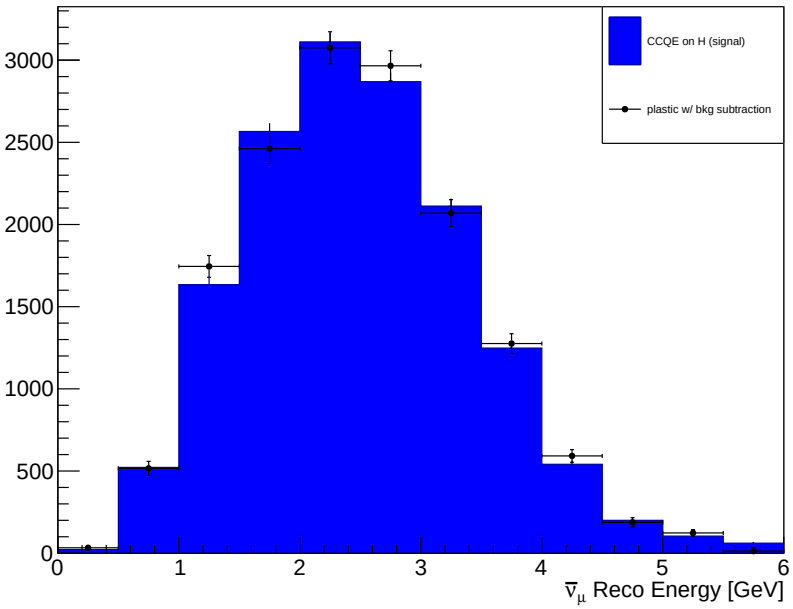

Figure 6.24: Comparison between the reconstructed energy spectrum of CCQE on H selected events (true positive) and the reconstructed spectrum obtained from a bin-to-bin subtraction of background rate measured in graphite (black dots in Figure 6.23) from the reconstructed spectrum in plastic (Figure 6.22).

where m_H is the total Hydrogen mass in the fiducial volume of SAND.

Figure 6.25 shows the distortion of the true antineutrino energy spectrum caused by the application of selection criteria to the final-state particles (effect of ϵ_S in equation 6.7), including the minimum number of wires required for μ^+ and the ECAL coincidence for the neutron. On the other hand, Figure 6.26 shows the effect of the detector response R on the neutrino energy for true CCQE on hydrogen selected events (true positives), where the reconstructed energy is obtained from the reconstructed μ^+ from Equation 6.2.

The problem of obtaining the true spectra form the convoluted effect of the detector resolution and efficiencies, can be addressed in different ways. In a real experiment, one could potentially measure the reconstruction efficiencies separately for neutrons in the calorimeter and antimuons in the drift chamber as a function of the reconstructed neutrino energy. These efficiencies could then be used to correct the measured rates for these effects. In this work, to account for detector effects, the approach is to use an *unfolding* technique implemented in the ROOT analysis framework with *RooUnfold* [74]. To perform the unfolding, the first step involves defining a response matrix that encapsulates the detector's efficiency and resolution effects. For this purpose, a object `RooUnfoldResponse` was created as:

```
1 RooUnfoldResponse response (nbins, xlo, xhi);
```

The parameters `nbins`, `xlo`, and `xhi` represent the number of bins, the lower bound and the upper bound of the energy range, respectively. The response matrix is then populated using the following logic:

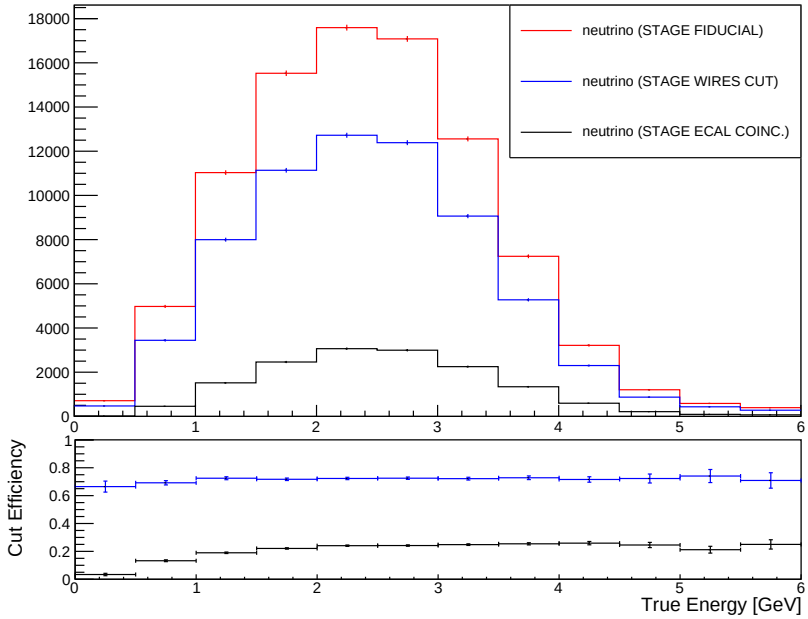

Figure 6.25: True antineutrino energy spectrum for signal events, after each cut of the analysis.

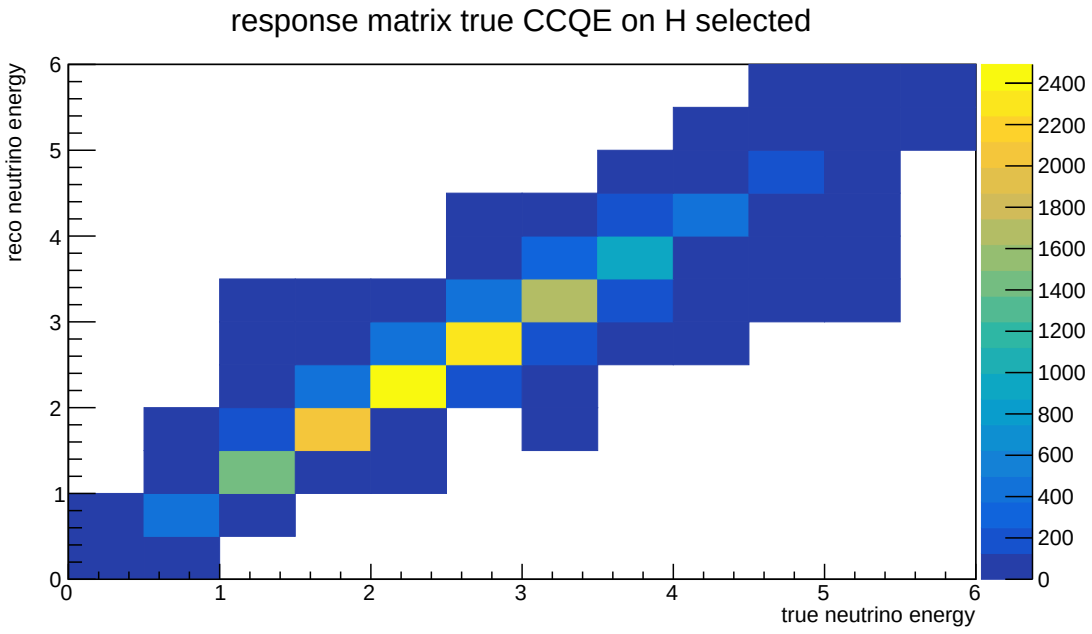

Figure 6.26: Response matrix for true CCQE on Hydrogen selected events.

```
if (is_true_signal && pass_selections) // selected true positive
    // account for detector resolution
    response.Fill(reco_neutrino_energy, true_neutrino_energy);
else
    response.Miss(true_neutrino_energy); // account for detector efficiency
```

Here, the `Fill` method updates the matrix to account for the detector's resolution by associating the reconstructed neutrino energy with the true neutrino energy. On the other hand, the `Miss` method records events where the detector fails to reconstruct the true energy, accounting for its inefficiencies. The response matrix is reported in Figure 6.26.

Once the response matrix has been constructed, the unfolding procedure is implemented using the Bayesian unfolding method. This is achieved through the `RooUnfoldBayes` class, which provides a straightforward way to perform unfolding. The process is initialized with the following code:

```
RooUnfoldBayes   unfold(response, plastic_carbon_subtracted, kterm);
```

The `RooUnfoldBayes` constructor takes three main arguments:

- `response`: The previously constructed response matrix, encapsulating the detector's resolution and efficiency.
- *plastic_carbon_subtracted*: the measured rate of selected CCQE-like events originated in plastic, from which the background contamination (e.g. interactions on carbon) has been subtracted. This represents the observed data that need to be unfolded.
- `kterm`: The regularization parameter, which determines the level of smoothing applied during the unfolding.

Figure 6.27 compares the reconstructed rate after subtraction but before unfolding (black dots, as shown in Figure 6.24), the unfolded rate, and the true signal rate (red).

As mentioned earlier, SAND offers the unique opportunity of having a rich sample of neutrino interactions on hydrogen for which the cross section is theoretically modeled by Llewelly and Smith in [75]:

$$\frac{d\sigma}{dQ^2}\left(\bar{\nu}_\mu H \to \mu^+ n\right) = \frac{M^2 G_F^2 \cos^2\theta_C}{8\pi E_\nu}\left[A(Q^2) + \frac{B(Q^2)(s-u)}{M^2} + \frac{C(Q^2)(s-u)^2}{M^2}\right] \tag{6.8}$$

where M is the nucleon mass, G_F is the Fermi constant, θ_C is the Cabibbo angle, and s and u are the Mandelstam variables. The terms A, B, and C are the vector form factors, which are functions of the electric and magnetic fields describing the charge and current distributions in the nucleon. The total uncertainties on this cross-section are below the percent level and negligible with respect to the systematic uncertainties. The cross-section in GENIE event generator can be obtained as a function of the true neutrino energy, as shown in Figure 6.28.

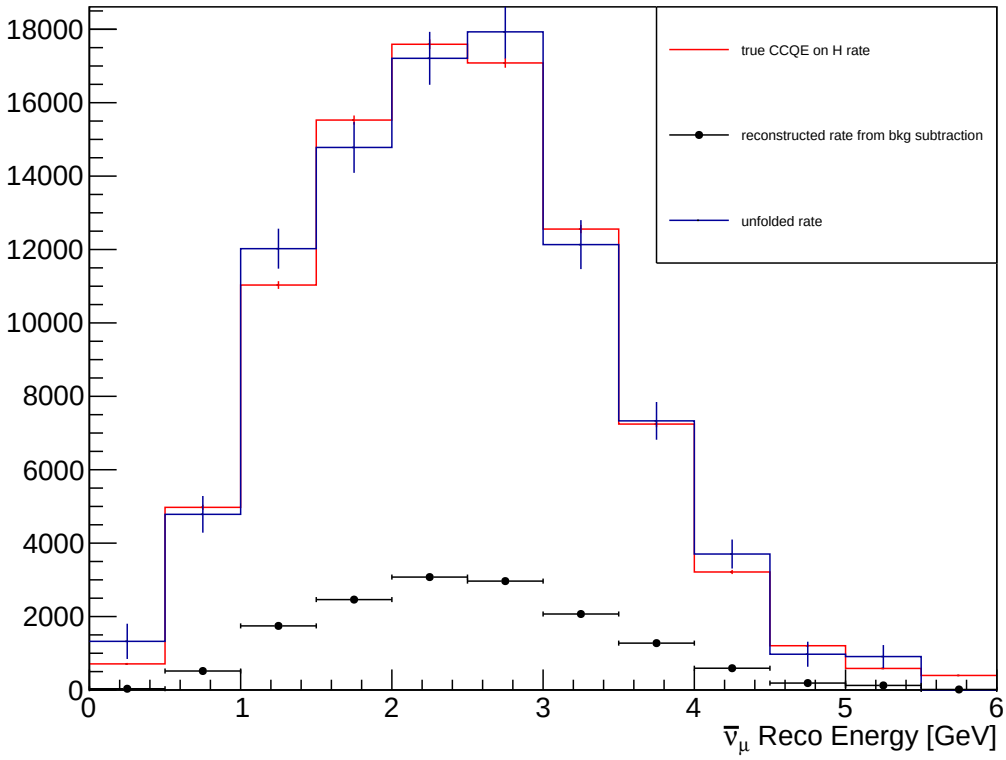

Figure 6.27: Comparison of the reconstructed rates for: *i* selected signal-like events originating in plastic targets after carbon subtraction but before unfolding (black dots, as shown in Figure 6.24); *ii* the unfolded rate (blue), and *iii* the true signal rate (red). The true signal rate is given as a function of the reconstructed energy and is the convolution of the flux, the cross-section normalized to the total mass of hydrogen in the fiducial volume.

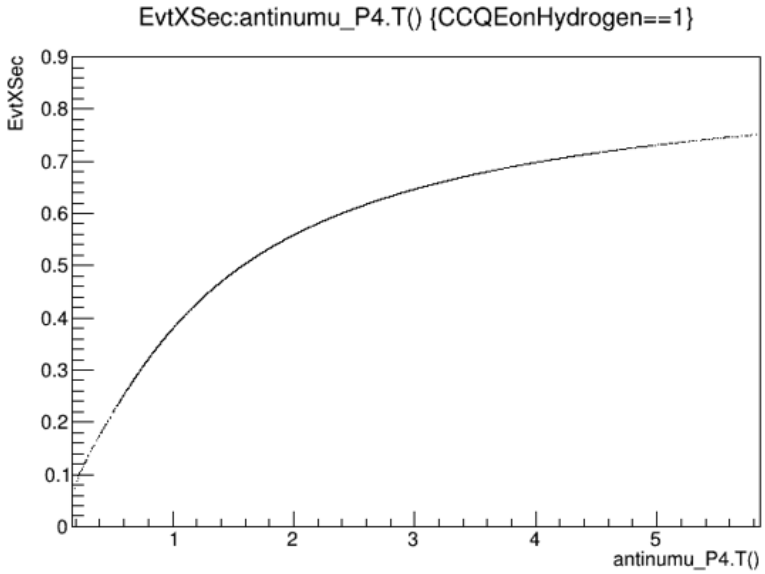

Figure 6.28: Normalized shape of $\overline{\nu}_\mu$ $H \rightarrow \mu^+$ n cross-section as function of the true neutrino Energy.

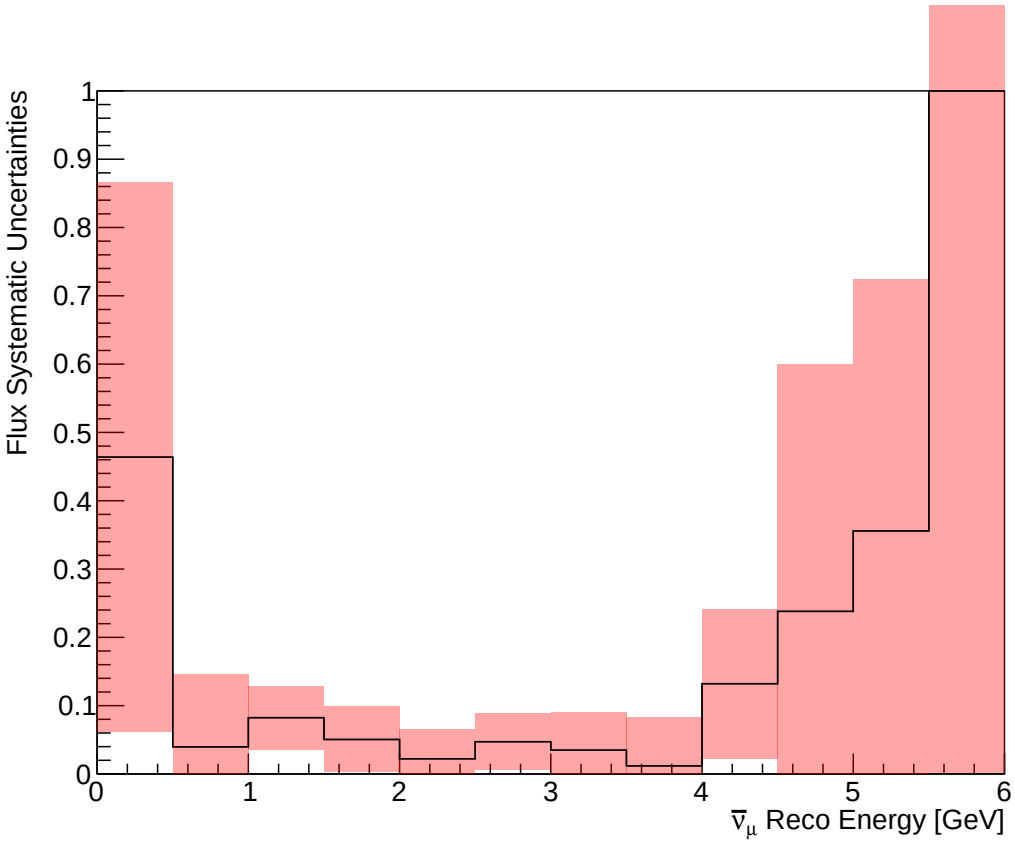

Figure 6.29: Systematic Uncertainties on the $\overline{\nu}_\mu$ flux as function of the reconstructed neutrino energy, for selected $\overline{\nu}_\mu$ $H \rightarrow \mu^+$ n interactions.

The previously defined response matrix is used to obtain the cross-section as a function of the reconstructed neutrino energy. The unfolded rate is then divided by the cross-section to obtain the reconstructed flux. Figure 6.29 shows the systematic uncertainties in the reconstructed flux $\overline{\nu}_\mu$, which accounts for the effects of the detector and the background subtraction technique.

Notation	Formula	Quantity
$\vec{x}_S^{True}$	$m_H(\Phi_{\overline{\nu}_\mu} \otimes \sigma_S)$	True signal rate for antineutrino interactions on Hydrogen: $\overline{\nu}_\mu + H \rightarrow \mu^+ + n$, where m_H is the total Hydrogen mass in the plastic target (fiducial volume).
$\vec{x}_B^{True}$	$m_C(\Phi_{\overline{\nu}_\mu} \otimes \sigma_B)$	True background rate (mainly antineutrino interactions on Carbon), where m_C is the total Carbon mass in the plastic and graphite targets (fiducial volume).
$\vec{x}_{S\text{-}like}^{Reco}$	$M(\Phi_{\overline{\nu}_\mu} \otimes \sigma \otimes \epsilon \otimes \ R)$	Reconstructed event rate for any reconstructed interaction that passes the selection criteria (signal-like), where R is the detector response and ϵ the selection efficiency.
$\vec{x}_{S\text{-}like,\ graphite}^{Reco}$	$m_C^{gra}(\Phi_{\overline{\nu}_\mu} \otimes \sigma_B \otimes \epsilon_B \otimes \ R)$	Reconstructed event rate for any reconstructed interaction that passes the selection criteria with vertex in graphite. This is a pure background control sample. Here m_C^{gra} is the total Carbon mass in the graphite targets of the fiducial volume.
$\vec{x}_{S\text{-}like,\ plastic}^{Reco}$	$m_H(\vec{x}_{S\text{-}like,H}^{Reco}) + m_C^{pla}(\vec{x}_{S\text{-}like,C}^{Reco}) + \vec{\delta}$	Reconstructed event rate for any reconstructed interaction that passes the selection criteria with vertex in plastic target. $\vec{\delta}$ is a residual background rate of CCRES on H. m_C^{pla} is the total Carbon mass in the plastic targets of the fiducial volume.
$\vec{x}_{\text{plastic - graphite}}^{Reco}$	$\vec{x}_{S\text{-}like,\ plastic}^{Reco} - \frac{m_C^{pla}}{m_C^{gra}} \cdot \vec{x}_{S\text{-}like,\ graphite}^{Reco}$	Reconstructed event rate of antineutrino interactions on Hydrogen obtained from statistical subtraction of $\overline{\nu}_\mu + C$ reconstructed rate from reconstructed rate in plastic

Table 6.1: All neutrino rates

Table 6.2: Summary of parameters for the $\overline{\nu}_\mu$ CCQE on H channel.

Parameter	**Value**
Selected channel	$\overline{\nu}_\mu\ H \rightarrow \mu^+\ n$
Exposure	$\sim 1\ yr$ (2.4 GW)
Beam runtime	1.2 $\times 10^6$ $\overline{\nu}_\mu$ CC (fiducial volume)
Selection criteria	70 hits on reconstructed μ^+, neutron's tof to ECAL determined with precision of $55\ ps/\sqrt{E[GeV]} \times 3$ (3 σ cut) neutron's ECAL hit coordinate, determined with precision of $5\ mm/\sqrt{E[GeV]}$ (1 σ cut)
Muon resolution	4.2%
Dip angle resolution	3 mrad
Flux Uncertainty	$\sim$4% (0.5–4 GeV)

Chapter 7

Future Prospects

SAND offers a unique opportunity to isolate a sample of antineutrino interactions on hydrogen by statistically subtracting graphite measurements, used as a background control sample, from interactions selected in plastic. Using the combined capabilities of the ECAL and tracker, the final-state neutron can be tagged, and the final-state antimuon reconstructed, allowing the selection of $\overline{\nu}_\mu \; H \rightarrow n \; \mu^+$ interactions within the fiducial volume.

In this analysis, the cuts applied to the number of wires for reconstructing the final-state muon are optimized to balance muon momentum resolution with the fraction of excluded events. A second selection criterion defines time and space windows in the calorimeter to identify potential signal-related neutron-induced hits in the ECAL. Preliminary investigations suggest that these criteria yield improved systematic control on the reconstructed flux.

Future improvements include:

- implementing a more accurate reconstruction algorithm for the tracker (e.g., a Kalman filter), which could modify the minimum number of wires required to reconstruct the muon (thus increasing the event acceptance);
- recovering of signal neutrons that do not produce complete cells in the calorimeter, thereby improving the overall efficiency of the signal selection (estimated to improve of about 4%);
- using an optimized clustering algorithm in the calorimeter to combine information from multiple cells, enhancing the tagging of signal neutrons and redefining the space and time windows for coincidence searches;
- integrating all selection criteria into a neural network to optimize cut values based on systematic uncertainties in the reconstructed flux;
- increasing statistics by extending the data-taking period—this analysis assumes about one year of data collection, while the nominal runtime for achieving SAND's physics goals is approximately five years.

Conclusions

DUNE will be the next generation of neutrino oscillation experiment with exploiting unprecedented beam power that will allow studying neutrino oscillation physics with high statistics. The SAND detector, as part of the Near Detector Complex, will measure the neutrino flux, its composition and stability and constrain the systematic uncertainties affecting the oscillation analysis. SAND includes a 0.6 T superconductive magnet, an electromagnetic calorimeter, a 1 ton liquid Argon active target (GRAIN) and a modular, low-density target tracker system to allow momentum resolution of the final state particles accurate to the percent level.

A key feature of SAND is that the availability of a large hydrogen target sample. This is obtained distributing thin polypropylene (C_3H_6) targets alternated to graphite targets (pure C) such that neutrino hydrogen interactions can be obtained from subtractions of measurements on graphite from those on polypropylene. One of the main limitations in measuring neutrino fluxes is the large statistical uncertainties affecting cross-section models and final-state interactions for neutrinos interacting with heavy nuclei. Neutrino interactions on hydrogen, however, are free from nuclear smearing effects, allowing the selection of interaction samples based on the kinematics of the final-state particles.

To probe the feasibility of the subtraction technique, a comprehensive simulation was implemented and includes: (*i*) detailed simulation of the SAND geometry, (*ii*) simulation of neutrino interactions and propagation of final state particles inside the detector, (*iii*) realistic detector response, (*iv*) reconstruction algorithm for the SAND tracker based on track fitting method of the measured *drift circles*. To select antineutrino interactions on hydrogen, the track reconstruction algorithm was applied to reconstruct the final state μ^+ from $\overline{\nu}_\mu + H \rightarrow \mu^+ + n$ interaction channel. The final-state neutron is identified in the calorimeter, where its energy is reconstructed based on the measured time of flight, utilizing the calorimeter's excellent timing resolution. This analysis demonstrates SAND's capability to select a pure sample of neutrino interactions by statistically subtracting CCQE-like interactions on graphite from those on plastic. A unique opportunity for SAND lies in its ability to measure the background contamination of the selected signal-like sample using a control sample with nearly the same detector acceptance as the signal region. This enables a bin-by-bin subtraction of the carbon background from the selected sample of signal-like events on plastic.

Using an unfolding procedure, the reconstructed rate is corrected for detector efficiency and resolution. Given that the cross-section of antineutrino interactions on hydrogen is known to a percent-level precision, this allows an estimation of the incident neutrino flux. The estimated statistical uncertainty on the reconstructed

flux is about 4% in the bulk of the neutrino energy spectrum.

Bibliography

[1] H. Duyang et al. *A Novel Approach to Neutrino-Hydrogen Measurements*. 2019. arXiv: 1809.08752 [hep-ph].

[2] Fermi E. "Tentativo di una Teoria Dei Raggi β". In: *Nuovo Com 11, 1-19* (1934).

[3] K.S. Hirata et al. "Experimental study of the atmospheric neutrino flux". In: *Physics Letters B* 205.2 (1988), pp. 416–420. ISSN: 0370-2693. DOI: https://doi.org/10.1016/0370-2693(88)91690-5.

[4] M. H. Ahn et al. "Measurement of neutrino oscillation by the K2K experiment". In: *Physical Review D* 74.7 (Oct. 2006). ISSN: 1550-2368. DOI: 10.1103/physrevd.74.072003. URL: http://dx.doi.org/10.1103/PhysRevD.74.072003.

[5] M. Aker et al. "Direct neutrino-mass measurement with sub-electronvolt sensitivity". In: *Nature Phys.* 18.2 (2022), pp. 160–166. DOI: 10.1038/s41567-021-01463-1. arXiv: 2105.08533 [hep-ex].

[6] N. Aghanim et al. "Planck2018 results: VI. Cosmological parameters". In: *Astronomy; Astrophysics* 641 (2020), A6. ISSN: 1432-0746. DOI: 10.1051/0004-6361/201833910. URL: http://dx.doi.org/10.1051/0004-6361/201833910.

[7] Carlo Giunti and Chung Wook Kim. *Fundamentals of Neutrino Physics and Astrophysics*. Oxford: Oxford University Press, 2007, pp. 259–269. URL: http://theor.jinr.ru/~vnaumov/Eng/JINR_Lectures/books/Giunti2007.pdf.

[8] C. Jarlskog. "A basis independent formulation of the connection between quark mass matrices, CP violation and experiment". In: *Zeitschrift für Physik C - Particles and Fields* 29 (1985), pp. 491–497. DOI: 10.1007/BF01565198.

[9] Mattias Blennow and Alexei Yu. Smirnov. "Neutrino Propagation in Matter". In: *Advances in High Energy Physics* 2013 (Mar. 2013), p. 972485. ISSN: 1687-7357. DOI: 10.1155/2013/972485.

[10] A. Cervera et al. "Golden Measurements at a Neutrino Factory". In: *Nuclear Physics B* 579.1 (2000), pp. 17–55. ISSN: 0550-3213. DOI: 10.1016/S0550-3213(00)00221-2.

[11] A. Cervera et al. "Erratum to "Golden Measurements at a Neutrino Factory": [Nucl. Phys. B 579 (2000) 17]". In: *Nuclear Physics B* 593.3 (2001), pp. 731–732. ISSN: 0550-3213. DOI: 10.1016/S0550-3213(00)00606-4.

[12] W. Hampel et al. "GALLEX solar neutrino observations: Results for GALLEX IV". In: *Phys. Lett. B* 447 (1999), pp. 127–133. DOI: 10.1016/S0370-2693(98)01579-2.

[13] M. Altmann et al. "Complete results for five years of GNO solar neutrino observations". In: *Physics Letters B* 616.3 (2005), pp. 174–190. ISSN: 0370-2693. DOI: https://doi.org/10.1016/j.physletb.2005.04.068.

[14] J. N. Abdurashitov et al. "Measurement of the solar neutrino capture rate with gallium metal. III. Results for the 2002–2007 data-taking period". In: *Phys. Rev. C* 80 (1 July 2009), p. 015807. DOI: 10.1103/PhysRevC.80.015807.

[15] W.C. Haxton, R.G. Hamish Robertson, and Aldo M. Serenelli. "Solar Neutrinos: Status and Prospects". In: *Annual Review of Astronomy and Astrophysics* 51.1 (2013), pp. 21–61. DOI: 10.1146/annurev-astro-081811-125539.

[16] K.S. Hirata et al. "Experimental study of the atmospheric neutrino flux". In: *Physics Letters B* 205.2 (1988), pp. 416–420. ISSN: 0370-2693. DOI: https://doi.org/10.1016/0370-2693(88)91690-5.

[17] K. Abe et al. "Solar neutrino measurements in Super-Kamiokande-IV". In: *Phys. Rev. D* 94 (5 Sept. 2016), p. 052010. DOI: 10.1103/PhysRevD.94.052010.

[18] B. Aharmim et al. "Combined analysis of all three phases of solar neutrino data from the Sudbury Neutrino Observatory". In: *Phys. Rev. C* 88 (2 Aug. 2013), p. 025501. DOI: 10.1103/PhysRevC.88.025501.

[19] J Boger et al. "The Sudbury Neutrino Observatory". In: *Nuclear Instruments and Methods in Physics Research Section A: Accelerators, Spectrometers, Detectors and Associated Equipment* 449.1 (2000), pp. 172–207. ISSN: 0168-9002. DOI: https://doi.org/10.1016/S0168-9002(99)01469-2.

[20] G. Alimonti et al. "The Borexino detector at the Laboratori Nazionali del Gran Sasso". In: *Nucl. Instrum. Meth. A* 600 (2009), pp. 568–593. DOI: 10.1016/j.nima.2008.11.076. arXiv: 0806.2400 [physics.ins-det].

[21] K. Eguchi et al. "First results from KamLAND: Evidence for reactor antineutrino disappearance". In: *Phys. Rev. Lett.* 90 (2003), p. 021802. DOI: 10.1103/PhysRevLett.90.021802. arXiv: hep-ex/0212021.

[22] A. Gando et al. "Reactor on-off antineutrino measurement with KamLAND". In: *Phys. Rev. D* 88 (3 Aug. 2013), p. 033001. DOI: 10.1103/PhysRevD.88.033001.

[23] D. Casper et al. "Measurement of atmospheric neutrino composition with the IMB-3 detector". In: *Phys. Rev. Lett.* 66 (20 May 1991), pp. 2561–2564. DOI: 10.1103/PhysRevLett.66.2561.

[24] M Ambrosio et al. "Measurement of the atmospheric neutrino-induced upgoing muon flux using MACRO". In: *Physics Letters B* 434.3 (1998), pp. 451–457. ISSN: 0370-2693. DOI: https://doi.org/10.1016/S0370-2693(98)00885-5.

[25] W.W.M. Allison et al. "Measurement of the atmospheric neutrino flavour composition in Soudan 2". In: *Physics Letters B* 391.3 (1997), pp. 491–500. ISSN: 0370-2693. DOI: https://doi.org/10.1016/S0370-2693(96)01609-7.

[26] Oleg Kalekin and (on behalf ofthe ANTARES collaboration). "The ANTARES underwater neutrino telescope". In: *Journal of Physics: Conference Series* 160.1 (Apr. 2009), p. 012036. DOI: 10.1088/1742-6596/160/1/012036.

[27] R. Abbasi et al. "The Design and Performance of IceCube DeepCore". In: *Astropart. Phys.* 35 (2012), pp. 615–624. DOI: 10.1016/j.astropartphys.2012.01.004. arXiv: 1109.6096 [astro-ph.IM].

[28] M.G. Aartsen et al. "Neutrino oscillation studies with IceCube-DeepCore". In: *Nuclear Physics B* 908 (2016). Neutrino Oscillations: Celebrating the Nobel Prize in Physics 2015, pp. 161–177. ISSN: 0550-3213. DOI: https://doi.org/10.1016/j.nuclphysb.2016.03.028.

[29] M. H. Ahn et al. "Measurement of neutrino oscillation by the K2K experiment". In: *Phys. Rev. D* 74 (7 Oct. 2006), p. 072003. DOI: 10.1103/PhysRevD.74.072003.

[30] D. G. Michael et al. "Observation of muon neutrino disappearance with the MINOS detectors and the NuMI neutrino beam". In: *Phys. Rev. Lett.* 97 (2006), p. 191801. DOI: 10.1103/PhysRevLett.97.191801. arXiv: hep-ex/0607088.

[31] M. A. Acero and others. "Improved measurement of neutrino oscillation parameters by the NOvA experiment". In: *Physical Review D* 106.3 (2022). ISSN: 2470-0029. DOI: 10.1103/physrevd.106.032004. URL: http://dx.doi.org/10.1103/PhysRevD.106.032004.

[32] K. Abe et al. "Constraint on the matter–antimatter symmetry-violating phase in neutrino oscillations". In: *Nature* 580.7803 (2020), pp. 339–344. ISSN: 1476-4687. DOI: 10.1038/s41586-020-2177-0. URL: http://dx.doi.org/10.1038/s41586-020-2177-0.

[33] F. P. An et al. "Precision Measurement of Reactor Antineutrino Oscillation at Kilometer-Scale Baselines by Daya Bay". In: *Phys. Rev. Lett.* 130 (16 Apr. 2023), p. 161802. DOI: 10.1103/PhysRevLett.130.161802. URL: https://link.aps.org/doi/10.1103/PhysRevLett.130.161802.

[34] A. Meregaglia. "Multi detector results from the Double Chooz experiment". In: *52nd Rencontres de Moriond on EW Interactions and Unified Theories*. 2017, pp. 359–366.

[35] G. Bak et al. "Measurement of Reactor Antineutrino Oscillation Amplitude and Frequency at RENO". In: *Phys. Rev. Lett.* 121 (20 Nov. 2018), p. 201801. DOI: 10.1103/PhysRevLett.121.201801. URL: https://link.aps.org/doi/10.1103/PhysRevLett.121.201801.

[36] Ivan Esteban et al. "The fate of hints: updated global analysis of three-flavor neutrino oscillations". In: *JHEP* 09 (2020), p. 178. DOI: 10.1007/JHEP09(2020)178. arXiv: 2007.14792 [hep-ph].

[37] P. F. De Salas et al. "Neutrino Mass Ordering from Oscillations and Beyond: 2018 Status and Future Prospects". In: *Front. Astron. Space Sci.* 5 (2018), p. 36. DOI: 10.3389/fspas.2018.00036. arXiv: 1806.11051 [hep-ph].

[38] NuFIT Collaboration. *NuFIT 5.0: Three-flavour neutrino oscillation analysis*. http://www.nu-fit.org/. Accessed: 2024-09-25. 2024.

[39] M. Ball et al. *The PIP-II Conceptual Design Report*. Tech. rep. Mar. 2017. DOI: 10.2172/1346823.

[40] James Strait et al. *Long-Baseline Neutrino Facility (LBNF) and Deep Underground Neutrino Experiment (DUNE): Conceptual Design Report, Volume 3: Long-Baseline Neutrino Facility for DUNE June 24, 2015*. arXiv: 1601.05823 [physics.ins-det]. Jan. 2016. arXiv: 1601.05823 [physics.ins-det].

[41] C. Brizzolari et al. "Enhancement of the X-Arapuca photon detection device for the DUNE experiment". In: *JINST* 16.09 (2021), P09027. DOI: 10.1088/1748-0221/16/09/P09027. arXiv: 2104.07548 [physics.ins-det].

[42] DUNE Collaboration, B. Abi et al. "Deep Underground Neutrino Experiment (DUNE), Far Detector Technical Design Report, Volume II DUNE Physics". In: *arXiv* (2020). arXiv: 2002.03005 [hep-ex].

[43] B. Abi et al. "Long-baseline neutrino oscillation physics potential of the DUNE experiment". In: *Eur. Phys. J. C* 80.10 (2020), p. 978. DOI: 10.1140/epjc/s10052-020-08456-z. arXiv: 2006.16043 [hep-ex].

[44] DUNE Measurement of CP Violation. "Baseline Optimization for the Measurement of CP Violation, Mass Hierarchy, and θ_{23} Octant in a Long-Baseline Neutrino Oscillation Experiment". In: *Phys. Rev. D* 91.5 (2015), p. 052015. DOI: 10.1103/PhysRevD.91.052015. arXiv: 1311.0212 [hep-ex].

[45] A. Abed Abud et al. *Snowmass Neutrino Frontier: DUNE Physics Summary*. Mar. 2022. arXiv: 2203.06100 [hep-ex].

[46] L. Hüdepohl et al. "Neutrino Signal of Electron-Capture Supernovae from Core Collapse to Cooling". In: *Phys. Rev. Lett.* 104.25 (June 2010), p. 251101. DOI: 10.1103/PhysRevLett.104.251101.

[47] Francesco Capozzi et al. "DUNE as the Next-Generation Solar Neutrino Experiment". In: *Phys. Rev. Lett.* 123.13 (2019), p. 131803. DOI: 10.1103/PhysRevLett.123.131803. arXiv: 1808.08232 [hep-ph].

[48] Lorenz Hudepohl. "Neutrinos from the Formation, Cooling and Black Hole Collapse of Neutron Stars". PhD thesis. Technical University of Munich, Oct. 2013.

[49] Y. Farzan and M. Tortola. "Neutrino Oscillations and Non-Standard Interactions". In: *Front. in Phys.* 6 (2018), p. 10. DOI: 10.3389/fphy.2018.00010. arXiv: 1710.09360 [hep-ph].

[50] Lina Necib et al. "Boosted Dark Matter at Neutrino Experiments". In: *Phys. Rev. D* 95.7 (2017), p. 075018. DOI: 10.1103/PhysRevD.95.075018. arXiv: 1610.03486 [hep-ph].

[51] Valentina De Romeri, Kevin J. Kelly, and Pedro A. N. Machado. "Hunting for Light Dark Matter with DUNE PRISM". In: *Journal of Physics: Conference Series*. Vol. 1468. 1. Feb. 2020, p. 012061. DOI: 10.1088/1742-6596/1468/1/012061.

[52] B. Abi et al. "Prospects for beyond the Standard Model physics searches at the Deep Underground Neutrino Experiment". In: *Eur. Phys. J. C* 81.322 (2021). DOI: 10.1140/epjc/s10052-021-09007-w.

[53] M. Adinolfi et al. "The KLOE electromagnetic calorimeter". In: *Nuclear Instruments and Methods in Physics Research Section A: Accelerators, Spectrometers, Detectors and Associated Equipment* 482.1 (2002), pp. 364–386. ISSN: 0168-9002. DOI: 10.1016/S0168-9002(01)01502-9. URL: https://doi.org/10.1016/S0168-9002(01)01502-9.

[54] Deep Underground Neutrino Experiment (DUNE). *Near Detector Conceptual Design Report*. arXiv:2103.13910v1 [physics.ins-det]. Mar. 2021. arXiv: 2103.13910v1 [physics.ins-det]. URL: https://arxiv.org/abs/2103.13910v1.

[55] Hamamatsu Photonics. *MPPC S14160-3050HS*. https://www.hamamatsu.com/jp/en/product/optical-sensors/mppc/mppc-mppc-array/S14160-3050HS.html. Last accessed on 2023-01-26.

[56] M. Hofmann et al. "Ion-beam excitation of liquid argon". In: *The European Physical Journal C* 73 (2013), p. 2618. DOI: 10.1140/epjc/s10052-013-2618-0.

[57] Joshua Jortner et al. "Localized Excitations in Condensed Ne, Ar, Kr, and Xe". In: *The Journal of Chemical Physics* 42.12 (1965), pp. 4250–4253. DOI: 10.1063/1.1695927. URL: https://doi.org/10.1063/1.1695927.

[58] Ettore Segreto. "Properties of Liquid Argon Scintillation Light Emission". In: *Physical Review D* 103.4 (2021), p. 043001. DOI: 10.1103/PhysRevD.103.043001. arXiv: 2012.06527 [physics.ins-det].

[59] *DUNE Geometry Description*. https://github.com/DUNE/dunendggd. Accessed: April 2024.

[60] C. Andreopoulos et al. "The GENIE Neutrino Monte Carlo Generator". In: *Nucl. Instrum. Meth.* A614 (2010), pp. 87–104. DOI: 10.1016/j.nima.2009.12.009. arXiv: 0905.2517 [hep-ph].

[61] Rene Brun and Fons Rademakers. "ROOT — An object oriented data analysis framework". In: *Nuclear Instruments and Methods in Physics Research Section A: Accelerators, Spectrometers, Detectors and Associated Equipment* 389.1 (1997), pp. 81–86. ISSN: 0168-9002. DOI: 10.1016/S0168-9002(97)00048-X. URL: https://www.sciencedirect.com/science/article/pii/S016890029700048X.

[62] Clark D. McGrew. *edep-sim*. https://github.com/ClarkMcGrew/edep-sim. Last accessed on 2023-01-27.

[63] T. Heindl et al. "The scintillation of liquid argon". In: *Europhysics Letters* 91.6 (Oct. 2010), p. 62002. DOI: 10.1209/0295-5075/91/62002.

[64] Valerio Pia. "Study of the calorimetric performance of a liquid Argon detector based on a novel optical imaging concept". PhD thesis. amsdottorato, Alma Mater Studiorum - Università di Bologna, Bologna U., 2023. DOI: 10.48676/unibo/amsdottorato/10933..

[65] V. Cicero. "Study of the tracking performance of a liquid Argon detector based on a novel optical imaging concept". PhD thesis. Ph. D. Thesis, 2023.

[66] Zbisław Tabor. "An analytical solution to the problem of linear track segment reconstruction in drift tube chambers". In: *Nuclear Instruments and Methods in Physics Research Section A: Accelerators, Spectrometers, Detectors and Associated Equipment* 788 (2015), pp. 106–110. ISSN: 0168-9002. DOI: https://doi.org/10.1016/j.nima.2015.03.086. URL: https://www.sciencedirect.com/science/article/pii/S0168900215004507.

[67] Liu Qiu-Guang et al. "Track reconstruction using the TSF method for the BESIII main drift chamber". In: *Chinese Physics C* 32 (Oct. 2010), p. 565. DOI: 10.1088/1674-1137/32/7/011.

[68] M Adinolfi et al. "The tracking detector of the KLOE experiment". In: *Nuclear Instruments and Methods in Physics Research Section A: Accelerators, Spectrometers, Detectors and Associated Equipment* 488.1 (2002), pp. 51–73. ISSN: 0168-9002. DOI: https://doi.org/10.1016/S0168-9002(02)00514-4. URL: https://www.sciencedirect.com/science/article/pii/S0168900202005144.

[69] Irene Cagnoli. "Electromagnetic Shower Identification in the SAND Calorimeter of the DUNE Near Detector". PhD thesis. PhD Thesis, 2021.

[70] S. J. Barish et al. "Measurement of the Total Cross Section for Deep-Inelastic Electron-Proton Scattering". In: *Physical Review D* 19 (1979), p. 2521.

[71] V. A. Okorokov et al. "A search for lepton charge nonconservation in K decays". In: *Zeitschrift für Physik C Particles and Fields* 10.1 (1981), pp. 63–70. DOI: 10.1007/BF01881707.

[72] M. S. Alam et al. "The upgrade of the ALICE central barrel TPC for operation at the CERN LHC". In: *The European Physical Journal A* 43.4 (2010), pp. 369–374. DOI: 10.1007/BF02440830.

[73] M. Derrick et al. "Multiplicity distributions in $\overline{\nu}_\mu p$ interactions". In: *Phys. Rev. D* 25 (3 Feb. 1982), pp. 624–633. DOI: 10.1103/PhysRevD.25.624. URL: https://link.aps.org/doi/10.1103/PhysRevD.25.624.

[74] Benedikt R. Webber. *RooUnfold: an unfolding library based on RooFit*. CERN-TH-2011-235. 2012. URL: https://gitlab.cern.ch/RooUnfold/RooUnfold.

[75] C.H. Llewellyn Smith. "Neutrino Interactions". In: *Physics Reports* 3C (1972), p. 261. DOI: 10.1016/0370-1573(72)90040-4.